FEDERAL UNIVERSITY OF SAO CARLOS
CENTER FOR EXACT SCIENCES AND TECHNOLOGY
GRADUATE PROGRAM IN CIVIL ENGINEERING

MATHEUS PENA DA SILVA E SILVA

SHEAR BOND AND SHEAR FATIGUE OF GEOSYNTHETIC INTERLAYERED ASPHALT OVERLAYS

SAO CARLOS – SP
2024

MATHEUS PENA DA SILVA E SILVA

SHEAR BOND AND SHEAR FATIGUE OF GEOSYNTHETIC INTERLAYERED ASPHALT OVERLAYS

Doctoral dissertation presented to Graduate Program in Civil Engineering of Federal University of Sao Carlos in partial fulfillment of the requirements for the Degree of Doctor of Science

Concentration area: Structures and Geotechnics

Supervisor: Dr. Natalia de Souza Correia

SAO CARLOS – SP

2024

UNIVERSIDADE FEDERAL DE SÃO CARLOS

Centro de Ciências Exatas e de Tecnologia
Programa de Pós-Graduação em Engenharia Civil

Folha de Aprovação

Defesa de Tese de Doutorado do candidato Matheus Pena da Silva e Silva, realizada em 01/03/2024.

Comissão Julgadora:

Profa. Dra. Natália de Souza Correia (UFSCar)

Prof. Dr. Jorge Gabriel Zornberg (UT)

Prof. Dr. Ennio Marques Palmeira (UnB)

Prof. Dr. Jaime Rafael Obando Ante (UNICAUCA)

Prof. Dr. Luiz Guilherme Rodrigues de Mello (UnB)

O Relatório de Defesa assinado pelos membros da Comissão Julgadora encontra-se arquivado junto ao Programa de Pós-Graduação em Engenharia Civil.

DEDICATION

To the Lord, for guiding and supporting me this far,

To my parents and brother, for their endless love, support, and encouragement,

To my wife, Nathasha, for her sacrifice and unwavering support over the last four years.

ACKNOWLEDGEMENTS

First of all, I would like to express my sincere gratitude to my parents and brother. Without your endless support, love, sacrifice, and encouragement, none of this would have been possible. I thank my mother for her example of perseverance and my father for his example of humility.

I will always be grateful to my wife, Nathasha, who sacrificed herself to be by my side away from her parents, supporting, loving, and believing in me.

I would like to thank gratefully and sincerely my supervisor, Professor Dr. Natalia Correia, for her guidance, support, understanding, and encouragement over the last four years, as well as for the opportunity to be part of the GEGEOS/UFSCar family. Under her supervision, I was able to participate in international projects, improve my scientific knowledge, learn about innovation, and develop laboratory infrastructure. I also evolved into being an independent researcher and advisor for master and undergraduate students. Professor Natalia, I owe you my eternal gratitude.

I would also like to thank Prof. Dr. Jorge G. Zornberg for accepting me as one of your students, supervising me, and providing guidance during my period as a visiting scholar at The University of Texas at Austin. I truly appreciate the suggestions, collaborations, and discussions with this research.

I extend my gratitude to Prof. Dr. Fernando Portelinha not only for his suggestions, collaborations, and discussions with this research, but also for his financial support.

I express my gratitude to the friends and colleagues I encountered during my time in Sao Carlos. Special thanks to Matheus Cardoso, a friend, fellow PhD candidate, and technician at the Laboratory of Geotechnics, and Dhionata Santos, Paulo Figueiredo, Mauro Sousa, Karolina Santos, Débora Toledo, Gabriele Martins, Andrea Vieira, Laura Cassini, Ana Laura Gianello, Ramon Felipe, Tiago Souza, and Sérgio Santilli. Each of you has contributed in various ways, and I appreciate your assistance.

I express gratitude to UT student research group for the suggestions on data analysis. Special thanks to Ph.D. candidate Ashray Saxena and Dr. Vinay Kumar. During my brief period at UT, our discussions helped me improve my scientific knowledge.

Thanks to my master's degree supervisor, Professor Dr. Consuelo Frota. Throughout the years, she supervised me during my master's research and taught me most of my current knowledge on asphalt mixture. This foundation helped me solve several issues during my PhD research project.

I acknowledge the support received from FAPESP (Foundation for Research Support of the State of Sao Paulo) through project number 2020/16027-9.

I acknowledge FAPEAM (Foundation for Research Support of the State of Amazonas) through process number 01.02.016301.001624/2021-10 for the PhD scholarship.

This study was financed in part by the Coordenação de Aperfeiçoamento de Pessoal de Nível Superior – Brasil (CAPES) – Finance Code 001. I acknowledge the scholarship received from CAPES PRInt – UFSCar program.

I am grateful to TDM Brazil, S&P Clever Brazil, Huesker, Asphalt Stratura, Bandeirantes Asphalt plant for offering all the necessary materials that made this research possible.

I thank the Graduate Program in Civil Engineering and the Federal University of Sao Carlos for all the institutional and material support that allowed the development of this work.

Last but not least, I would like to thank everyone who directly or indirectly contributed to the conclusion of my PhD project.

ABSTRACT

Innovative applications of paving geosynthetics have emerged to reduce reflective crack propagation and moisture infiltration in pavement structures, leading to the development of various products such as paving grids, composites, and mats. The diversity within the geosynthetic market encompasses products with differing properties. Ensuring an adequate bond between paving geosynthetics and adjacent asphalt layers is crucial for proper asphalt system performance. However, the impact of paving geosynthetic properties, along with tack coat types and rates, on bond properties remains uncertain. This study aims to assess the influence of multiple factors on interface shear bond and shear fatigue parameters. A comprehensive testing program utilizing a multifunctional interface shear tester and laboratory-prepared double-layered asphalt specimens with paving geosynthetics was conducted. The experimental setup involved nine types of paving geosynthetics, two tack coat types, and varying tack coat rates. Results from interface shear bond tests demonstrate significant effects from the paving geosynthetic type, tack coat type and rate, as well as their interactions. Multiple linear regression analysis identified geogrid mesh area, paving geosynthetic thickness, fabric backing thickness, and presence of bitumen coating as key factors influencing interface shear strength. A predictive model for geosynthetic-reinforced asphalt layers' interface shear strength based on geosynthetic properties is proposed. Additionally, shear fatigue test results revealed that bitumen content of the geosynthetic coating, type of fabric in the geosynthetics, and geogrid mesh area predominantly affect shear fatigue life. Furthermore, a correlation between shear fatigue life and interface bond parameters was observed. Overall, these findings enhance understanding of geosynthetic properties affecting short and long-term bonding properties, as well as the impact of tack coat type and rate, and, in the case of shear fatigue tests, test frequency.

Keywords: paving geosynthetic, asphalt overlays, interface bond, shear Fatigue.

RESUMO

Aplicações inovadoras de geossintéticos na pavimentação surgiram para reduzir a propagação de trincas reflexivas e a infiltração de água em estruturas de pavimento, levando ao desenvolvimento de diversos produtos, como geogrelhas e geocompostos. A diversidade dentro do mercado de geossintéticos engloba produtos com propriedades diferentes. Garantir uma aderência adequada entre os geossintéticos e as camadas de asfalto é crucial para o desempenho adequado desta técnica. No entanto, o impacto das propriedades dos geossintéticos, juntamente com os tipos e taxas de pintura de ligação, nas propriedades de aderência permanece incerto. Este estudo tem como objetivo avaliar a influência de múltiplos fatores nos parâmetros de cisalhamento de interface e de fadiga por cisalhamento. Um programa ensaios foi conduzido, utilizando um dispositivo de cisalhamento de interface multifunctional, bem como corpos de prova de asfalto de dupla camada preparados em laboratório com geossintéticos. O programa experimental envolveu nove tipos de geossintéticos, dois tipos de pintura de ligação e taxas de aplicações diferentes. Os resultados dos ensaios de cisalhamento de interface demonstraram efeitos significativos do tipo de geossintético, tipo e taxa de pintura de ligação, bem como suas interações. A análise de regressão linear múltipla identificou a área da malha do geogrelha, a espessura do geossintético, a espessura do geotêxtil de suporte e a presença de cobertura de betuminosa como fatores-chave que influenciam a resistência ao cisalhamento da interface. Modelos de previsão da resistência ao cisalhamento de interface de camadas de asfalto reforçadas com geossintéticos com base nas propriedades dos geossintéticos foram propostos. Além disso, os resultados dos testes de fadiga de cisalhamento revelaram que o teor de betume na cobertura betuminosa de geossintéticos, o tipo de geotêxtil presente nos geossintéticos e a área da malha do geogrelha afetam predominantemente a vida útil de fadiga de cisalhamento. Além disso, observou-se uma correlação entre a vida útil de fadiga por cisalhamento e os parâmetros de cisalhamento de interface obtidos no ensaio de cisalhamento de interface. No geral, essas descobertas melhoram a compreensão das propriedades dos geossintéticos que afetam as propriedades de aderência a curto e longo prazo, bem como o impacto do tipo e taxa de pintura de ligação e, no caso de ensaios de fadiga por cisalhamento, a frequência de ensaio.

Palavras-chave: geossintéticos na pavimentação, dupla camada de asfalto, cisalhamento de interface, fadiga por cisalhamento.

LIST OF FIGURES

Figure 2.1 – Case study at Salvador International Airport: (a) installation process, (b) extracted field core specimen showing debonding, (c) asphalt layer slippage failure at geosynthetic interface, and (d) hole from specimen extraction closed after slippage. Source: Correia et al. (2023). 26
Figure 2.2 – Schematic of relative displacement between two bonded layers. Source: Roque et al. (2017). 28
Figure 2.3 – Distribution of strain vs. depth for different interface shear stiffness. Source: Canestrari et al. (2013). 29
Figure 2.4 – Different modes of failure at asphalt interface: (a) pure shear, (b) pure tension, (c) shear-compression, (d) shear-tension. 30
Figure 2.5 – The field mechanism of bond failures. Source: Sudarsanan et al. (2016)..... 30
Figure 2.6 – Different test methods for interface bonding evaluation. Source: Rahman et al. (2017). 31
Figure 2.7 – Pure shear testing devices: (a) Leutner, (b) LPDS. Fonte: Canestrari et al. (2013).. 32
Figure 2.8 – Shear stress-displacement curve. 34
Figure 2.9 – Interface shear testing devices with application of normal stress: (a) ASTRA, (b) LISST. Source: a) Canestrari et al. (2013); b) Mohammad et al. (2009). 35
Figure 2.10 – LISST test performed during NCHRP 09-40A project. Source: Mohammad et al. (2018). 37
Figure 2.11 – Field test required in Australia for bond evaluation. Source: Department of Transport and Main Roads (2021). 38
Figure 2.12 – Comparison between *ISS* results obtained using Leutner and ASTRA devices. Source: Ragni et al. (2019). 40
Figure 2.13 – Correlation between shear displacement rate and *ISS*. Source: Canestrari et al. (2013). 40
Figure 2.14 – Interface shear strength behavior with the variation of displacement rate and temperature: (a) asphalt overlays without paving geosynthetic, (b) asphalt overlays with paving geosynthetic (CF), (c) asphalt overlays with paving geosynthetic (FP). Source: Canestrari et al. (2018). 42

Figure 2.15 – Comparison between *ISS* obtained from field specimens and laboratory-prepared specimens Source: Canestrari et al. (2005). 44
Figure 2.16 – Influence of specimen extraction on the *ISS* obtained from specimens without paving geosynthetic. Source: Sufian et. al. (2021). 45
Figure 2.17 – Shear strength with respect to aging, based on US-90 project data. Source: Sholar et al. (2004). 46
Figure 2.18 – Effect of different types of emulsions on *ISS*. Source: Sufian et al. (2021). 47
Figure 2.19 – Influence of different tack coat types on *ISS*. Source: Yang et al. (2021). 48
Figure 2.20 – Influence of tack coat type on *ISS* obtained from asphalt overlays with paving geosynthetic. Source: Safavizadeh et al. (2020). 49
Figure 2.21 – Effect of the tack coat type and rate, and temperature on *ISS*: (a) 25°C, (b) 50°C. Source: Hu et al. (2017a). 50
Figure 2.22 – Effect of the temperature and tack coat rate on *ISS.* Source: Yang et al. (2021). ... 50
Figure 2.23 – Effect of the tack coat rate on *ISS* of asphalt overlays with different paving geosynthetic. Source: Correia et al. (2023). 51
Figure 2.24 – Bonding mechanism (upper asphalt surface/lower asphalt surface): (a) geogrid (THB/THB), (b) geotextile (adhesion/adhesion), and (c) geocomposite (THB/adhesion). Source: Sudarsanan et al. (2018). 53
Figure 2.25 – Testing device used in Donavan et al. (2000): (a) device schematic, (b) device photograph. 55
Figure 2.26 – Shear fatigue device schematic. Source: Romanoschi and Metcalf (2001) 56
Figure 2.27 – Sapienza Inclined Shear Test Machine. Source: D'Andrea and Tozzo (2016)..... 56
Figure 2.28 – Scheme of Sapienza Direct Shear Testing Machine. Source: Tozzo et al. (2014b) 57
Figure 2.29 – Double shear test: a) schematic diagram of the double shear test, b) schematic and photographic presentation of the double shear device. Source: Diakhaté et al. (2011). 57
Figure 2.30 – Testing devices used by the participating laboratories of Task Group 3 of RILEM TC 272-PIM: (a) C-ASTRA, (b) AST, (c) MAST, (d) CCSB, and (e) RIL. Source: Canestrari et al. (2022). 58
Figure 2.31 – Types of pulses: a) Haversine and sinusoidal waveform without a rest period (Cheng et al., 2021); b) Haversine pulse with a rest period (Tozzo et al., 2016)..... 60

Figure 2.32 – Typical results from dynamic tests: a) permanent displacement vs. number of cycles obtained from shear fatigue test (Tozzo et al., 2014b); b) permanent displacement curve vs. number of cycles obtained from dynamic creep test (Alavi et al., 2011) 61
Figure 2.33 – Phase angle for different types of waveform pulse: (a) sinusoidal waveform, (b) haversine waveform. Source: Venudharan and Biligiri (2015). 62
Figure 2.34 – Approaches for N_{50}: (a) interface shear stiffness modulus vs. number of cycles (Isailović and Wistuba, 2018), (b) normalized interface shear stiffness modulus vs. number of cycles (Diakhaté et al., 2011). 63
Figure 2.35 – Normalized stiffness times normalized cycles failure criterion's approach. Source: ASTM D8237 (2021). 64
Figure 2.36 – Relationship between shear fatigue life and loading frequency. Source: Nian et al. (2020). 66
Figure 2.37 – Fatigue life's trend of different tack coat types under different temperatures. Source: Wang et al. (2017). 66
Figure 2.38 – Shear fatigue behavior under different stress pulse amplitude: (a) fixed stress values, (b) fixed Δτ/ISS ratio. Source: (a) Miró et al. (2021), (b) Nian et al. (2020). 67
Figure 2.39 – Shear fatigue life at different normal stress. Source: Tozzo et al. (2014b). 67
Figure 2.40 – The variation of shear fatigue life with different tack coat type. Source: Yang et al. (2020) 68
Figure 2.41 – Number of cycles to failure versus tack coat rate. Source: Donovan et al. (2000). 68
Figure 2.42 – Bond type ranking in monotonic shear test (based on resulting shear strengths) and in cyclic shear test (based on shear fatigue life). Source: Isailović and Wistuba (2018). 69
Figure 2.43 – Correlation between fatigue life and interface shear stiffness modulus. Source: Yang et al. (2020). 70
Figure 3.1 – Asphalt mixture materials: (a) crushed stone size number 67, (b) crushed stone size number 8, (c) stone dust size number 89, (d) stone dust classified as size number 10, (e) calcitic hydrated lime, (f) PG 82-16. 71
Figure 3.2 – Particle size distribution curves for each material composing the asphalt mixture. . 72
Figure 3.3 – HMA gradation. 72
Figure 3.4 – Paving composites and paving mat: (a) Pa-C-1, (b) Pa-C-2, (c) Pa-C-3, (d) Pa-C-4, and (e) P-M. 76

Figure 3.5 – Paving grids: (a) Pa-G-1, (b) Pa-G-2, (c) Pa-G-3, (d) Pa-G-4. 77
Figure 3.6 – Physical characterization of geosynthetics: (a) identification of measurements, (b) measurement of the longitudinal yarn, (c) nominal thickness under 2 kPa. 78
Figure 3.7 – Index asphalt retention procedure using PG 58-16. 79
Figure 3.8 – Index asphalt retention procedure using CRS-1, adapted from ASTM D6140. 80
Figure 3.9 – Bitumen content of the coating testing: (a) specimens, (b) geosynthetic immersed in perchloroethylene solvent, (c) test after 24 hours. 81
Figure 4.1 – Marshall apparatus: (a) design of the compaction mold assembly, (b) compaction mold assembly, (c) compaction pedestal. 84
Figure 4.2 – Mixing and compaction temperature ranges. 85
Figure 4.3 – Production of double-layered asphalt specimens with paving geosynthetics: (a) pre-heated binder and aggregates, (b) mixing, (c) compacted bottom asphalt layer, (d) application of CRS-1, (e) application of PG 58-16, (f) spreading PG 58-16, (g) Placement of the geosynthetic, (h) prepared specimen. 86
Figure 5.1 – Multifunctional interface shear testing (MIST) device. 87
Figure 5.2 – Different test configurations: (a) LISST configuration with normal stress, (b) ASTRA configuration with normal stress, (c) LISST configuration without normal stress, (d) Leutner shear test configuration; (e) side view of the gap interface, (f) front view after conducting Leutner shear test. 89
Figure 6.1 – Electropneumatic dynamic testing machine. 94
Figure 6.2 – Test configuration tab. 95
Figure 6.3 – Permanent displacement tab. 96
Figure 6.4 – Interface shear stiffness modulus tab. 96
Figure 6.5 – Comparison between theoretical and measured pulse waveform: (a) haversine waveform, (b) 1 Hz, (c) 5 Hz, (d) 10 Hz. 97
Figure 6.6 – Alignment and seating of the test specimen: (a) interface marking, (b) test specimen horizontally positioned, (c) traffic direction alignment. 100
Figure 6.7 – Typical curve of permanent shear displacement versus the number of cycles. 103
Figure 6.8 – Curves of permanent shear displacement, fitted permanent shear displacement, and permanent shear displacement rate versus number of cycles together. 104

Figure 6.9 – Typical results related to cyclic interface shear stiffness modulus: (a) cyclic interface shear stiffness modulus versus number of cycles, (b) the normalized cyclic interface shear stiffness modulus x normalized cycles versus number of cycles. 105
Figure 6.10 – (a) raw and fitted cyclic interface shear modulus curve, (b) raw and fitted normalized cyclic interface shear stiffness modulus x normalized cycles versus number of cycles. 106
Figure 6.11 – Different approaches to determine the failure point: (a) shear flow number approach, (b) normalized cyclic interface shear stiffness modulus x normalized cycles approach, (c) design cyclic interface shear stiffness modulus. 107
Figure 7.1 - Typical interface shear stress-displacement for different interface conditions: (a) control, (b) Pa-G-1, (c) Pa-G-2, (d) Pa-G-3, (e) Pa-G-4, (f) Pa-C-1, (g) Pa-C-2, (h) Pa-C-3, (i) Pa-C-4, and (j) P-M. 110
Figure 7.2 – Average *ISS* values for different variables in asphalt layers with paving geosynthetic. 111
Figure 7.3 – Geogrid mesh area causing interlocking of HMA aggregates. 121
Figure 7.4 – Effect of the geogrid thickness. 122
Figure 7.5. Effect of the presence and absence of bitumen coating: (a) geogrid coated with bitumen attached to upper asphalt layer, (b) comparison of tack coat impregnation of paving geogrid with different tack coat rates. 122
Figure 7.6 – Effect of fabric backing thickness: (a) detached fabric backing saturated with tack coat facilitating adhesion mechanism, (b) Thick fabric backing with lower tack coat saturation impairing THB mechanism. 123
Figure 7.7 – Comparison between measured and predicted ISS values for: (a) CRS-1 at 400 g/m²; (b) CRS-1 at 600 g/m²; and (c) CRS-1 at 800 g/m². 125
Figure 7.8 – Minimum predicted *ISS* to meet minimum *ISS* required for laboratory-prepared specimens: (a) CRS-1; and (b) PG58-16. 126
Figure 7.9 – Prediction of interface shear stiffness modulus based on interface shear strength for each interface condition: (a) CRS-1 and PG 58-16 at a rate of 400 g/m², (b) CRS-1 and PG 58-16 at a rate of 600 g/m², (c) CRS-1 and PG 58-16 at a rate of 800 g/m². 127
Figure 8.1 – Typical curves of permanent shear displacement versus the number of cycles for different combinations of paving geosynthetic and tack coat types. 129

Figure 8.2 Shear fatigue parameters for different types of geosynthetic and tack coat: (a) N_f, (b) $k_{s,d}$. 130
Figure 8.3 – Typical curves of permanent shear displacement versus the number of cycles for different combinations of paving geosynthetic and tack coat rate. 132
Figure 8.4 –Shear fatigue parameters for different types of paving geosynthetics and tack coat rates: (a) N_f, (b) $k_{s,d}$. 133
Figure 8.5 – Typical curves of permanent shear displacement versus the number of cycles for different combinations of paving geosynthetic and test frequency. 135
Figure 8.6 – Shear fatigue parameters for different types of paving geosynthetic and test frequency: (a) N_f, (b) $k_{s,d}$. 135
Figure 8.7 – Typical curves of permanent shear displacement versus the number of cycles for combinations with different paving geosynthetics combined with PG 58-16 at a tack coat rate of 600 g/m². 137
Figure 8.8 – Average shear fatigue life for the combinations with different geosynthetics..... 138
Figure 8.9 – Average cyclic interface shear stiffness modulus for the control test specimen and for test specimen with different paving geosynthetics. 139
Figure 8.10 – Correlation between $k_{s,d.}$ and N_f. 140
Figure 8.11 – Effect of geogrid mesh area causing aggregate interlocking. 142
Figure 8.12 – Illustration of the geosynthetic properties affecting shear fatigue life: (a) bitumen-coated geogrid of Pa-C-1 attached to surrounding asphalt layer facilitating adhesion, (b) fabric strips reducing the effect of THB mechanism, (c) Thin fabric backing reducing the effect of THB mechanism, and (d) thick fabric backing with lower tack coat saturation impairing THB mechanism. 143
Figure 8.13 – Scatterplot comparing predicted and average measured N_f values in this study... 144
Figure 8.14 – Linear regression and correlation between shear fatigue life and interface shear strength: (a) considering all paving geosynthetics, (b) after excluding Pa-C-1 and Pa-G-4. 144
Figure 8.15 – Linear regression and correlation between shear fatigue life and interface shear strength: (a) considering all paving geosynthetics, (b) after excluding Pa-C-1 and Pa-G-4. 146

LIST OF TABLES

Table 3.1 – Properties of aggregates. 73
Table 3.2 – Absorption, bulk and apparent specific gravity. 73
Table 3.3 – Properties of PG 82-16. 74
Table 3.4 – Final proportion of the materials composing the HMA. 74
Table 3.5 – Properties of HMA. 74
Table 3.6 – Properties of PG 58-16. 75
Table 3.7 – Properties of CRS-1. 75
Table 3.8 – Properties of the paving geosynthetics. 82
Table 5.1 – Equality of means of *ISS* and *k* between the results derived from the MIST device in Leutner configuration and those obtained from a commercially available version of Leutner shear test device. 90
Table 5.2 – Values of ϕ for 95% confidence level. 92
Table 5.3 – Experimental program for interface shear bond tests. 93
Table 6.1 – Coefficient of variation for each parameter for the different test configurations. 98
Table 6.2 – Experimental test program of the shear fatigue testing. 108
Table 7.1 – ANOVA for paving geosynthetic type, tack coat type, tack coat rate and interactions. 113
Table 7.2 – Effect size of factors and interactions. 114
Table 7.3 – Assumptions of MLR model. 115
Table 7.4 – Description of predictor variables for *ISS*. 117
Table 7.5 – Statistics of the MLR models established for interface shear strength and the assumption checks. 118
Table 7.6 – Significance test results for each regression coefficient selected to predict *ISS*. 120
Table 7.7 – Regression coefficients and minimum interface shear stiffness modulus values. 128
Table 8.1 – Two-way ANOVA for shear fatigue parameters results considering the paving geosynthetic type and tack coat type. 131
Table 8.2 – Two-way ANOVA for shear fatigue parameters results considering the paving geosynthetic type and tack coat rate. 134

Table 8.3 – Two-way ANOVA for shear fatigue parameters results considering the paving geosynthetic type and test frequency. 136
Table 8.4 – One-way ANOVA of shear fatigue parameters for different paving geosynthetics. 139
Table 8.5 – Description of predictor variables for N_f. 141
Table 8.6 – Statistics of the predictive model established for shear fatigue life and the assumption checks. 141
Table 8.7 – Significance test results for each regression coefficient selected to predict shear fatigue life. 142

LIST OF ABBREVIATIONS

ANOVA - Analysis of variance

AST - Advanced Shear Tester

ASTRA - Ancona Shear Testing Research and Analysis

C-ASTRA - Cyclic-Ancona Shear Testing Research and Analysis

CRS - Cationic rapid-setting emulsion

HMA - Hot Mix Asphalt

ISE - Interface shear energy

ISFE - Interface shear fracture energy

ISS - Interface shear strength

LISST - Louisiana Interface Shear Strength Tester

LPDS - Layer-Parallel Direct Shear

LVDT -Linear Variable Differential Transformer

MAST - Modified Advanced Shear Tester

MIST - Multifunctional Interface Shear Tester

MLR - Multiple Linear Regression

PET - Polyester

PG - Performance grade

PP - Polypropylene

PVA - Polyvinyl alcohol

RIL - Repeated Impulse Leutner

THB - Through Hole Bonding

VIF - Variance Inflation Factor

LIST OF SYMBOLS

A_{gm} - Geogrid mesh area

$A_{initial}$ - Initial area

B_c - Bitumen coating

B_{cc} - Bitumen content coating

D - Specimen diameter

E_D - Total accumulated dissipated energy

G - Shear modulus

Gsa - Apparent specific gravity

Gsb - Bulk specific gravity

h - Thickness

$ISS_{f\text{-}predicted}$ - Interface shear strength of specimen extracted from field

$ISS_{l\text{-}predicted}$ - Interface shear strength of laboratory-prepared specimens

ISS_{meas} - Sample's average value of interface shear strength

ISS_{min} - Minimum interface shear strength value required

ISS_{tm} - True mean of interface shear strength

k - Interface shear stiffness modulus

$k_{s,d}$ - Design cyclic interface shear stiffness modulus

$k_{s,n}$ - Cyclic interface shear stiffness modulus

N_f - Shear fatigue life

$N_{f,c}$ - Number of cycles corresponding to complete debonding

N_{sfn} - Shear flow number

P_{max} - Load peak

R^2 - coefficient of determination

T_{fb} - Thickness of the fabric backing

T_g - Thickness of the geosynthetic pavement interlayer

ΔF_n - Amplitude of the applied shear force

Δu - Relative shear displacement

Δu_n - Amplitude of the relative shear displacement

$\Delta \tau$ - Amplitude of the shear stress

τ - Shear stress

τ_{max} - Maximum shear stress

ϕ - Correction coefficient

φ_n - Phase angle

ω^2 - Omega squared

LIST OF CONTENTS

CHAPTER 1. INTRODUCTION 22

1.1 Statement of the problem 22

1.2 Main research objective 24

1.3 Specific research objective 24

CHAPTER 2. RESEARCH BACKGROUND 25

2.1 Paving geosynthetics within asphalt overlays 25

2.2 Interface bonding between asphalt layers 27

2.3 Tests for interface bond evaluation: modes of failure, testing devices, procedures, parameters, and specifications 29

2.4 Factors influencing the interface bonding properties of asphalt overlays with and without paving geosynthetic 39

2.4.1 Influence of test configuration 39

2.4.2 Influence of specimen characteristics 43

2.4.3 Influence of interface characteristics 46

2.4.3.1 Tack coat type 46

2.4.3.2 Tack coat rate 49

2.4.3.3 Texture and interface conditions 51

2.4.3.4 Influence of paving geosynthetic on the interface bonding: types, physical properties, and mechanical properties 52

2.5 Interface shear fatigue: testing devices, procedures, parameters, and rupture criteria 54

2.5.1 Studies regarding shear fatigue test: influencing factors and correlation with monotonic interface shear test 65

CHAPTER 3. MATERIALS 71

3.1 Asphalt mixture 71

3.2 Tack coat 74
3.3 Paving geosynthetics 75
3.3.1 Paving composites and paving mat 75
3.3.2 Paving geogrids 77
3.3.3 Geosynthetic properties 78
CHAPTER 4. DOUBLE-LAYERED ASPHALT SPECIMENS WITH PAVING GEOSYNTHETICS 83
4.1 Compaction method 83
4.2 Specimen preparation 84
CHAPTER 5. INTERFACE SHEAR BOND TEST 87
5.1 Multifunctional interface shear testing device 87
5.2 Leutner shear tests 89
5.3 Procedure for determining minimum interface shear strength 90
5.4 Experimental program for interface shear bond tests 92
CHAPTER 6. SHEAR FATIGUE TEST 94
6.1 Dynamic testing machine 94
6.2 Dynamic testing machine validation 97
6.3 Proposed test method and analysis procedures 98
6.3.4 Procedure 99
6.3.5 Calculation and interpretation of results 101
6.3.5.1 Result charts 103
6.3.5.2 Approaches to determine the failure point 106
6.3.6 Precision and Bias 108
6.4 Experimental program for shear fatigue tests 108
CHAPTER 7. INTERFACE SHEAR BOND TEST RESULTS AND ANALYSIS 109

7.1 Interface shear stress-displacement curve 109
7.2 Results and analysis of Interface shear strength 111
7.3 Evaluation of the significant factors for interface shear strength 112
7.4 Multiple linear regression analysis for Interface shear strength 114
7.5 Analysis of the Multiple linear regression models for Interface shear strength 118
7.6 Verification of the MLR models and prediction of Interface shear strength 124
7.7 Prediction of interface shear stiffness modulus based on interface shear strength 126
CHAPTER 8. SHEAR FATIGUE ANALYSIS 129
8.1 Effect of tack coat type on shear fatigue 129
8.2 Effect of tack coat rate on shear fatigue properties 131
8.3 Effect of test frequency on shear fatigue properties 134
8.4 Effect of different paving geosynthetics on shear fatigue properties 136
8.4.1 Multiple linear regression analysis for shear fatigue life based on geosynthetic properties 140
8.5 Correlation between shear fatigue life and interface shear strength 144
CHAPTER 9. CONCLUSIONS AND RECOMMENDATIONS 147
9.1 Conclusions 147
9.2 Recommendations for future work 148
REFERENCES 149

CHAPTER 1. INTRODUCTION

1.1 Statement of the problem

The application of paving geosynthetics within asphalt overlays has been a widely used technique in pavement rehabilitation. Its primary objectives are to mitigate the development of thermal and reflective cracking, as well as to reduce degradation caused by water infiltration. Several studies further indicate that the presence of paving geosynthetics in asphalt overlays can help reduce the magnitude of rutting, as well as decrease stresses in the lower asphalt layers. However, the presence of paving geosynthetics may reduce the bonding between asphalt layers and, consequently, impact pavement performance (Canestrari et al., 2022b; Correia et al., 2023; Correia and Mugayar, 2021; Ge et al., 2015; Sagnol et al., 2019; Solatiyan et al., 2021a). According to Canestrari et al. (2022), the correct assessment of interface bonding between asphalt layers is crucial for estimating the service life of the pavement structure, especially when paving geosynthetics are employed within asphalt overlays.

The current version of the European specification pr-EN 12.697-48 (European Standard, 2021) considers the possibility of using three types of tests to quantify the interface bonding between asphalt pavement layers: torque, shear, and tensile. Among these three tests, Petit et al. (2018a) state that the in-plane shear mode evaluates the most common cause of failure between the layers. This type of test allows for determining the shear strength and the stiffness modulus of the interface. Investigations of asphalt pavements have shown that diverse factors influence the interface bonding properties. These factors include the type of tack coat, the tack coat rate, the surface condition (milled or not milled), and the temperature (Mohammad et al., 2018; Sufian et al., 2021; Yang et al., 2021).

The evaluation of the interface bonding behavior between asphalt layers with paving geosynthetics has been discussed in the literature. Safavizadeh et al. (2020) indicated that the type of tack coat affects interface bonding, while Noory et al. (2019a) found that the macrotexture of the asphalt mixture surface has little impact on interface bonding when paving geosynthetics are used at the interface. Correia and Mugayar (2021) studied the effect of different tack coat rates and the physical properties of paving geosynthetics on interface bonding behavior. Properties such as the geogrid mesh size, the thickness of the geosynthetic, geosynthetic coating type, the presence of

fabric backing, and tensile stiffness are indicated as factors that influence the interface bonding behavior of asphalt overlays with paving geosynthetics (Correia e Mugayar, 2021; Kumar e Saride, 2017; Noory et al., 2019a; Sagnol et al., 2019; Sudarsanan et al., 2018a; Walubita et al., 2018).

The geosynthetic industry has increasingly innovated in developing products specifically for use in asphalt rehabilitation applications. Thus, there are other factors that may affect interface bonding properties, such as the presence bitumen coating in the geosynthetic, the bitumen coating content, as well the presence of fabric strips crossing the paving geogrid mesh. However, studies involving the evaluation of interface bonding in asphalt overlays with paving geosynthetics have primarily focused on monotonic interface shear bond tests.

The cyclic shear stiffness modulus of the interface is indicated as a useful parameter for predicting the bearing capacity of the pavement structure. Although monotonic interface shear bond tests have been widely used, since the traffic loads applied to the pavement are dynamic, cyclic tests between asphalt layers should lead to more realistic predictions. However, due to the scarcity of studies and the lack of standardization in shear fatigue tests, the study of Canestrari et al. (2022), published by the RILEM Technical Committee 272-PIM, proposes gathering information on equipment and testing protocols to characterize the cyclic behavior of bituminous interlayers. Similar to the observed in monotonic interface shear bond tests, diverse factors affect the results of interface shear fatigue tests, such as test configurations, frequency and amplitude of the load pulse (Miró et al., 2021; Nian et al., 2020; Song et al., 2016; Tozzo et al., 2014b; Wang et al., 2017; Yang et al., 2020).Due to the complexity of dynamic shear tests and the challenges in conducting them, research has been carried out with the aim of establishing correlations between monotonic and shear fatigue tests (Yang et al., 2020), however, focusing on asphalt overlays without paving geosynthetics. Among the few studies that have evaluated the behavior of asphalt overlays with paving geosynthetic under cyclic shear load are the research of Donovan et al. (2000), and Safavizadeh et al. (2022a), which demonstrate the presence of paving geosynthetic within asphalt overlays influence the interface shear fatigue behavior, as well as tack coat rate, and geogrid mesh size.

While numerous studies have delved into the cyclic behavior of bituminous interlayers, limited knowledge exists regarding the shear bond behavior of asphalt overlays with paving geosynthetics in various configurations of monotonic and cyclic interface shear bond tests. Previous research has provided valuable insights into the factors affecting the interface bond

strength with paving geosynthetics, although primarily focusing on assessing isolated geosynthetic parameters on interface bond properties. Thus, there is a gap in identifying synergistic impacts resulting from the combination of geosynthetic and tack coat characteristics on the behavior of bituminous interlayers.

This research aims to fill these knowledge gaps and contribute to the understanding of the effects of multiple factors on monotonic interface bond and shear fatigue parameters, as well as the relationship of the significant factors with the interface bond and shear fatigue parameters. To evaluate monotonic interface bond and shear fatigue parameters, a multifunctional interface shear testing device was developed. This device was used to conduct monotonic interface bond and shear fatigue tests, considering a diverse range of paving geosynthetics with varying properties, in conjunction with different tack coat types and rates.

1.2 Main research objective

To evaluate the effect of multiple factors on monotonic interface bond and shear fatigue parameters, as well as the relationship of the significant factors with the interface bond and shear fatigue parameters, considering a wide variety of paving geosynthetics with different properties, in combination with different tack coat types and rates.

1.3 Specific research objective

- To develop a dynamic testing machine and a multifunctional interface shear testing device for conducting tests with different configurations.
- To identify whether the tack coat type and rate, as well as the paving geosynthetic type, significantly affect interface shear strength and shear fatigue life.
- To identify the geosynthetic properties that most affect interface shear strength and shear fatigue life.
- To establish predictive models of interface shear strength and shear fatigue life for geosynthetic-reinforced systems based on geosynthetic physical properties.
- To establish correlations between monotonic interface bond and shear fatigue parameters for geosynthetic-reinforced systems.

CHAPTER 2. RESEARCH BACKGROUND

2.1 Paving geosynthetics within asphalt overlays

The use of paving geosynthetics within asphalt overlays emerged in the early 1980s and has since been increasingly used in pavement rehabilitation. The purpose of this technique is to mitigate the development of thermal and reflective cracks, as well as to reduce or eliminate degradation caused by water infiltration. Additionally, the paving geosynthetic can enhance fatigue life, improve resistance to rutting, extend the service life of a new asphalt layer, and enhance overall pavement performance (Correia and Zornberg, 2018; Jaskula et al., 2023; Khodaii et al., 2009; Kumar et al., 2021; Vinay Kumar et al., 2022; Roodi et al., 2017; Sudarsanan et al., 2020). While several studies have demonstrated that the presence of paving geosynthetics between an old and a new asphalt layer can effectively restrict crack growth in the new asphalt layer (Kumar and Saride, 2019; Kumar et al., 2022; Safavizadeh et al., 2015; Saride and Kumar, 2017; Kumar and Saride, 2017; Wargo *et al*., 2017), potential debonding or sliding of the interface has been indicated as side effect that can compromise the fatigue life and overall performance of the pavement (Brown et al., 2001; Canestrari et al., 2012, 2013; Ferrotti et al., 2012; Vanelstraete et al., 2004; Zamora-Barraza et al., 2010).

Therefore, the lack of bonding at the interface between the paving geosynthetic and surrounding asphalt layers is a critical factor to the overall performance of the asphalt pavement, whether caused by an excess or a lack of tack coat. If the upper asphalt layer is not fully bonded, it is susceptible to pathologies such as early cracking and asphalt layer delamination (Chen and Huang, 2010; Mohammad et al., 2012; Sudarsanan et al., 2018b). Figure 2.1 illustrates a case at the Salvador International Airport, Bahia, Brazil, where lack of bonding between the paving geosynthetic and the surrounding asphalt layers led to asphalt layer sliding.

In the last decade, the evaluation of the interface bonding behavior between paving geosynthetics and the surrounding asphalt layers has been discussed in the literature (Correia et al., 2023; Correia and Mugayar, 2021; Kumar and Saride, 2017a; Kumar et al., 2023; Noory et al., 2019; Safavizadeh et al., 2022a; Sagnol et al., 2019; Sudarsanan et al., 2018b; Walubita et al., 2018). Studies show that different factors affect bond strength in geosynthetic-reinforced asphalt

overlays, but with potential debonding being a manageable side effect influenced by ideal tack coat type and rate, as well as installation process and geosynthetic characteristics.

.

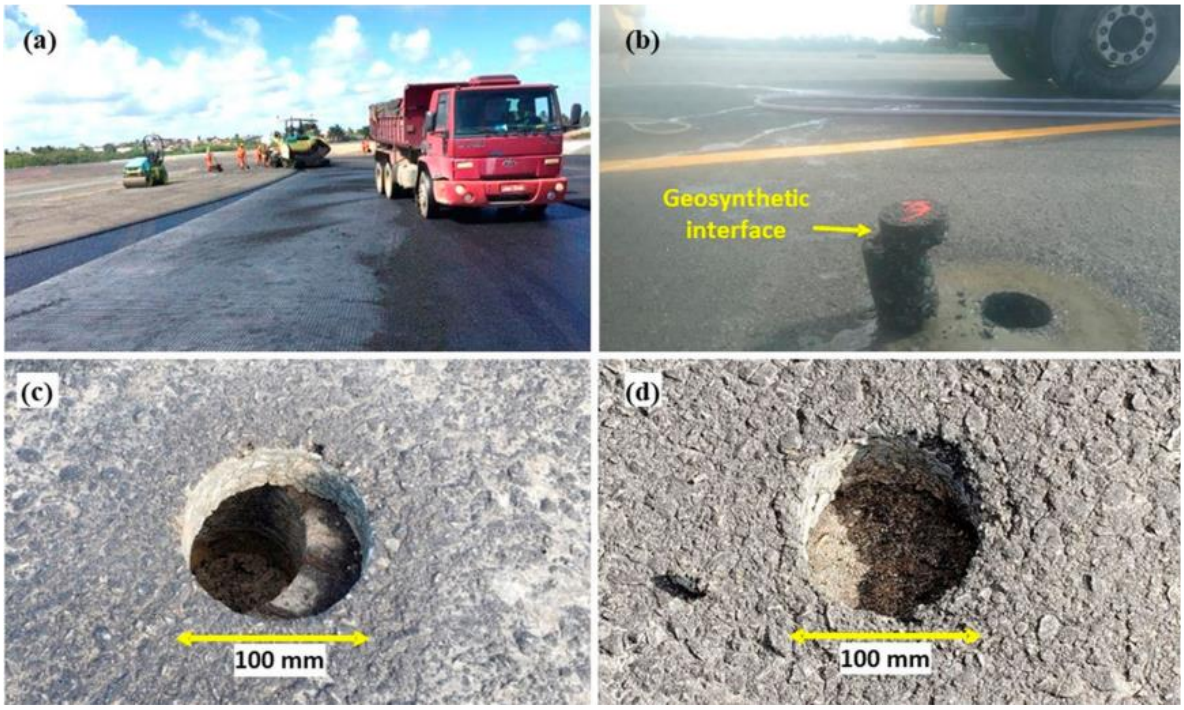

Figure 2.1 – Case study at Salvador International Airport: (a) installation process, (b) extracted field core specimen showing debonding, (c) asphalt layer slippage failure at geosynthetic interface, and (d) hole from specimen extraction closed after slippage. Source: Correia et al. (2023).

The selection of an ideal tack coat and application rate is crucial in developing adequate bond strength (Mohammad et al., 2012). Walubita et al. (2018) indicate that the increasing use of paving geosynthetics makes the bonding between asphalt layers even more critical aspect for the selection of asphalt mixtures and tack coats. Leite-Gembus e Elsing (2020) suggest that the proper application of paving geosynthetics within asphalt layers requires a higher tack coat rate at the interface compared to conventional asphalt overlays, but this would lead to a stress-reducing effect, allowing deformations, which it was called "flexible bond". In this regard, there is a consensus that the quality of the interface bonding is the crucial factor in the mode of failure and is related to the performance of the asphalt overlays.

2.2 Interface bonding between asphalt layers

Two questions can be asked about the phenomenon of adhesion. The first is related to what keeps two bodies together. The second concerns the forces that must be applied to separate two bonded bodies. These two questions, initially brought by Newton in 1730, are addressed, respectively, by fundamental adhesion and practical adhesion. Fundamental adhesion refers to the forces and mechanisms involved in the bonding of different components at a molecular scale. On the other hand, practical adhesion deals with the magnitude of the mechanical force or the amount of energy that must be applied to break the bonding between two bodies (Silva et al., 2018). For engineers, practical adhesion is relevant when evaluating failure in service or in laboratory tests. It can be measured in terms of strength (force or stress), modulus/stiffness, or work/energy (White, 2017).

The bonding substantially affects the performance of the pavement structure and the stress-strain distribution (Ge et al., 2015; Hu et al., 2017; Kim et al., 2011). However, design methods are based on fatigue or permanent deformation criteria, considering fully bonded layers (Diakhate et al., 2006; Roussel et al., 2022), which does not align with reality, as the interface bonding can be considered partial (Yang and Li, 2021). According to Romanoschi and Metcalf (2001), if the interface bonding condition were taken into account in the design, pathologies related to the interface could be reduced or eliminated. In this regard, theoretical investigations have been carried out to assess the correct bearing capacity of the pavement.

Several software can be used for modeling pavement structures. This process can be accomplished through the use of constitutive material laws and appropriate pavement behavior models, allowing the evaluation of stress-strain distribution (Canestrari et al., 2013). According to Roque et al. (2017), the theory of elasticity has been assumed to describe the mechanical behavior of the interface, which is considered as a thin material with a shear modulus (G) and thickness (h). Thus, the shear stress (τ) between layers resulting from loading forces induces a relative shear displacement (Δu). Figure 2.2 shows the schematic of relative displacement between two bonded layers The relationship between these parameters is presented in Equation 2.1:

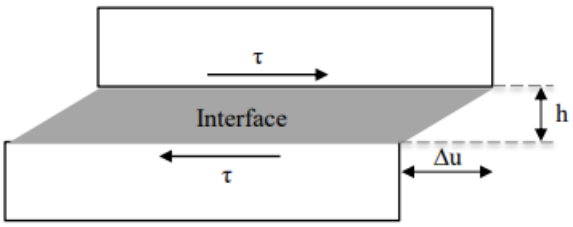

Figure 2.2 – Schematic of relative displacement between two bonded layers. Source: Roque et al. (2017).

$$\tau = G \cdot \frac{\Delta u}{h} = G \cdot \gamma \tag{2.1}$$

Where γ is the shear strain for an interlayer material. From Equation 2.1, the well-known constitutive law of Goodman (Goodman et al., 1968) is derived. This law describes the behavior of the interface in an elastic multi-layered structure, as demonstrated in Equation 2.2.:

$$\tau = k \cdot \Delta u \tag{2.2}$$

In equation 2.2, *k* arises from the ratio between *G* and *h* and represents the interface shear stiffness modulus, commonly expressed in MPa/mm.

In modeling, a higher value of *k* indicates a tendency toward complete adhesion at the interface, while a value of *k* close to zero suggests a tendency towards complete slippage (Yang e Li, 2021). Yang e Li (2021) highlight the interface shear stiffness modulus as a useful variable for understanding the behavior of interface bonding up to the point of failure. For this reason, it has been employed by several authors to assess the effects of varying levels of bonding on the stress-strain distribution of the pavement, both under static and dynamic loading conditions (Ortiz-Ripoll et al., 2020; Ozer et al., 2012; Ragni et al., 2021; Romanoschi e Metcalf, 2001; Uzan et al., 1978).

The influence of interface bonding on stress distribution was studied by varying different values of *k* at the interface between the asphalt layer and the base of a structure consisting of three layers over a soft subgrade (Uzan et al., 1978). In this research, it was discovered that the most significant change in stress magnitude and deformation at the bottom of the asphalt layer occurred when *k* ranged between 1 and 10^2 MPa/mm. Furthermore, it was demonstrated that an increase in the interface shear stiffness modulus value brings the deformation closer to the calculated value for

a fully bonded interface. Figure 2.3 shows the distribution of strain vs. depth for different interface shear stiffness.

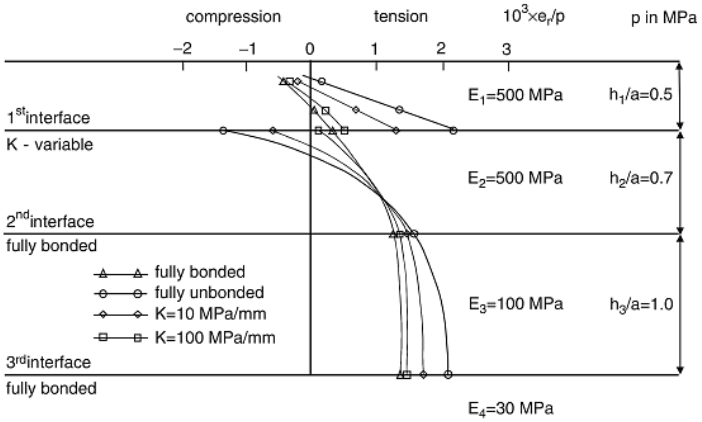

Figure 2.3 – Distribution of strain vs. depth for different interface shear stiffness. Source: Canestrari et al. (2013).

From a practical point of view, stiffness assessment can be performed through back-calculation analysis using measurements from the Falling Weight Deflectometer (Canestrari et al., 2013). Due to a practical limitation in most back-calculation analysis, which assume complete bonding between layers, Al Hakim (2002) developed a novel approach to determine the modulus of stiffness. This method has been applied to various pavement structures representing field conditions, including thermal and material variations. Two threshold values for *k* were identified: below 10^{-2} MPa represented perfect sliding conditions, and above 10^2 MPa indicated perfect bonding, while the actual condition lies between these two limits. These considerations have been recognized by different authors(Canestrari et al., 2013; Correia et al., 2022; Yang e Li, 2021). Therefore, a correct assessment of the interface bonding conditions between asphalt layers is crucial for accurately determining the pavement bearing capacity, using available methods for rational design and maintenance of flexible pavement.

2.3 Tests for interface bond evaluation: modes of failure, testing devices, procedures, parameters, and specifications

The existing tests to evaluate interface bonding consider the modes of failure that occur in the field. According to Rahman et al. (2017), the interfaces of pavement layers are subject to

different failure mechanisms: pure shear, pure tension, shear-compression, and shear-tension. Figure 2.4 illustrates these different interface failure conditions.

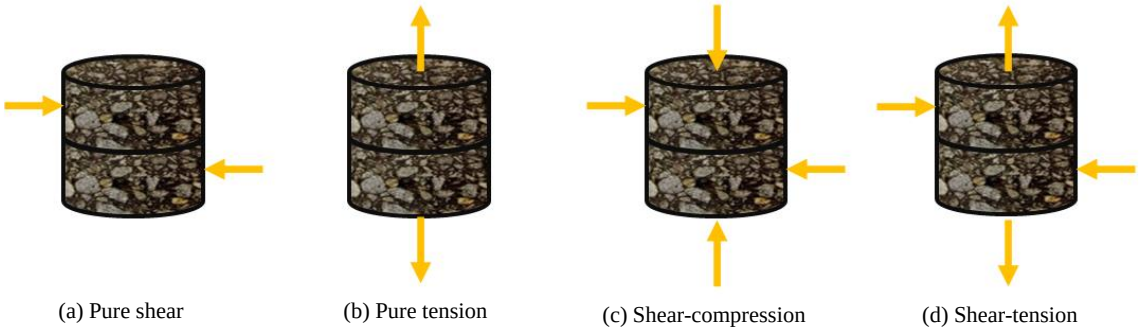

Figure 2.4 – Different modes of failure at asphalt interface: (a) pure shear, (b) pure tension, (c) shear-compression, (d) shear-tension.

The modes of pure shear or shear-compression can occur in both longitudinal and transverse directions, being caused by traffic or shearing stresses resulting from temperature. (Nottingham and User, 2010). Vertical tensile stresses are generated as a result of the gas expansion phenomenon (blistering), which is due to retained moisture or microbial activity at the interface, as well as tire suction between the layers. This condition can be observed when a concrete overlay is superimposed by an asphalt layer (Brown e Darnell, 1987; Hironaka e Holland, 1987; Raab et al., 2009). When the interface bonding below a thin layer is weak, horizontal loadings concentrate on the upper layer, resulting in buckling of the overlay ahead of the tire. In this case, both axial stress and shear stress are induced by horizontal loading (Nottingham and User, 2010). However, the buckling phenomenon rarely occurs in a real pavement structure. Figure 2.5 depicts the field mechanism of bond failures.

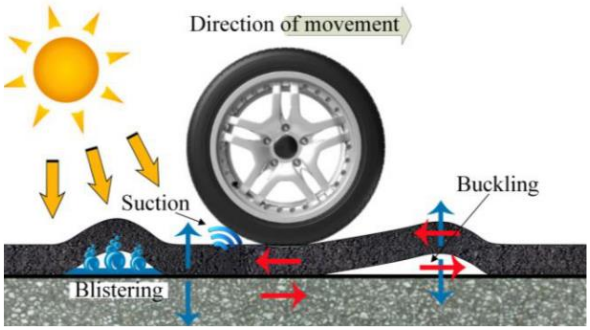

Figure 2.5 – The field mechanism of bond failures. Source: Sudarsanan et al. (2016).

Currently, there are diverse types of tests and testing devices to evaluate the different mechanisms. For this reason, the RILEM Technical Committee 241 – MCD (Petit et al., 2018) proposed classifying existing interface bonding tests into four categories: opening mode (Mode I); in-plane shear mode (Mode II); out-of-plane shear mode (Mode III); and the combination of modes I and II (Mixed Mode). Figure 2.6 presents the different test methods for interface bonding evaluation.

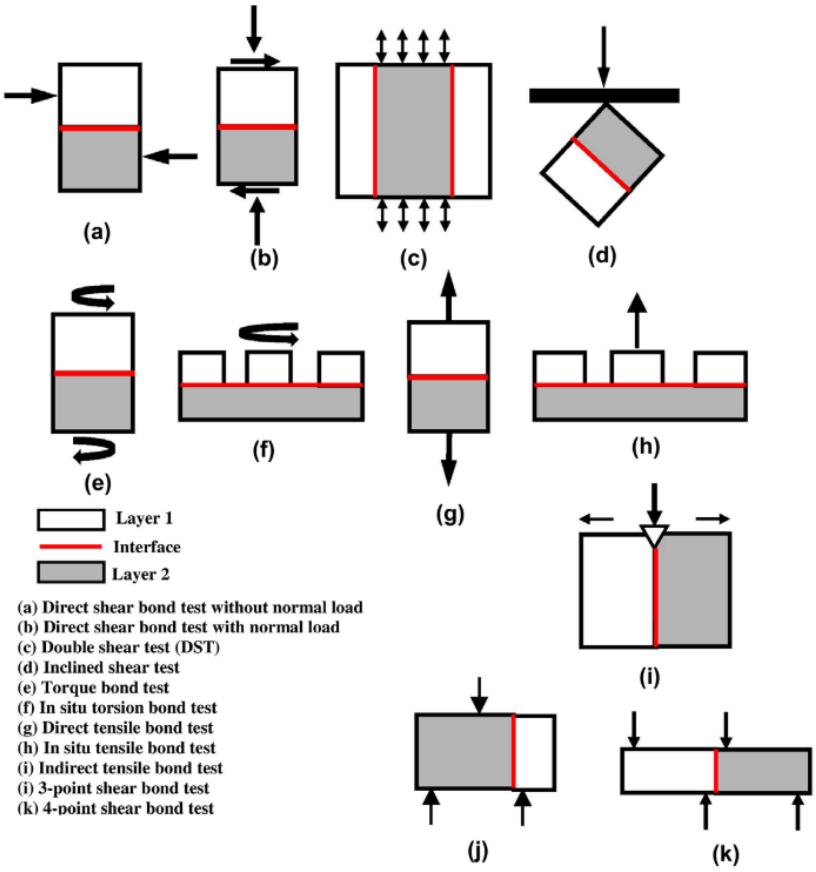

Figure 2.6 – Different test methods for interface bonding evaluation. Source: Rahman et al. (2017).

Mode I evaluates the phenomenon of delamination created through tensile loading, with Tensile Bond Tests and Tensile Notch Bond Tests as the main types of testing devices. Mode II considers damage to the interface caused by shear loading. Tests of this type can be conducted with or without normal loading. Mode III encompasses the torque test, which can be performed in the field or in a laboratory. Mode IV comprises tests conducted through three-point or four-point bending. The current version of the pre-European standard pr-EN 12.697-48 (European Standard,

2021) considers the possibility of using three types of tests to measure the bond between layers: torsion, shear, and tension. Among these tests, Petit et al. (2018a) stated that shear mode in-plane assesses the most common cause of delamination between layers. Furthermore, it is the type of test that allows the determination of the interface shear stiffness modulus, following the constitutive law of Goodman.

Based on the publication by Uzan et al. (1978), the study and development of in-plane shear equipment were initiated. In 1979, Leutner developed a device to perform a pure shear test, in a guillotine style, characterized by the application of a constant displacement rate on double-layer cylindrical specimens until the failure of the interface (Leutner, 1979). Due to its simplicity and ease way to test, many researchers have adapted the Leutner test to suit their specific objectives. Notable adaptations of this device test include the Florida Department of Transportation Shearing Test, Layer-Parallel Direct Shear (LPDS), and the Modified Leutner test (Collop et al., 2009; Partl e Raab, 1999; Sholar et al., 2004). Among these adaptations, the LPDS test has been standardized in Switzerland (Swiss Standard, 2012), the United Kingdom (Highways England's standards and specifications, 2021), Austria, and Germany (FGSV, 2013), and various other countries for testing cylindrical specimens with diameters of 100 and 150 mm, with a displacement rate of 50 mm/min. According to Ortiz-Ripoll et al. (2020), this test is still referred to as a Leutner test in many countries. In Spain, the shear equipment is referred to as Device A, similar to the Leutner device, but the test is conducted at a displacement rate of 2.5 mm/min (NLT-382, 2008). Figure 2.7 illustrates the Leutner and LPDS devices.

(a) (b)

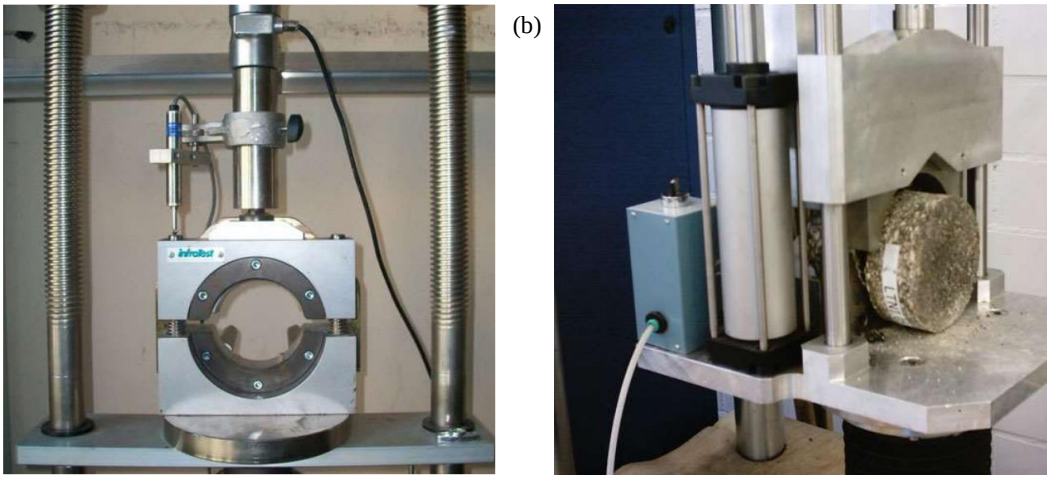

Figure 2.7 – Pure shear testing devices: (a) Leutner, (b) LPDS. Fonte: Canestrari et al. (2013).

Originally, in the Leutner device, there was no gap width between the shearing rings of the device, resulting in misalignment of the interface in the shear plane, especially for specimens with irregular interfaces (Rahman et al., 2017). In order to overcome this issue, Choi et al. (2005) were the first to introduce a gap of 5 mm and noted the positive effect on the test. Collop et al. (2005) revealed that introducing a gap reduced the variability of the results. European standards recommend a gap of less than or equal to 5 mm, while the research by Raab et al. (2010) suggests that 3 mm appears to be ideal for considering layers with larger maximum aggregate sizes and irregularities in the interface. The resulting output is a shear stress-displacement curve, from which the interface shear strength (*ISS*), interface shear stiffness modulus (*k*), and interface shear fracture energy (*ISFE*) can be obtained.

Regarding the *ISS*, as determined by Equation 2.3, the primary divergence to consider is whether the area used to calculate the strength should be the initial area or the contact area at the moment of rupture. Many researchers have not explicitly specified which area was considered in their calculations of *ISS* (Hu et al., 2017; Lee et al., 2020; Mohammad et al., 2010, 2009, 2002; Raab e Partl, 2009; Ragni et al., 2019; West et al., 2005). However, Pasetto et al. (2019) propose the use of the initial area to calculate *ISS*. According to White (2017), employing the area at the moment of rupture leads to an approximate 5% increase in the *ISS*.

$$ISS = \frac{P_{\max}}{A_{Initial}} = \tau_{\max} \tag{2.3}$$

Where *ISS* is the interface shear strength, P_{max} is the load peak, $A_{initial}$ is the initial area, and τ_{max} is the peak shear stress.

Concerning to the interface shear stiffness modulus, which is determined by the ratio between the *ISS* and the shear displacement (Equation 2.4), there is no consensus in the literature regarding the maximum shear displacement (Δu) to be considered. Some researchers have used the displacement corresponding to the peak stress. This approach assumes a secant line connecting the origin of the stress-displacement graph to the peak stress point, which is not a standard practice (Bae et al., 2010; Lee et al., 2019; Mohammad et al., 2012). Other researches have considered that the displacement gradient (Δu) starts at the intersection between the extension of the linear portion of the graph and the abscissa axis (Correia e Mugayar, 2021; Isailović e Wistuba, 2018; Raab e

Partl, 2009; Sudarsanan et al., 2018a). This second approach is in accordance with the recommendations of pr-EN 12.697-48 (European Standard, 2021). Figure 2.8 illustrates the shear stress-displacement curve and this second approach.

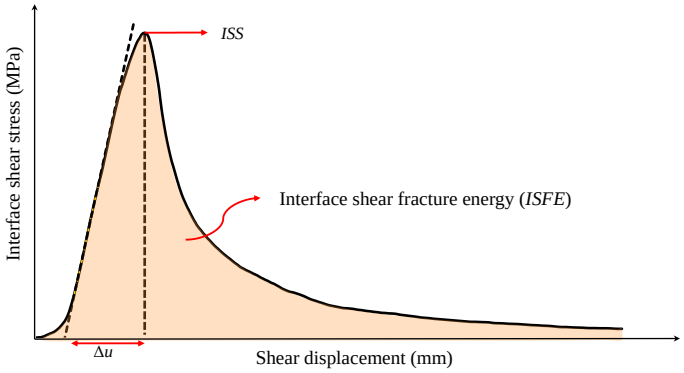

Figure 2.8 – Shear stress-displacement curve.

$$k = \frac{ISS}{\Delta u} \tag{2.4}$$

The interface shear energy (*ISE*) is determined by calculating the area under the shear stress-displacement curve, as per Equation 2.5. Santagata et at. (2009) used the energy up to the stress peak to calculate an equivalent shear displacement. Santagata et at. (2009), as well as Romanoschi and Metcalf (2002) suggested that the *ISE* after the peak load is dominated by the frictional properties of the interface. Lee et al. (2019) determined the *ISE* up to the displacement corresponding to zero shear stress at the end of the test, which it is known as interface shear fracture energy (*ISFE*). The *ISFE* is a useful parameter for comparing differences in interface shear bond after the occurrence of the peak load for specimens with similar *ISS* and *k* values(White, 2017).

$$ISE = \sum(\tau \cdot \Delta d) \tag{2.5}$$

Where *ISE* is the interface shear energy [kJ/m²], τ is the shear stress [MPa] related to a small shear displacement gradient (Δd) [mm].

Despite the widely use of pure shear test being in different countries, many researchers argue that the application of normal stress represents the effect of traffic loading on a highway and

should be included in interface shear bond tests (Canestrari et al., 2005; D'Andrea et al., 2013; Mohammad et al., 2009; Romanoschi e Metcalf, 2001; Santagata et al., 1993; Zofka et al., 2015). Studies on the importance of normal stress for interface shear failure have revealed that using interface shear strength without the application of normal stress leads to a conservative evaluation of interface shear strength (Karshenas et al., 2014; Mohammad et al., 2009), which may be acceptable for the purpose of controlling and ensuring the quality of the interface bonding. Karshenas et al. (2014) emphasize the importance of conducting a pavement analysis to use a normal stress that accurately represents in-situ pressure, considering environmental conditions and traffic loads.

However, according to Petit et al. (2018a), many of the testing devices developed to introduce normal stress produce highly variable results or require complex biaxial loading structures. The most well-known ones are the Ancona Shear Testing Research And Analysis (ASTRA) (Santagata et al., 1993), which complies with pre-EN 12.697-48 (European Standard, 2021) and is standardized in Italy (UNI/TS 11214, 2007), and the Louisiana Interface Shear Strength Tester (LISST) (Mohammad et al., 2009), approved by AASHTO TP 114-18 (2018). Figure 2.9 illustrates ASTRA and LISST devices.

(a) (b)

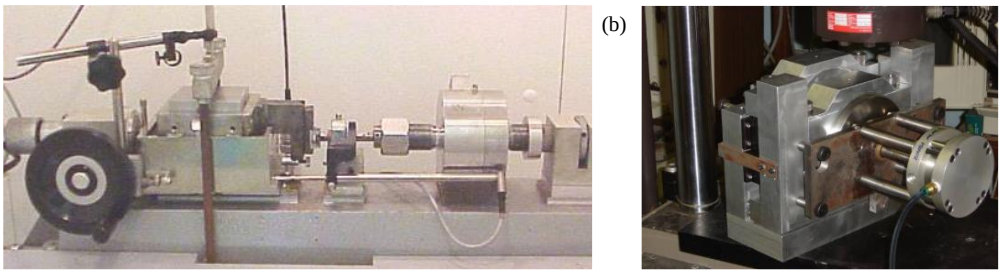

Figure 2.9 – Interface shear testing devices with application of normal stress: (a) ASTRA, (b) LISST. Source: a) Canestrari et al. (2013); b) Mohammad et al. (2009).

The procedure involves tests using ASTRA and LISST devices conducted at a displacement rate of 2.5 mm/min, which is lower than the displacement rate applied in the Leutner shear test procedure. The LISST device allows for testing specimens with diameters of 100 and 150 mm, while ASTRA enables testing with prismatic samples measuring 100 mm x 100 mm or cylindrical samples with a diameter of 100 mm, with the latter geometry being more common (Canestrari et al., 2018, 2022b; Canestrari and Santagata, 2005; Chen and Huang, 2010; D'Andrea et al., 2013; Partl et al., 2009; Ragni et al., 2019; Santagata et al., 2008, 2009) and is endorsed by pr-EN 12.697-

48 (European Standard, 2021). Originally, the LISST test was conducted without lateral confinement and under a normal stress of 0.138 MPa (Mohammad et al., 2012). However, the AASHTO TP 114-18 (2018) allows for applying a normal stress up to 0.21 MPa.

The ASTRA device has already been used with different levels of normal stress. In this case, the parameters *ISS*, *k*, and *ISFE* can be determined for each applied normal stress level. Furthermore, several researchers (Canestrari et al., 2018; Canestrari e Santagata, 2005; Chen e Huang, 2010; D'Andrea et al., 2013; Santagata et al., 2008) have confirmed that the relationship between shear stress at failure and normal stress can be expressed by a linear function, employing the Mohr-Coulomb principle.

Despite the different parameters obtained in tests with or without normal stress and theoretical studies indicating stiffness modulus as the parameter of interest, existing regulations in various countries have adopted shear strength alone to establish minimum specification limits. Only a few European countries that have established minimum limits have adopted the Leutner device or LPDS as the standard. In Germany (FGSV, 2013) and Switzerland (Swiss Standard, 2012), the standards specify that the laboratory tests should be conducted on field-extracted specimens with a diameter of 150 mm, at a temperature of 20°C, and a test speed of 50 mm/min, requiring an *ISS* of 0.85 MPa (15 kN) between the surface layers (wearing course/binder layer). Authors such as Raab and Partl (1999), as well as Stöckert (2001) suggest values of 1.3 and 1.41 MPa, respectively, for surface layers based on their research.

In the United Kingdom, an $ISS \geq 1.0$ MPa (17.7 kN) is required for interfaces located at a depth of ≤ 75 mm, and an $ISS \geq 0.5$ MPa (8.85 kN) is required for interfaces located at a depth of ≥ 75 mm (Highways England's standards and specifications, 2021). The test configurations are similar to those required in Germany and Switzerland. However, it is not specified whether the specimens are core field or specimens prepared in the laboratory. In Spain, the limits are $ISS \geq 0.6$ MPa (10.6 kN) when one of the layers is asphalt, and $ISS \geq 0.4$ MPa (7 kN) for all other cases (Ministerio de Transportes, Movilidad y Agenda Urbana, 2015). These values are for specimens extracted from the field, with a diameter of 100 or 150 mm and a displacement rate of 2.5 mm/min (NLT-382, 2008).

In Austria, the ÖNORM B3639-1 (Austrian Standards Institute, 1997) establishes criteria based on the type of tack coat. For interfaces with tack coats not modified by polymers, the minimum *ISS* values are 0.8 MPa (14.15 kN) between asphalt layers and 0.5 MPa (8.85 kN) for

other interfaces. When tack coats modified by polymers are used, the minimum *ISS* values are 1.2 MPa (21.2 kN) for asphalt layers and 1.0 MPa (17.7 kN) for other layers. In these cases, the specimens are extracted from the field and have a diameter of 100 mm. Despite the majority of European standards indicating the use of test specimens extracted from the field, the European recommendation pr-EN 12.697-48 (European Standard, 2021) establishes that tests can also be performed with specimens prepared in the laboratory.

In the United States, the NCHRP Project 09-40, titled 'Optimization of Tack Coat for HMA Placement' developed the LISST equipment, determined application methods and rates, as well as tack coat to be used in asphalt pavement interface applications. This study led to the establishment of the AASHTO TP 114-18 (2018), titled 'Standard Method of Test for Determining the Interlayer Shear Strength of Asphalt Pavement Layers'. In the report of NCHRP Project 712 (Mohammad et al., 2012), an *ISS* value of 0.28 MPa is documented as the minimum *ISS* required using the LISST device. However, this value is based on results derived from a Finite Element Analysis.

The NCHRP 09-40A Project, 'Field Evaluation of the Louisiana Interlayer Shear Strength Tester', was conducted to further validate the methodology developed in the previous project. The results of this project are presented in Report 878, titled 'Validation of the Louisiana Interlayer Shear Strength Test for Tack Coat' (Mohammad et al., 2018). In this report, 33 experimental sections in different states of the USA were evaluated, and the short-term performance of these structures was correlated with the measured *ISS*. In the end, a minimum *ISS* value of 0.28 MPa was confirmed for satisfactory field performance. This value was obtained from the analysis of tests conducted with a displacement rate of 2.5 mm/min, at 25°C, with a 12.7 mm gap, a 150 mm diameter, field-extracted specimens, and no application of normal stress. Figure 2.10 shows LISST test performed during NCHRP 09-40A project.

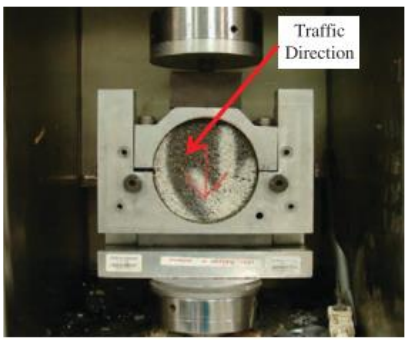

Figure 2.10 – LISST test performed during NCHRP 09-40A project. Source: Mohammad et al. (2018).

In Australia, specification MRTS104 (Department of Transport and Main Roads, 2021) requires a field test to verify whether the applied tack coat rate ensures adequate bonding between the paving geosynthetic and surrounding asphalt layer. However, there is currently no requirement for interface shear tests. The field test is conducted using a spring balance with a hook, which is used to pull the geosynthetic and detach it from the asphalt surface. If the balance reading is equal to or greater than 9 kg, the pavement service proceeds. Figure 2.11 illustrates the field test required in Australia for bond evaluation.

Figure 2.11 – Field test required in Australia for bond evaluation. Source: Department of Transport and Main Roads (2021).

In South America, the *Dirección Nacional de Vialidad* of Argentina (2017) establishes a minimum *ISS* value of 0.7 MPa between asphalt layers. Furthermore, it recommended interface shear bond tests according to pr-EN 12.697-48 (European Standard, 2021). In Brazil, the manual for the rehabilitation of asphalt pavements by the *Departamento Nacional de Infraestrutura de Transporte* (DNIT, 2006a) and the standards addressing this issue (DER ET-DE-P00/043, 2006; DNIT ES 145, 2010), whether with or without paving geosynthetics, only recommend the tack coat type and rate without establishing acceptance criteria regarding the *ISS*.

Despite the advancements addressed by the standards, all standards were developed based on studies that evaluated interface bonding for pavements rehabilitated without paving geosynthetics. Thus, the previous standards do not directly apply to asphalt overlays with paving geosynthetics. According to this was the reason for the German working group FGSV 770 (2013) to specify a minimum *ISS* requirement of 0.56 MPa (10 kN) to core fields of asphalt overlays with paving geosynthetics. In the literature, among the research results that evaluated asphalt overlays with paving geosynthetics, the *ISS* average values ranged from no bonding to 2.0 MPa (Correia et al., 2023; Correia and Mugayar, 2021; Ferrotti et al., 2012; Kumar et al., 2023; Leite-Gembus and

Elsing, 2020; Noory et al., 2019, 2017; Safavizadeh et al., 2022a; Solatiyan et al., 2021b; Spadoni et al., 2021; Sudarsanan et al., 2018b; Walubita et al., 2018). However, similar to asphalt interfaces without paving geosynthetics, the interface bonding properties for asphalt overlays with paving geosynthetics are influenced by various factors.

2.4 Factors influencing the interface bonding properties of asphalt overlays with and without paving geosynthetic

Understanding what influences the bonding between asphalt layers assists in the development of field methods and practices, in the improvement of the specification of different materials, as well as in the compatibility of different laboratory practices. The factors that affect the results of interface shear tests are related to different test configurations (shear device, test speed, application or not of normal stress, and temperature) and the characteristics of the specimens and the interface (Canestrari et al., 2013, 2021; Collop et al., 2009; Mohammad et al., 2018; Partl et al., 2009; Sufian et al., 2021; Walubita et al., 2018; White, 2017; Yang e Li, 2021). The characteristics of the specimens are relative to their origin, whether extracted from the field or fabricated in the laboratory, the diameter of the specimens, and the aging time. Regarding interface characteristics, it can be mentioned the tack coat type and rate, the surface condition (milled or not), the type of asphalt mixture, and the presence and type of paving geosynthetic.

2.4.1 Influence of test configuration

Ragni et al. (2019) evaluated the ASTRA and Leutner devices under the same testing conditions, using 100 mm specimens, a displacement rate of 2.5 mm/min, and a testing temperature of 20°C, without applying any normal force. The authors stated that the Leutner device induces higher resistance values compared to the ASTRA device. However, Ragni et al. (2019) only considered the average values without performing any statistical analysis to indicate a significant difference between the results. Figure 2.12 shows the comparison between *ISS* results obtained using Leutner and ASTRA devices. According to Canestrari et al. (2013), differences between results obtained from ASTRA and Leutner devices arise when different test configurations are used.

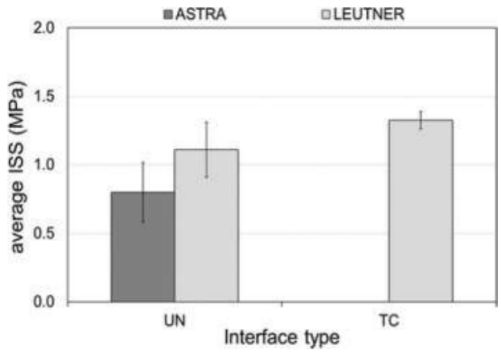

Figure 2.12 – Comparison between *ISS* results obtained using Leutner and ASTRA devices. Source: Ragni et al. (2019).

In the study by Uzan et al. (1978) it was found that the higher the displacement rate test, the higher are the *ISS* values. Sutanto et al. (2007) varied the displacement rate at 10, 50, and 100 mm/min and observed that the *ISS* varied by approximately 33%, proportionally to the applied rate. In the investigation conducted by Sholar et al. (2004) , there was a 55% increase in *ISS* when the rate was ranged from 19 mm/min to 50 mm/min.. Canestrari et al. (2013) carried out an evaluation of *ISS* involving five different displacement rate: 2.5 mm/min, 12.7 mm/min, 25 mm/min, 50 mm/min, and 200 mm/min, using a total of 77 specimens with a diameter of 150 mm on a Leutner device. The results indicated a power function with a high coefficient of determination ($R^2 = 0.99$), resulting in Equation 2.6 to correlate displacement rates. Ortiz-Ripoll et al. (2019) suggest that the equation provided satisfactory predictions, based on studies conducted on Leutner device following the NLT-382 (2008), at displacement rates of 2.5 mm and 50 mm/min. Figure 2.13 shows the correlation between shear displacement rate and ISS obtained by Canestrari et al. (2013).

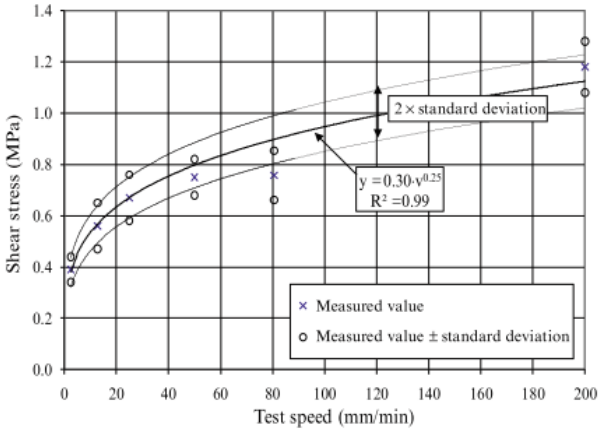

Figure 2.13 – Correlation between shear displacement rate and *ISS*. Source: Canestrari et al. (2013).

$$\tau_{vx} = \tau_{v1} \cdot \left(\frac{v_x}{v_1} \right)^{0,22} \quad (2.6)$$

Where τ_{vx} is the *ISS* at a displacement rate *x* (v_x), τ_{v1} is the *ISS* at known displacement rate (v_1).

Regarding to interface shear stiffness modulus (*k*), Ortiz-Ripoll et al. (2020) suggest the Equation 2.7, based on results obtained by Diakhaté et al. (2007).

$$k_{vx} = k_{v1} \cdot \left(\frac{v_x}{v_1} \right)^{0,45} \quad (2.7)$$

Where k_{vx} is the interface shear stiffness modulus at a displacement rate x (v_x), k_{v1} is the interface shear stiffness modulus at known displacement rate (v_1).

Various studies have demonstrated that the inclusion of normal stress in interface shear bond tests increases the interface shear strength following the Mohr-Coulomb principle. To study the influence of normal stress on the maximum shear stress, Canestrari et al. (2013) analyzed the results of 63 specimens extracted from three experimental sections, with a diameter of 100 mm, a displacement rate of 2.5 mm/min, and at three different temperatures. The regression analysis of the obtained results resulted in Equation 2.8, which allows for the determination of interface shear strength for a specific normal stress based on test results without normal stress.

$$\tau_{\sigma n} = (1 + 0,38 \cdot \sigma_n) \cdot \tau_{\sigma 0} + (0,74 \cdot \sigma_n) \quad (2.8)$$

Where $\tau_{\sigma n}$ is the interface shear strength with normal stress, $\tau_{\sigma 0}$ is the interface shear strength without normal stress, and σ_n is the normal stress.

Regarding the influence of normal stress on the interface stiffness modulus, the results from Canestrari et. al (2005) demonstrated that the values of *k* also exhibit a linear behavior with increasing normal stress. Ortiz-Ripoll et al. (2020) employed Equation 2.9 to propose a semi-empirical method for estimating shear stresses, stiffness modulus, and shear strength under service conditions.

$$k_{\sigma n} = \left(1 + 5\frac{\sigma_n}{\tau}\right) \cdot k_{\sigma 0} \tag{2.9}$$

Where $k_{\sigma n}$ is the interface shear stiffness modulus when normal stress is applied, σ_n is the normal stress, τ é the shear stress e $k_{\sigma 0}$ is the interface shear stiffness modulus without normal stress.

The test condition that can affect the bonding properties is the temperature, which is considered the most influential factor in the results (Noory et al., 2019). The literature indicates that an increase in temperature leads to a significant reduction in *ISS* (Canestrari et al., 2013, 2018; Mohammad et al., 2012; Partl et al., 2009; Safavizadeh et al., 2022a; Sufian et al., 2021; West et al., 2005). According to Partl et al. (2009), Canestrari et al. (2013), and Karshenas et al. (2014), this behavior follows a semi-logarithmic trend, as presented by Equation 2.10. Equations 2.7 to 2.10 were developed from studies of the interface between asphalt layers without paving geosynthetic. However, Canestrari et al. (2018) also studied the influence of temperature on the interface shear strength between asphalt layers with and without paving geosynthetic. The results, validated the semi-logarithmic trend proposed by Equation 2.10 and confirmed the significant reduction in interface shear strength for asphalt overlays with paving geosynthetic, due to the increase in temperature. Figure 2.14 shows interface shear strength behavior with the variation of displacement rate and temperature.

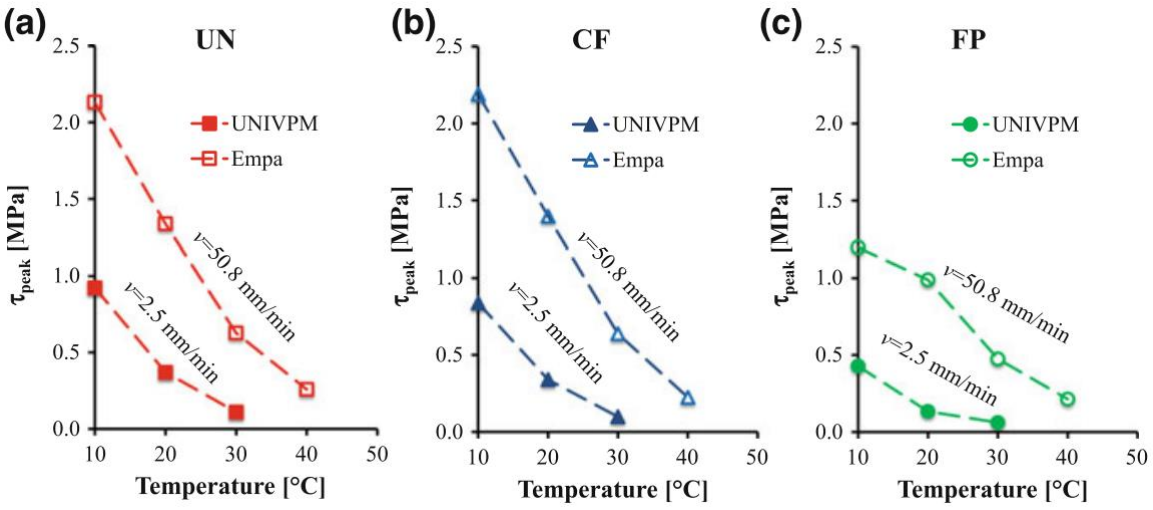

Figure 2.14 – Interface shear strength behavior with the variation of displacement rate and temperature: (a) asphalt overlays without paving geosynthetic, (b) asphalt overlays with paving geosynthetic (CF), (c) asphalt overlays with paving geosynthetic (FP). Source: Canestrari et al. (2018).

$$\log \tau_{pico} = a \cdot T + b \tag{2.10}$$

Where a e b are regression coefficients, $\tau_{\sigma n}$ is the peak shear stress and T is the temperature in Celsius degree.

Canestrari et al. (2021) reviewed Equations 2.7 and 2.9 in an investigation involving four paving geosynthetic. The tests were conducted on both field and laboratory specimens using the ASTRA device with a displacement rate of 2.5 mm/min and a normal stress of 0.2 MPa, as well as the Leutner device at displacement rate of 2.5 mm/min and 50.8 mm/min, without normal stress. Based on the obtained results, Canestrari et al. (2021) proposed Equations 2.11 and 2.12 for asphalt overlays with paving geosynthetics.

$$\tau_{Leut\,2,5} = \tau_{Leut\,50,8} \cdot \left(\frac{2,5}{50,8} \right)^{0,38} \tag{2.11}$$

$$\tau_{ASTRA} = (1 + 0,20 \cdot \sigma_n) \cdot \tau_{Leut\,2,5} + (0,73 \cdot \sigma_n) \tag{2.12}$$

Where $\tau_{Leut2,5}$ is the interface shear strength obtained using Leutner device at displacement rate of 2,5 mm/min, $\tau_{Leut50,8}$ is the interface shear strength obtained using Leutner device at displacement rate of 50,8 mm/min, τ_{ASTRA} is the interface shear strength obtained using ASTRA device, and σ_n is the normal stress.

2.4.2 Influence of specimen characteristics

Several studies have indicated that the method of obtaining specimens influences the *ISS* (Bahia et al., 2019; Canestrari et al., 2021, 2005; Collop et al., 2009; Mohammad et al., 2012, 2010; Raab et al., 2016; Sufian et al., 2021; Tran et al., 2012). Canestrari et al. (2005) evaluated the *ISS* results from specimens extracted from the field and laboratory-prepared specimens. The results revealed that laboratory-prepared specimens exhibit higher *ISS* values when compared to specimens extracted from the field. Figure 2.15 depicts the comparison between *ISS* obtained from field specimens and laboratory-prepared specimens.

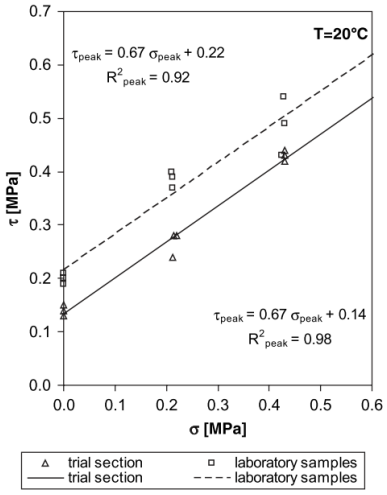

Figure 2.15 – Comparison between *ISS* obtained from field specimens and laboratory-prepared specimens Source: Canestrari et al. (2005).

However, there is no consensus regarding the magnitude of the increase in interface shear strength using field and laboratory-prepared specimens. Furthermore, some results in the literature demonstrate the inconsistency of this statement. Mohammad et al. (2012) reported an increase ranging from 2 to 10 times for samples produced in the laboratory. Tran et al. (2012) observed an increase of 2 to 2.5 times for specimens without tack coat at the interface; however, upon including the tack coat, some results showed equivalent or even lower *ISS* values for laboratory-prepared specimens. The results obtained by Sufian et al. (2021) indicated that depending on a combination of factors, there may be no statistically significant difference between specimens extracted from field and laboratory-prepared specimens. Canestrari et al. (2022) pointed out that specimens extracted from the field showed better adhesion results than those produced in the laboratory. However, when evaluating asphalt overlays with paving geosynthetic, field-extracted specimens exhibited lower *ISS* than laboratory-prepared specimens. Canestrari et al. (2022) justified this by stating that the geosynthetic installation in the laboratory was more appropriate. Furthermore, Canestrari et al. (2022) recommend an increase in the *ISS* minimum required value by 50% when using laboratory-prepared specimens with paving geosynthetic.

Other reasons are provided for the increasing trend in terms of *ISS* when it is obtained using laboratory-prepared specimens, Mohammad et al. (2012) suggested differences in the asphalt mixtures and the compaction and tack coat application methods as potential causes. Sufian et al.

(2021) added the effect of in-situ specimen extraction. To investigate this factor, Sufian et al. (2021) prepared 150 mm specimens and extracted 100 mm diameter specimens from them. The results indicated approximately a 25% reduction in *ISS* for field-extracted specimens. Figure 2,16 shows the influence of specimen extraction on the *ISS* obtained from specimens without paving geosynthetic.

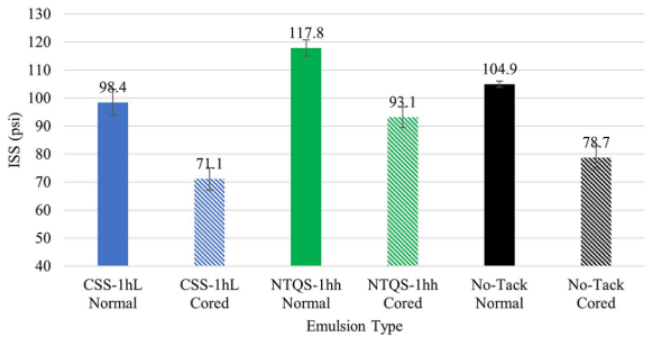

Figure 2.16 – Influence of specimen extraction on the *ISS* obtained from specimens without paving geosynthetic. Source: Sufian et. al. (2021).

However, when it comes to the same specimen preparation process, the variation in diameter has shown different impacts on the *ISS* results. Partl et al. (2009), and Canestrari et al. (2013) reported that specimens with a diameter of 100 mm exhibit higher *ISS* results when compared to those with a 150 mm diameter under the same test conditions. Canestrari et al. (2013) tested 616 specimens extracted from three different experimental sections, at a displacement rate test of 50 mm/min, and at three different temperatures (10, 20, and 30°C), and it was found a correlation between the results for asphalt overlays without paving geosynthetic, as demonstrated by Equation 2.13.

$$\tau_{D=100mm} = a \cdot \tau_{D=150mm} \tag{2.13}$$

Where a is a factor that depends on the interface condition, $\tau_{D=100mm}$ is the *ISS* for specimens with 100 mm in diameter, and $\tau_{D=150mm}$ is the *ISS* for specimens with 150 mm in diameter. The regression of all obtained results yielded an $R^2 = 0.97$, with a value of a equal to 1.14, meaning a 14% increase when reducing the diameter from 150 to 100 mm.

Zhang (2017) reported that the specimen aging tends to cause an increase in *ISS*. Sholar et al. (2004) evaluated a pavement structure that had undergone milling of the old asphalt layer, being replaced by two new asphalt layers bonded by an asphalt emulsion. The specimens were extracted along the wheel path over four days (1, 13, 40, and 99) after the structure's rehabilitation. Figure 2.17 illustrates the shear strength with respect to aging. For all the conditions investigated, the results indicated an increase in *ISS*, as depicted in Figure .2.17. Partl et al. (2009) reported an increase of up to 27% in *ISS* after an 18-month period. Canestrari et al. (2018) found that aging of asphalt overlays with paving geosynthetic resulted in an increase in *ISS*.

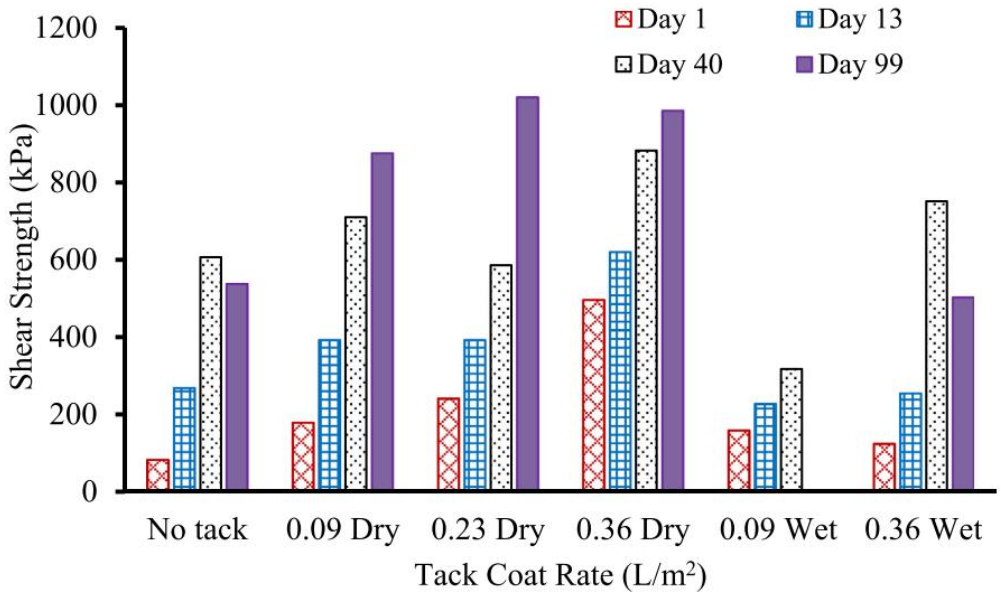

Figure 2.17 – Shear strength with respect to aging, based on US-90 project data. Source: Sholar et al. (2004).

2.4.3 Influence of interface characteristics

2.4.3.1 Tack coat type

Several researchers have reported that the tack coat type is an important factor for the bonding between asphalt layers (Canestrari et al., 2005; Mohammad et al., 2018, 2012; Safavizadeh et al., 2020; Sufian et al., 2021; Tran et al., 2012). However, there is still no consensus on which tack coat type provides the best interface bonding performance. Canestrari et al. (2005) evaluated three interface treatments (no tack coat, unmodified emulsion, and polymer-modified emulsion),

and at 20°C, modified emulsions induced better bonding results. However, at approximately 40°C, there was no significant difference in the bonding results.

In the study conducted by Mohammad et al. (2012) the influence of five types of tack coat, including PG 64-22, slow-setting emulsions, cationic rapid-setting emulsion (CRS-1), and polymer-modified emulsion, was investigated. The best performance in terms of *ISS* was observed with the polymer-modified emulsion, followed by PG 64-22 and CRS-1. In the other hand, in the research conducted by Tran et al. (2012), the interface with PG 64-22 as a tack coat exhibited performance similar to the interface with modified emulsion as a tack coat (NTSS-1HM).

Sufian et al. (2021) investigated the influence of temperature, surface texture, tack coat type and application rate; however, Sufian et al. (2021) performed an analysis of variance considering only the surface texture, and the tack coat type and rate. The results indicated that the tack coat type was the second most influential factor, followed by the application rate. Among the four emulsions studied, only the modified one (NTQS-1hh) showed a significant difference in terms of *ISS*. Figure 2.18 shows the effect of different types of emulsions on *ISS*.

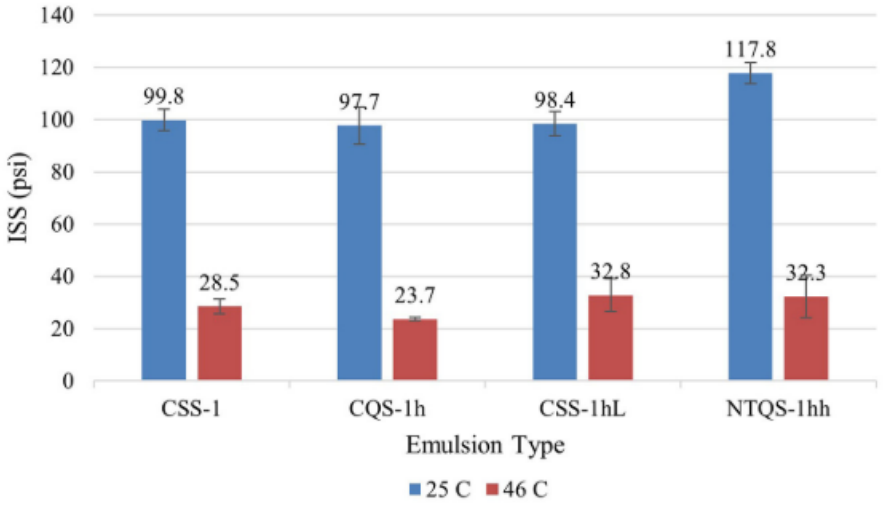

Figure 2.18 – Effect of different types of emulsions on *ISS*. Source: Sufian et al. (2021).

Yang et al. (2021) evaluated alternative tack coat types, including an epoxy resin, and tack coats modified by styrene-butadiene-styrene polymer. The results of interface bonding behavior demonstrated superior performance when applying epoxy resin, with no significant difference observed between the modified hot asphalt and the modified emulsion. Figure 2.19 presents the findings of this study.

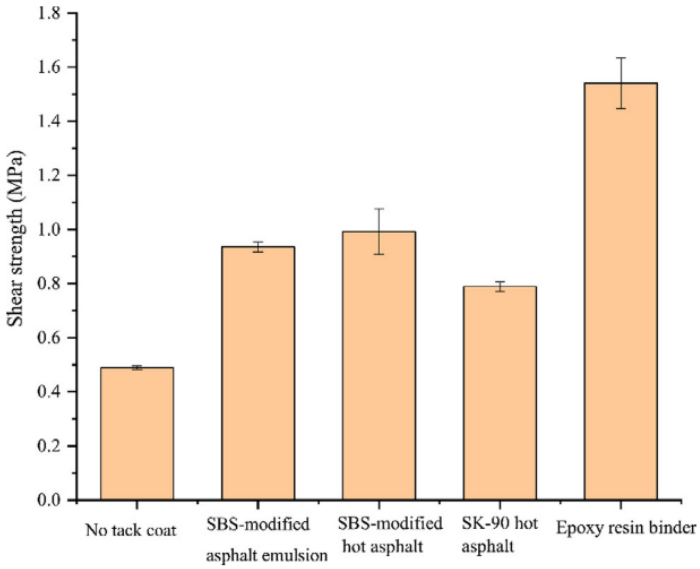

Figure 2.19 – Influence of different tack coat types on *ISS*. Source: Yang et al. (2021).

Covey et al. (2017) investigated the relationship between the rheological properties of six types of cationic emulsions CSS-1H and *ISS*. The results showed that higher viscosity and softening point values, as well as lower penetration values, induce better interface bonding behavior.

Although the literature presents various studies on the influence of tack coat type on interface bonding, few studies have addressed the influence of tack coat type on the *ISS* of asphalt overlays with paving geosynthetic. For instance, Safavizadeh et al. (2020) investigated the influence of temperature, tack coat type, and the type of paving geosynthetic on the *ISS* of asphalt overlays with paving geosynthetic. Two combinations were evaluated: one with a geogrid with a mesh size of 12.5 mm and a PG 64-22 binder as a tack coat (G12.5-PG), and another with a geogrid with a mesh size of 25 mm and asphalt emulsion SS-1 as a tack coat (G25-S1). These combinations were tested at 5°C, 18°C, 32°C, and 48°C. Figure 2.20 presents the results of this study, indicating better performance for the G12.5-PG interface compared to the G25-S1 interface. According to Safavizadeh et al. (2020), this improvement is attributed to the use of PG 64-22. However, temperature proved to be the most influential factor.

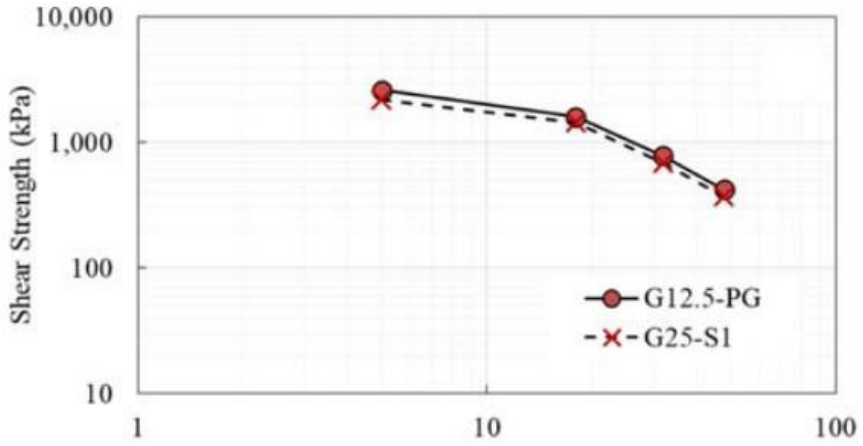

Figure 2.20 – Influence of tack coat type on *ISS* obtained from asphalt overlays with paving geosynthetic. Source: Safavizadeh et al. (2020).

2.4.3.2 Tack coat rate

The application of tack coat type is an essential step in rehabilitation of asphalt layers. The applied tack coat can fill voids on the asphalt surface and increase the contact area between the new and old asphalt layer, consequently leading to improved bonding. However, if the tack coat rate used is excessive, a sliding plan can be introduced at the interface, reducing bonding and interlocking between asphalt layers. Thus, the tack coat rate employed is crucial to ensure adequate bond.

In the literature, there is no consensus regarding the effect of tack coat rate on *ISS*. The findings of Sufian et al. (2021) suggested that variations in tack coat rate not influence the *ISS*. Hu et al. (2017a) investigated the influence of tack coat type and rate, as well as temperature on *ISS* testing laboratory-prepared specimens. Figure 2.21 shows the results obtained by Hu et al. (2017a). It was observed a decrease in *ISS* with increasing tack coat rate, particularly at higher temperatures, as depicted in Figure 2.21. This behavior was also noted by Mohammad et al. (2012) in laboratory-prepared specimens. On the other hand, Mohammad et al. (2012) noticed when testing specimens extracted from the field, an increase in tack coat rate led to an enhancement in *ISS.*

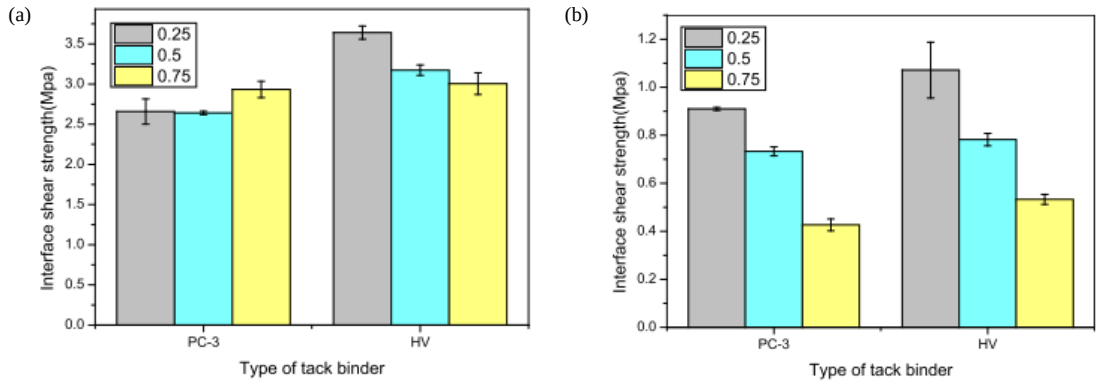

Figure 2.21 – Effect of the tack coat type and rate, and temperature on *ISS*: (a) 25°C, (b) 50°C. Source: Hu et al. (2017a).

In the study conducted by Mohammad et al. (2018), following an investigation involving core fields from various states in the United States, it was observed that the tack coat type exhibited statistical significance in relation to interface bonding. Mohammad et al. (2018) suggested that an increase in the tack coat rate leads to an enhancement in *ISS*. However, it is noteworthy that Mohammad et al. (2018) examined only two distinct tack coat rates.

In contrast, Yang et al. (2021) delved into a more comprehensive analysis, involving up to seven different tack coat rates, different tack coat types and temperatures in laboratory-prepared specimens. The findings indicated an initial trend of increased *ISS* with increasing tack coat rate, followed by a subsequent decrease after reaching a certain tack coat rate. This implies that an excess of tack coat may be detrimental to *ISS*. Furthermore, the results suggested that the optimal tack coat rate depend upon both temperature and tack coat type. Figure 2.22 illustrates one of the obtained results.

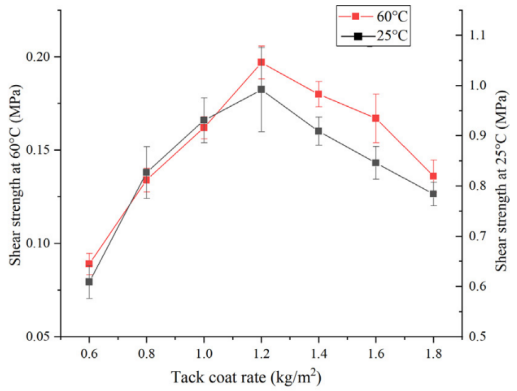

Figure 2.22 – Effect of the temperature and tack coat rate on *ISS*. Source: Yang et al. (2021).

In the case of asphalt overlays with paving geosynthetic, Noory et al. (2019a) investigated the influence of various factors on interface shear strength through a Taguchi experimental design. Among the factors analyzed, the tack coat rate proved to be the second most influential factor after temperature, with the *ISS* gain decreasing as the tack coat rate increased. Correia and Mugayar (2021) extracted specimens from experimental asphalt pavement section with paving geosynthetics and investigated the effect of different tack coat rates with various types of paving geosynthetics. The results of Leutner shear tests also indicated the benefit of increasing the tack coat rate for all paving geosynthetics evaluated. However, based on the results obtained by Correia et al. (2023), different *ISS* trends were observed in extracted specimens from the experimental asphalt pavement section with paving geosynthetics at Salvador Airport in Brazil. The results revealed the following trends: 1) an increase in *ISS* with an increasing tack coat rate; 2) an increase in *ISS* with an increase in the tack coat rate up to a certain point, followed by a decrease with a further increase in the tack coat rate; 3) a decrease in *ISS* with an increase in the tack coat rate up to a certain point, followed by an increase with a further increase in the tack coat rate. Figure 2.23 illustrates the *ISS* results obtained by Correia et al. (2023).

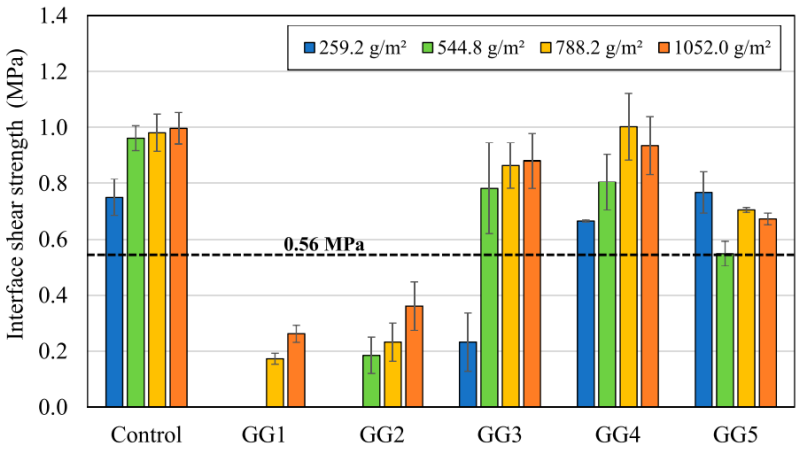

Figure 2.23 – Effect of the tack coat rate on *ISS* of asphalt overlays with different paving geosynthetic. Source: Correia et al. (2023).

2.4.3.3 Texture and interface conditions

In terms of texture and interface condition, research indicates that smooth or rough asphalt surfaces affect interface bonding (Li et al., 2013; White, 2017). Collop et al. (2009), and Sufian

et al. (2021) suggest that the particle size distribution of asphalt mixtures significantly influences the shear strength of the interface. Variations in aggregate particle size distribution can yield different types of asphalt mixtures, such as dense, open, and gap-graded, leading to diverse surface combinations and resulting in varying *ISS* values (Raposeiras et al., 2013; Zhang, 2017; Zhao et al., 2017).

The presence of rounded and water-sensitive grains adversely affects bond performance (Tran et al., 2012; White, 2015). Mohammad et al. (2018) revealed that the *ISS* is highly dependent on the type of existing pavement surface, whether asphalt or Portland cement concrete, and its texture. Mohammad et al. (2018) noted that milled hot mix asphalt (HMA) surfaces yield higher *ISS* results, followed by newly applied asphalt concrete, existing asphalt overlay surfaces, and finally, Portland cement concrete surfaces.

However, Noory et al. (2019a) investigated the contribution of various factors to the *ISS* of asphalt overlays with paving geosynthetic. Among the evaluated factors, texture was statistically significant only for interface shear bond tests with normal stress, but with the lowest level of contribution (0.62%) to the *ISS*. Canestrari et al. (2022) evaluated the influence of milled and non-milled surface in *ISS* of asphalt overlays with different paving geosynthetics. The results obtained by Canestrari et al. (2022) demonstrated that the presence of paving geosynthetic within asphalt overlays tends to mitigate difference between milled and non-milled asphalt surfaces in terms of *ISS*.

2.4.3.4 Influence of paving geosynthetic on the interface bonding: types, physical properties, and mechanical properties

Several studies have pointed out that the incorporation of paving geosynthetic within asphalt overlays reduces the interface shear bonding (Canestrari et al., 2018, 2021; Correia e Mugayar, 2021; Kumar e Saride, 2017; Sagnol et al., 2019a; Saride e Kumar, 2017; Solatiyan et al., 2021b; Spadoni et al., 2021; Sudarsanan et al., 2018a; Walubita et al., 2018). However, in some studies, different paving geosynthetics, combined with other factors such as tack coat type and rate, achieved values of *ISS* close to those obtained from asphalt overlays without paving geosynthetic (Correia e Mugayar, 2021; Sagnol et al., 2019a; Solatiyan et al., 2021a; Sudarsanan et al., 2018a; Walubita et al., 2018).

Various types of paving geosynthetics influence the *ISS* and *k*, as well as being subjected to different bonding mechanisms with the surrounding asphalt layers. These mechanisms are Through Hole Bonding (THB) and adhesion. THB occurs when there is mobilization of shear strength through interlocking between the aggregate in the asphalt mixture and the geogrid. The second mechanism is driven by the adhesion between the geotextile and the asphalt layers (Sudarsanan et al., 2018). Figure 2.24 illustrates these mechanisms according to the type of paving geosynthetic.

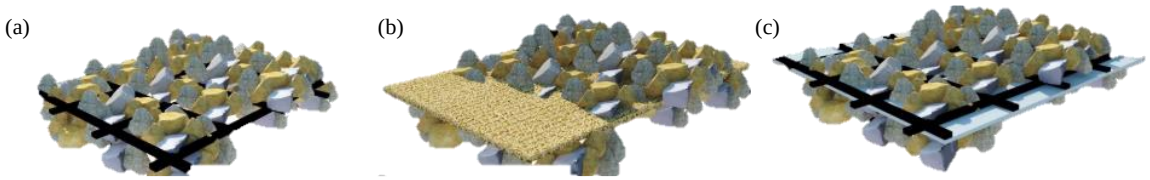

Figure 2.24 – Bonding mechanism (upper asphalt surface/lower asphalt surface): (a) geogrid (THB/THB), (b) geotextile (adhesion/adhesion), and (c) geocomposite (THB/adhesion). Source: Sudarsanan et al. (2018).

In the study conducted by Kumar and Saride (2017), the interface shear bonding properties of asphalt overlays with paving geosynthetic were evaluated using a large-scale direct shear device. The polyester (PET) geogrid with bituminous coating exhibited the best performance, followed by the polypropylene (PP) geogrid, fiberglass geocomposite, and jute fiber geotextile. Kumar and Saride (2017) have pointed out that the geogrids outperformed the other two paving geosynthetics due to the THB mechanism facilitated by the geogrid mesh. Furthermore, among the geogrids, the bituminous coating of the PET geogrid may have positively influenced the results, as it had a smaller geogrid mesh than the PP geogrid.

In Noory et al.'s study (2019a) the *ISS* was evaluated using four geocomposites, consisting of fiberglass geogrid combined with non-woven PP geotextile, each with different geogrid mesh of 28 mm, 33 mm, 67 mm, and 111 mm. These mesh sizes were chosen despite resulting in different ultimate tensile strengths. The findings indicated that *ISS* increased with larger geogrid mesh, a trend also observed by Walubita et al. (2018). However, Correia and Mugayar (2021) supplemented this by suggesting that geogrid mesh plays a crucial role, but only up to a certain size. Correia and Mugayar (2021) suggested an optimal *ISS* behavior based on the combination of aggregate, geogrid mesh size, and tack coat rate.

Sagnol et al. (2019a) investigated, through Leutner shear tests, the influence of incorporating or not lightweight fabric backing in geogrids and the type of coating on paving geosynthetics. According to Sagnol et al. (2019a), the presence of a fabric backing negatively influenced interface bonding. Regarding geosynthetic coating, it was reported that the type of coating influences *ISS*, which aligns with the findings of Kumar e Saride (2017).

Another parameter that can influence the bonding properties is the tensile stiffness of geosynthetic. Sudarsanan et al. (2018a) evaluated the *ISS* of asphalt overlays with paving geosynthetic. In their study, three geosynthetics were employed: coconut fiber geotextile, jute fiber geotextile, and a fiberglass geocomposite. Sudarsanan et al. (2018a) reported that higher tensile stiffness in geosynthetics resulted in a smaller reduction in *ISS*. However, the statement that a higher stiffness modulus of geosynthetics will increase the bonding between asphalt layers may not be appropriate. Walubita et al. (2018) found opposing results, as PET geogrids exhibited superior performance to fiberglass geogrids in reinforced interfaces, attributed to the flexibility of the material. Correia e Mugayar (2021) also investigated the influence of geosynthetic tensile stiffness and observed that an increase in stiffness did not lead to superior interface bonding. They suggest that physical properties of geosynthetics may be more influential than the mechanical properties of geosynthetics in the bonding of asphalt overlays with paving geosynthetic.

As noted in the literature, many factors may be correlated with the bonding performance of asphalt overlays with paving geosynthetic. Furthermore, new paving geosynthetics have been manufactured to mitigate reflective cracking, such as hybrid geosynthetics, also known as paving mats, as outlined in ASTM D7239 (2018) "Standard Specification for Hybrid Geosynthetic Paving Mat for Highway Applications", thereby encouraging further investigations. Another crucial aspect is how the paving geosynthetics behaves when subjected to cyclic shear loads.

2.5 Interface shear fatigue: testing devices, procedures, parameters, and rupture criteria

As traffic loads applied to pavements are cyclic, several studies have been investigating the behavior of the interface through cyclic shear tests to understand long-term performance of the pavement structure (Canestrari et al., 2022; D'Andrea e Tozzo, 2016; Diakhate et al., 2006; Diakhaté et al., 2011; Donovan et al., 2000; Isailović et al., 2017; Isailović and Wistuba, 2018; Miró et al., 2021; Nian et al., 2020; Petit et al., 2012; Ragni et al., 2021, 2019; Romanoschi e

Metcalf, 2001; Safavizadeh e Kim, 2014; Safavizadeh et al., 2020; Song et al., 2016; Tozzo et al., 2016, 2015, 2014a, 2014b; Wang et al., 2017; Yang et al., 2020). Thus, similar to monotonic shear bond tests, various testing devices has been developed.

One of the first studies addressing this subject was conducted by Donovan et al. (2000). Donovan et al. (2000) developed equipment with the aim of applying a cyclic shear load at the interface of a specimen simulating the layer of a concrete bridge deck overlaid by a asphalt layer. The tests were conducted with a controlled displacement of 0.40 mm, using a displacement pulse in the haversine format and a frequency of 1 Hz. Figure 2.25 illustrates the testing device used in Donavan et al. (2000).

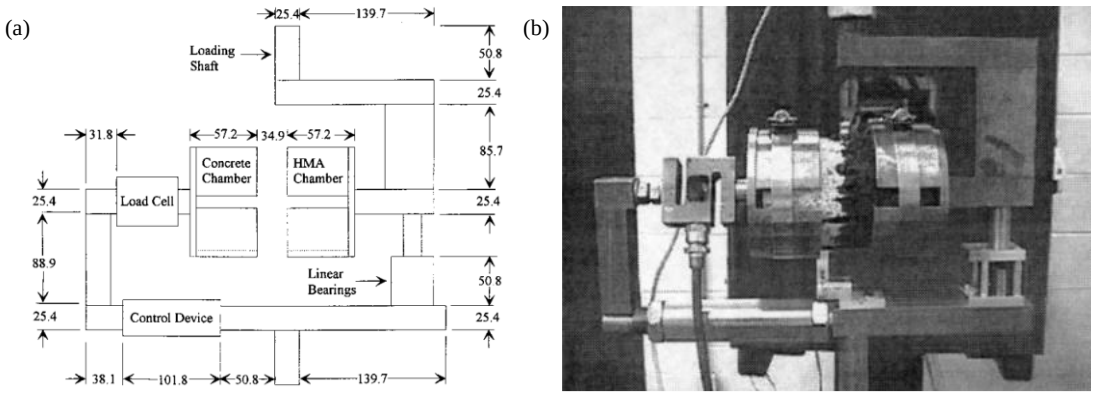

Figure 2.25 – Testing device used in Donavan et al. (2000): (a) device schematic, (b) device photograph.

Romanoschi and Metcalf (2001) developed a 25.5° inclined shear fatigue test. In this study, asphalt specimens are placed in two metallic molds separated by a 5 mm gap. To allow horizontal relative movement of the upper part of the assembly and the actuator, a steel sphere plate was positioned on top of the upper base plate. The actuator cyclically acts on a steel plate placed above the sphere plate. In conjunction with vertical force and displacement, shear and normal displacements at the interface are measured by two linear variable differential transformers (LVDTs). Elastic and permanent displacements in both tangential and normal directions, as well as maximum and minimum vertical forces, were recorded at each cycle. The tests were conducted under stress control with a haversine pulse and a test frequency of 5 Hz. Figure 2.26 illustrates the schematic of shear fatigue device developed by Romanoschi and Metcalf (2001).

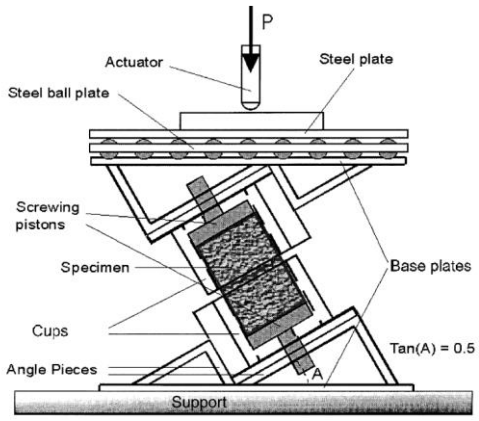

Figure 2.26 – Shear fatigue device schematic. Source: Romanoschi and Metcalf (2001)

D'Andrea e Tozzo (2016) adapted the Sapienza Inclined Shear Test Machine, developed and designed at Sapienza University of Rome to assess shear fatigue performance, similar to the apparatus used by Wheat (2007) and Romanoshi and Metcalf (2001). The device features two half-molds with an internal diameter of 100 mm, with the sample axis inclined relative to the horizontal, capable of being executed at angles ranging from 0 to 65°, allowing for the adjustment of the ratio between normal and shear force components. The gap between the half-molds is fixed at 1 cm, and to facilitate sliding between the components, the device incorporates a plate with spherical materials. The tests were conducted under controlled stress, with a stress pulse in a haversine waveform and at three frequencies (1, 2, and 5 Hz). Figure 2.27 shows the Sapienza Inclined Shear Test Machine.

Figure 2.27 – Sapienza Inclined Shear Test Machine. Source: D'Andrea and Tozzo (2016).

Tozzo et al. (2014b) used the Sapienza Direct Shear Testing Machine to investigate the performance of shear fatigue. The testing device is similar to that used by Donovan et al. (2000), with the difference lying in the capability to apply normal stress. The device features a fixed 1 cm

gap between the molds and is capable of testing double-layer cylindrical specimens with a diameter of 100 mm. The test was conducted under constant normal stress, a haversine shear load pulse, and frequencies of 1 Hz and 5 Hz. Figure 2.28 shows the scheme of Sapienza Direct Shear Testing Machine.

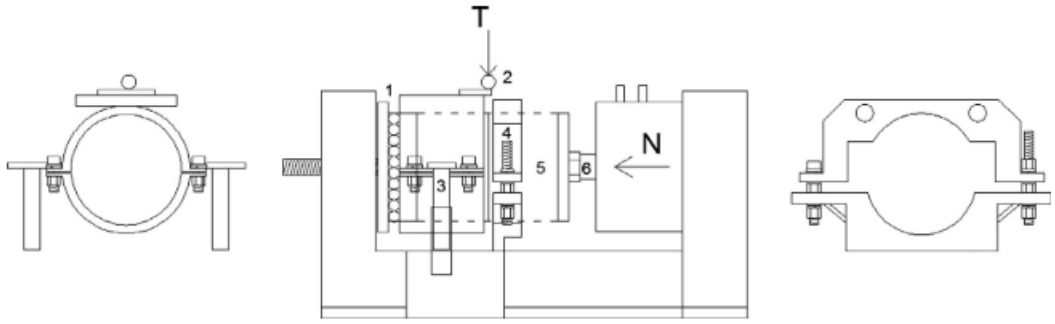

Figure 2.28 – Scheme of Sapienza Direct Shear Testing Machine. Source: Tozzo et al. (2014b)

At the University of Limoges in France, the "3MsCe" Laboratory has implemented a double shear testing device. In this testing device, the specimens are prismatic with two symmetrical interfaces. These interfaces are simultaneously subjected to the application of a shearing loads, acting by moving the central part, while the external parts remain fixed. The tests were conducted under controlled stress conditions, with a sinusoidal waveform and a frequency of 10 Hz. (Diakhaté et al., 2011). Figure 2.29 depicts double shear test.

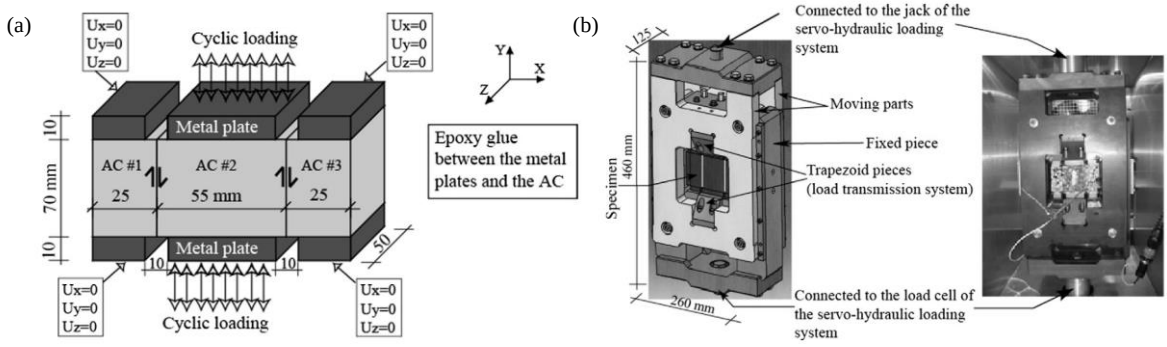

Figure 2.29 – Double shear test: a) schematic diagram of the double shear test, b) schematic and photographic presentation of the double shear device. Source: Diakhaté et al. (2011).

Recently, the Task Group 3 "Multilayer Pavement System" of RILEM TC 272-PIM presented the direct shear devices that have been used in different laboratories involved in the

investigation of cyclic shear tests (Canestrari et al., 2022a). Among the devices are a) Cyclic-Ancona Shear Testing Research and Analysis (C-ASTRA); b) Advanced Shear Tester (AST); c) Modified Advanced Shear Tester (MAST); d) Cyclic Compressed Shear Bond (CCSB); and e) Repeated Impulse Leutner (RIL). Figure 2.30 illustrates these devices.

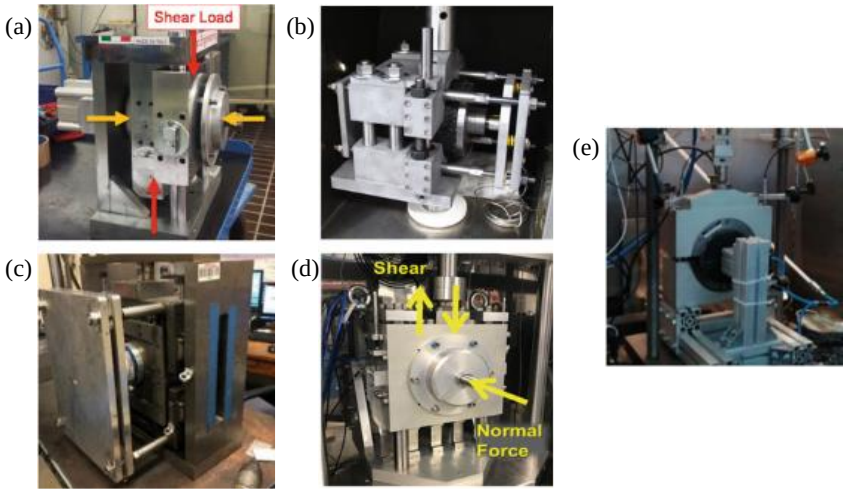

Figure 2.30 – Testing devices used by the participating laboratories of Task Group 3 of RILEM TC 272-PIM: (a) C-ASTRA, (b) AST, (c) MAST, (d) CCSB, and (e) RIL. Source: Canestrari et al. (2022).

The Cyclic-Ancona Shear Testing Research and Analysis (C-ASTRA) device (Figure 2.30a) was employed at the Polytechnic University of Marche. It consists of two half-boxes separated by an adjustable gap. One half-box moves vertically, allowing for the application of a vertical load (parallel to the interface). The other half-box can slide horizontally (perpendicular to the interface), enabling the phenomenon of dilatancy. The device also facilitates the application of a pre-set normal load (perpendicular to the interface) using a pneumatic actuator (Ragni et al., 2019). The C-ASTRA tests were conducted under tension-controlled conditions in a haversine waveform, with a frequency of 5 Hz and without the application of normal stress.

The Advanced Shear Tester (AST) device (Figure 2.30b) was employed at both Gdansk University of Technology and the Road and Bridge Research Institute. It primarily consists of two parts: a stationary support and a movable collar, with an adjustable variable gap size between them (Zofka et al., 2015). The AST device can apply normal stress to the interface through four die springs. Gdansk University of Technology conducted cyclic AST tests with a 2 mm gap, stress control, and a frequency of 5 Hz. Meanwhile, Road and Bridge Research Institute conducted Cyclic AST tests with a 5 mm gap, a frequency of 10 Hz, and a normal stress of 400 kPa.

The Modified Advanced Shear Tester (MAST) device (Figure 2.30c) was employed at the North Carolina State University. It comprises a fixed side plate and a movable side plate separated by an 8 mm gap. The movable side plate is free to move both vertically (parallel to the interface) and horizontally (perpendicular to the interface). The MAST device also allows the application of normal stress to the specimen through a bolt and spring system (Cho et al., 2017). This testing device was used in a controlled displacement test, with a frequency of 5 Hz and without normal stress.

The Cyclic Compressed Shear Bond (CCSB) device was utilized by the Swiss Federal Laboratories for Materials Testing and Research in collaboration with the University of Dresden. Double-layer cylindrical specimens are bonded to half-shells mounted on aluminum supports (Figure 2.30d). The shear stress is applied by a vertical mobile support, while the horizontally mobile support enables the application of normal stress. The test was conducted with controlled sinusoidal displacement and five frequencies (0.1, 0.3, 1, 3, and 10 Hz).(Canestrari et al., 2022a).

The Repeated Impulse Leutner (RIL) device was developed at the University of Bologna and allows the assessment of fatigue life under cyclic shear and normal loadings. The device comprises a traditional Leutner apparatus affixed to a structure equipped with a pneumatic piston capable of applying a constant normal stress on the upper surface of the double-layered cylindrical specimen, as depicted in Figure 2.30e (Canestrari et al., 2022a). At the University of Bologna, it was employed under stress-controlled conditions in a haversine waveform, with a frequency of 0.7 Hz and without normal stress.

Regarding the testing procedure, as there is no standard establishing a procedure, different test conditions are found in the literature. Most studies have conducted the test under controlled stress conditions (D'Andrea e Tozzo, 2016; Miró et al., 2021; Nian et al., 2020; Ragni et al., 2019; Romanoschi e Metcalf, 2001; Safavizadeh et al., 2020; Song et al., 2016; Wang et al., 2017; Yang et al., 2020; Zofka et al., 2015). However, there are studies have performed the test using controlled displacement (Donovan et al., 2000; Isailović et al., 2017; Isailović and Wistuba, 2018; Ragni et al., 2022).

The controlled stress method maintains peak and rest stresses constant during the loading process. Meanwhile, in the controlled displacement mode, the displacement amplitude is kept constant during the test. In both the controlled stress and controlled displacement methods, there is no consensus on the value of stress or displacement amplitude to be applied. In the first method,

constant stress is maintained as relative displacement gradually increases, while in the second method, stress decreases progressively to maintain the same displacement level (Liao et al., 2012).

In the literature, the frequencies commonly employed in shear fatigue tests are 1, 2, 5, 10, and 15 Hz, with particular emphasis on the values of 1, 5, and 10 Hz. Regarding the pulse load waveform, tests have been conducted either in the haversine waveform (D'Andrea e Tozzo, 2016; Miró et al., 2021; Nian et al., 2020; Ragni et al., 2019; Romanoschi e Metcalf, 2001; Tozzo et al., 2015, 2014a, 2014b, 2016) or in the sinusoidal waveform (Isailović e Wistuba, 2018; Ragni et al., 2021; Safavizadeh et al., 2020; Song et al., 2016; Yang et al., 2020; Zofka et al., 2015). Figure 2.31 shows the type of pulses. The distinction between these waveforms is illustrated in Figure 2.31a. Furthermore, tests may be conducted with (Figure 2.31b) or without (Figure 2.31a) rest periods.

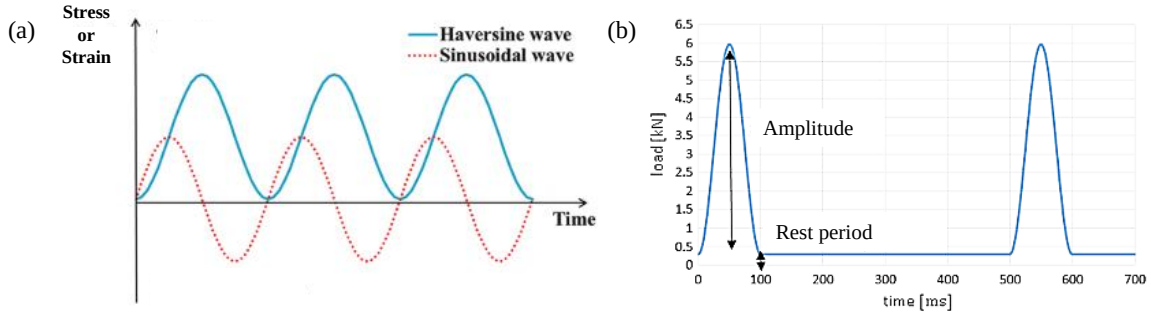

Figure 2.31 – Types of pulses: a) Haversine and sinusoidal waveform without a rest period (Cheng et al., 2021); b) Haversine pulse with a rest period (Tozzo et al., 2016).

Among the studies that employ the rest period, most indicate a loading pulse of 0.1s with the rest period varying from 0.9s, 0.4s, 0.1s for frequencies of 1, 2, and 5 Hz, respectively (Canestrari et al., 2022a; Donovan et al., 2000; Tozzo et al., 2016, 2015, 2014b, 2014a). After a finite element analysis, Tozzo et al. (2014a, 2014b) pointed out that the test frequency and rest time depend on the magnitude of the applied shear stress, justifying that for higher levels of applied stress, the rest time should be longer for complete viscoelastic recovery. However, other authors maintained the constant loading amplitude, regardless of the frequency employed (Miró et al., 2021; Nian et al., 2020). Regarding research that did not use rest time, the loading pulse time depended on the test frequency, determined by the well-known relationship between period and frequency (Miró et al., 2021; Ragni et al., 2022, 2019; Safavizadeh et al., 2022a; Song et al., 2016; Yang et al., 2020).

The shear fatigue test provides several parameters as a function of the number of cycles, such as permanent shear displacement, cyclic interface shear stiffness modulus ($k_{s,n}$), and the total accumulated dissipated energy (E_D) (Canestrari et al., 2022a). Figure 2.32 presents the permanent displacement vs. number of cycles curve. According to Tozzo et al. (2014b), this curve can be divided into three stages. In the first stage, adjustments of interlocking between aggregates at the interface lead to a rapid increase in interface displacement. After this brief initiation, sliding continues to grow slowly in the second stage, with an approximately constant trend easily identified by the slope of the tangent line to the response curve. The intermediate stage concludes when the curve shows an inflection point. The last stage is characterized by a very rapid propagation of the failure mechanism and, consequently, a very rapid increase in displacement. This interpretation is also provided in other dynamic tests conducted on asphalt mixtures, for example, the dynamic creep test, as shown in Figure 2.32b (Alavi et al., 2011).

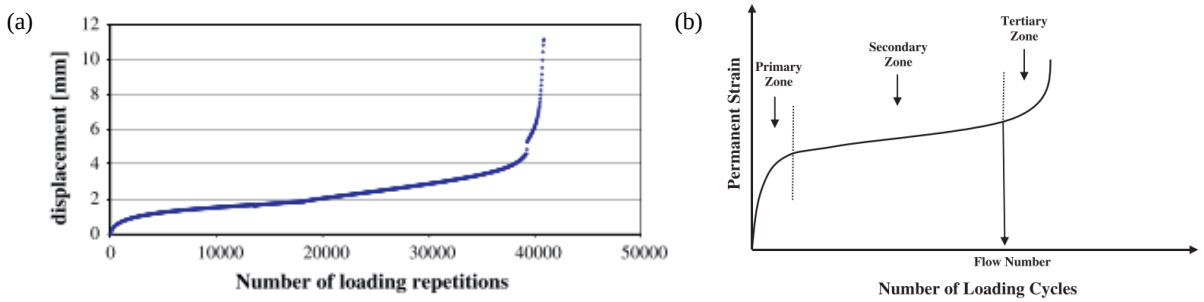

Figure 2.32 – Typical results from dynamic tests: a) permanent displacement vs. number of cycles obtained from shear fatigue test (Tozzo et al., 2014b); b) permanent displacement curve vs. number of cycles obtained from dynamic creep test (Alavi et al., 2011)

According to Diakhaté et al. (2011), for each fatigue test, the cyclic interface shear stiffness can be expressed by $k^*_{s,n}$, as presented in Equation 2.14. From this number, the cyclic interface shear stiffness modulus ($k_{s,n}$) can be determined, as per Equation 2.15. Other studies have adopted Equation 2.15 to determine cyclic interface shear stiffness modulus (Isailović et al., 2017; Isailović e Wistuba, 2018; Ragni et al., 2021, 2019).

$$k^*_{s,n}(i\omega) = \frac{\Delta F_n}{S \cdot \Delta u_n} \cdot e^{i\varphi_n} \tag{2.14}$$

$$k_{s,n} = \left| k^*_{s,n}(i\omega) \right| = \frac{\Delta F_n}{S \cdot \Delta u_n} = \frac{\Delta \tau_n}{\Delta u_n} \tag{2.15}$$

Where $k^*_{s,n}$ is the complex number expressing the cyclic interface shear stiffness at the n^{th} cycle, ΔF_n is the amplitude of the applied shear force at the n^{th} cycle; Δu_n is the amplitude of the relative shear displacement measured at the n^{th} cycle; φ_n is the phase angle between the shear force and displacement signals at the n^{th} cycle; S is the interface cross-section area; $k_{s,n}$ is the cyclic interface shear stiffness modulus at the n^{th} cycle, and $\Delta\tau$ is the amplitude of the shear stress at the n^{th} cycle.

The phase angle is conceptualized as the time interval or delay between the peak of the stress pulse and the peak of the relative strain pulse (Cheng et al., 2021). Typically, φ_n is obtained for a two-node sinusoidal waveform, with limits ranging from 0° to 360° (Figure 2.34a)(Sun et al., 2018; Venudharan e Biligiri, 2015; Ye et al., 2009). Mathematically expressed by Equation 2.16. However, according to Venudharan and Biligiri (2015), for haversine waveform pulses, the total wavelength ranges between 0 and 180°. In such cases, the phase angle should be expressed by Equation 2.17. Figure 2.33 shows phase angle for different types of waveform pulse.

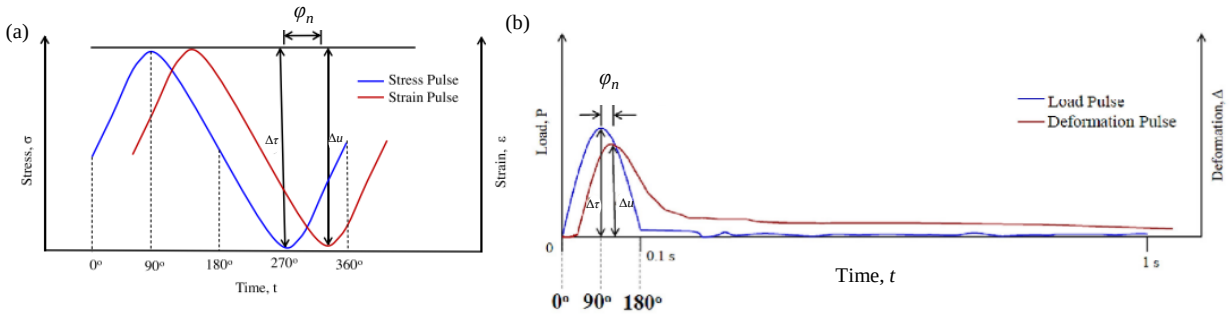

Figure 2.33 – Phase angle for different types of waveform pulse: (a) sinusoidal waveform, (b) haversine waveform. Source: Venudharan and Biligiri (2015).

$$\varphi_n = 360° \cdot f \cdot t \tag{2.16}$$

$$\varphi_n = 180° \cdot f \cdot t \tag{2.17}$$

Where φ_n is the phase angle at the n^{th} cycle, f is the test frequency, and t is the time interval between the peak of the stress pulse and the peak of the relative strain pulse at the n^{th} cycle.

There are few studies on shear fatigue that have analyzed energy dissipation. According to Petit et. al. (2012), , this parameter is calculated for each loading cycle using Equation 2.18. The accumulated energy dissipation is given by Equation 2.19.

$$E_{D,n} = \pi \cdot \Delta\tau_n \cdot \Delta u_n \cdot \sin\varphi_n \tag{2.18}$$

$$E_{CD} = \sum_{i=1}^{n} E_{D,n} \tag{2.19}$$

Where $E_{D,n}$ is the energy dissipation [kJ/mm²] at the n^{th} cycle; $\Delta\tau_n$ is the amplitude of shear stress [kPa] at the n^{th} cycle, Δu_n is the amplitude of relative displacement measured (mm) at the n^{th} cycle, φ_n is the phase angle at the n^{th} cycle; e E_{CD} is the accumulated energy dissipation [kJ/mm²].

In the literature, two criteria have been adopted regarding failure criteria for fatigue shear studies. Some research studies have recommended using the number of cycles corresponding to complete debonding of the interface as a failure criterion (D'Andrea e Tozzo, 2016; Tozzo et al., 2015, 2014b), while others studies have employed the number of cycles relative to 50% reduction in the initial interface shear stiffness modulus (N_{50}) (Diakhaté et al., 2011; Isailović et al., 2017; Isailović and Wistuba, 2018; Petit et al., 2012; Ragni et al., 2021; Song et al., 2016; Tozzo et al., 2014b). The approach to determine N_{50} is typically obtained from the curve of the interface shear stiffness modulus, or the modulus normalized by the initial value, both plotted against the number of cycles. Figure 2.34 shows approaches for N_{50}.

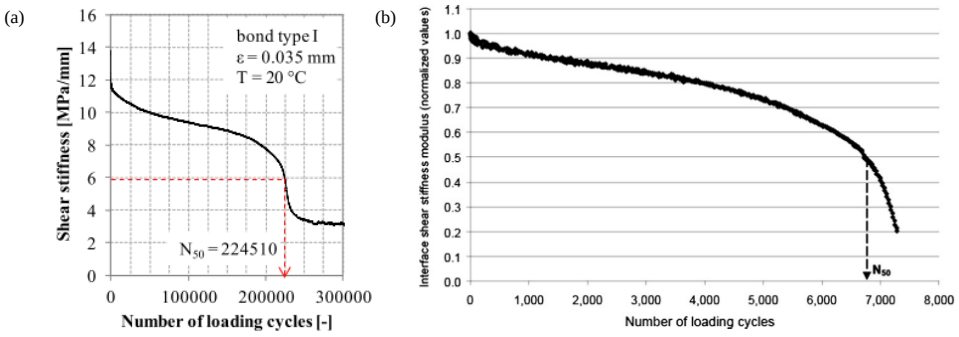

Figure 2.34 – Approaches for N_{50}: (a) interface shear stiffness modulus vs. number of cycles (Isailović and Wistuba, 2018), (b) normalized interface shear stiffness modulus vs. number of cycles (Diakhaté et al., 2011).

The N_{50} criterion has been used for both controlled displacement and tension-controlled tests. However, the adoption of this criterion for tension-controlled testing is controversial when using other fatigue tests for asphalt mixtures. Some studies have recommended its use only for controlled displacement tests because, in this case, the testing time can be very long, and the failure condition is not obvious, unlike stress-controlled tests, in which the specimen ruptures completely (Bhasin et al., 2009; Liao et al., 2012; Masad et al., 2008). In this case, the criterion of complete debonding seems more suitable for stress-controlled tests. In addition, Bhasin et al. (2009) recommended the number of cycles corresponding to a 100% increase in strain compared to its initial value.

The ASTM D8237 (2021) 'Standard Test Method for Determining Fatigue Failure of Asphalt-Aggregate Mixtures with the Four-Point Beam Fatigue Device' recommends, as a failure criterion, the number of cycles corresponding to the peak value of the curve of normalized stiffness times normalized cycles versus the number of cycles. However, this failure criterion has not yet been employed in a shear fatigue test. The normalized stiffness times normalized cycles is given by Equation 2.20. Figure 2.35 shows normalized stiffness times normalized cycles failure criterion's approach.

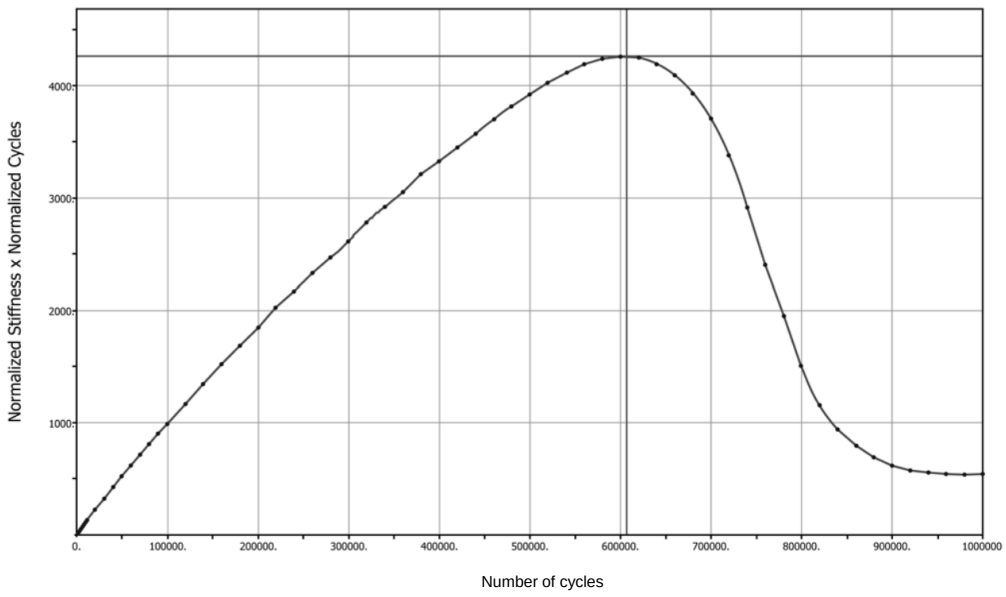

Figure 2.35 – Normalized stiffness times normalized cycles failure criterion's approach. Source: ASTM D8237 (2021).

$$SN = \frac{S_i \times N_i}{S_0 \times N_0} \tag{2.20}$$

Where *SN* is the normalized stiffness times normalized cycles, S_i is stiffness at cycle i, N_i is the cycle i, S_0 is initial stiffness, estimated at approximately 50 cycles, and N_0 is the number of cycles corresponding to the initial stiffness.

2.5.1 Studies regarding shear fatigue test: influencing factors and correlation with monotonic interface shear test

In fatigue shear tests, as in monotonic interface shear tests, there are several factors influencing the fatigue properties. These factors are related to either the test configurations or the interface characteristics. Regarding the test configurations, the factors studied so far include frequency, temperature, stress/strain pulse amplitude, the ratio between the force applied in cyclic testing and *ISS* (Δτ/ISS), and the application of normal stress. Concerning interface characteristics, investigations have been conducted with or without the presence of tack coat, variation in the tack coat rate, and tack coat type (Miró et al., 2021; Nian et al., 2020; Ragni et al., 2021, 2019; Song et al., 2016; Tozzo et al., 2014b; Wang et al., 2017; Yang et al., 2020).

Regarding the studies that evaluated different test frequency, Nian et al. (2020) observed that an increase in frequency results in enhanced shear fatigue life performance. This phenomenon was also noted by Miró et al. (2021). Although additional studies have explored test frequency variations, the simultaneous variation in applied stress magnitude precluded an assessment of its impact on the corresponding cycles to failure (D'Andrea e Tozzo, 2016; Tozzo et al., 2014a, 2014b). Figure 2.36 shows the relationship between shear fatigue life and loading frequency.

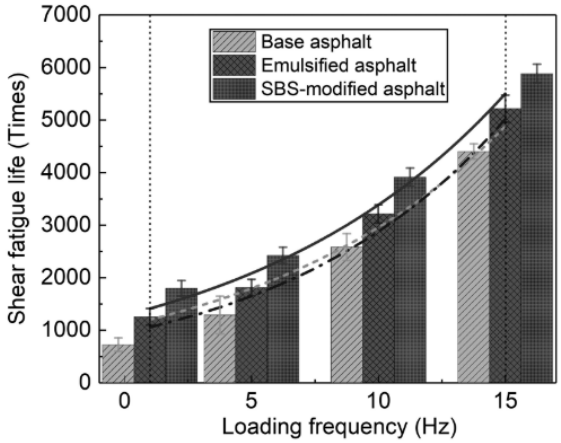

Figure 2.36 – Relationship between shear fatigue life and loading frequency. Source: Nian et al. (2020).

Concerning the temperature, as observed in monotonic interface shear bond tests, studies have demonstrated that an increase in temperature reduces the shear fatigue life (Nian et al., 2020; Wang et al., 2017). Figure 2.37 shows the fatigue life's trend of different tack coat types under different temperatures. Regarding the magnitude of the applied shear stress amplitude, studies have been conducted in two distinct ways: fixed stress values (D'Andrea and Tozzo, 2016; Miró et al., 2021; Romanoschi and Metcalf, 2001; Safavizadeh et al., 2022b; Tozzo et al., 2016, 2015, 2014b), and fixed $\Delta\tau/ISS$ ratio (Nian et al., 2020; Ragni et al., 2019; Song et al., 2016; Wang et al., 2017; Yang et al., 2020). In these cases, literature values for $\Delta\tau$/ISS range from 0.2 to 0.7. Regardless of the approach, results have shown that an increase in stress amplitude reduces the fatigue life. Figure 2.38 depicts the shear fatigue life behavior with tests conducted at fixed stress values and fixed $\Delta\tau/ISS$ ratio.

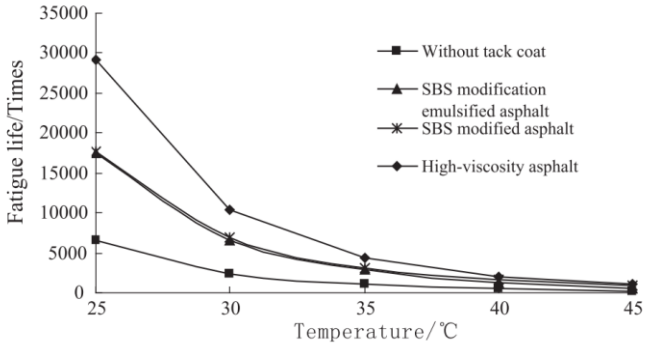

Figure 2.37 – Fatigue life's trend of different tack coat types under different temperatures. Source: Wang et al. (2017).

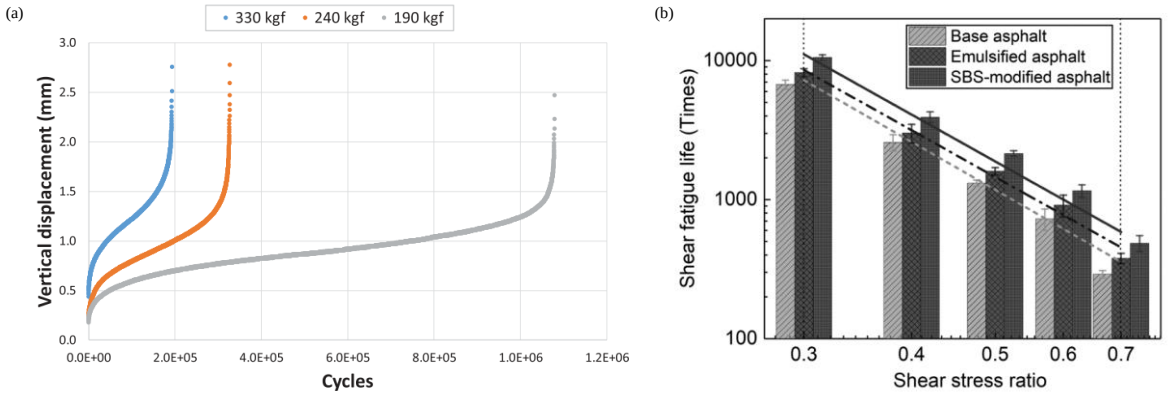

Figure 2.38 – Shear fatigue behavior under different stress pulse amplitude: (a) fixed stress values, (b) fixed Δτ/ISS ratio. Source: (a) Miró et al. (2021), (b) Nian et al. (2020).

In tests conducted under normal stress, similarly to what occurs in monotonic tests, the literature indicates an increase in the number of cycles to failure compared to tests performed without normal stress (D'Andrea e Tozzo, 2016; Tozzo et al., 2014b). Figure 2.39 illustrates this behavior.

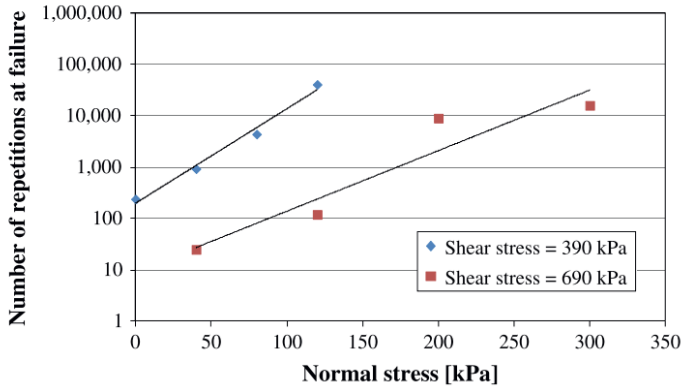

Figure 2.39 – Shear fatigue life at different normal stress. Source: Tozzo et al. (2014b).

Regarding the interface characteristics, studies have indicated that the presence and type of tack coat significantly influence shear fatigue life. The majority of studies show that the presence of tack coat provides long-term performance benefits for the interface. Figure 2.40 illustrates the findings reported by Yang et al. (2020) regarding the influence of tack coat presence and type, aligning with similar conclusions drawn in other studies (Nian et al., 2020; Ragni et al., 2022, 2019; Wang et al., 2017).

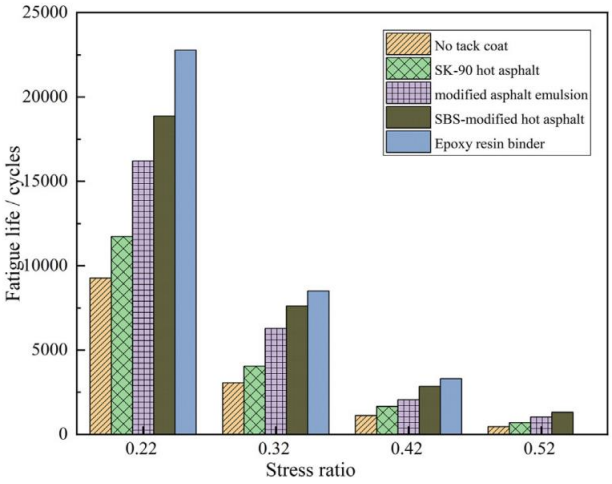

Figure 2.40 – The variation of shear fatigue life with different tack coat type. Source: Yang et al. (2020)

Few studies have evaluated the influence of different tack cot rates on shear fatigue life. Song et al. (2016) pointed out that the increase in the tack coat rate resulted in a decrease in fatigue life. Additionally, interfaces without tack coat yielded higher shear fatigue life results than interfaces with the presence of tack coat.

Few studies have investigated the shear fatigue behavior in asphalt overlays with paving geosynthetic. Donovan et al. (2000) assessed the influence of applying a geocomposite between a layer of cement concrete and an asphalt layer, as well as the variation of tack coat rate through shear fatigue testing. The tack coat rates used by Donovan et al. (2000) ranged from 1 to 2.5 kg/m². Figure 2.41 shows the results obtained by Donovan et al. (2000). It was identified an optimal tack coat rate that maximized the number of cycles to failure. Similar to monotonic interface shear tests, the presence of the geocomposite reduced the service life of the interface when compared to the interface without a geocomposite.

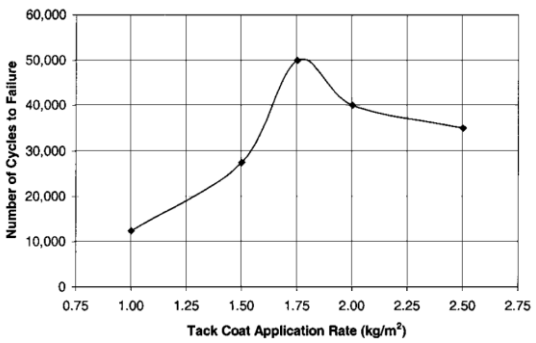

Figure 2.41 – Number of cycles to failure versus tack coat rate. Source: Donovan et al. (2000).

Safavizadeh et al. (2022) conducted a shear fatigue test with asphalt overlays with paving geosynthetic to assess the effect of geogrid mesh and tack coat type on both monotonic shear and shear fatigue tests. Two types of geogrids were employed, differing only in the mesh size (G12.5 mm and G25 mm), along with two tack coat types, PG 64-22, and emulsion (S1). In the cyclic MAST dynamic test, utilizing a sinusoidal load pulse at a frequency of 5 Hz, the fatigue life performance obtained by Safavizadeh et al. (2022) was as follows: G25-PG > G25-S1 > G12.5-S1. While, in the monotonic interface shear test, the performance rank differently: G25-PG > G12.5-PG > G25-S1. Safavizadeh et al. (2022) reported that for shear fatigue tests, the larger geogrid mesh seems to have a greater effect than the tack coat type, whereas in monotonic tests, the tack coat type appears to be more influential. However, the sample size in the study was small (one or two test replicates), suggesting the need for further investigations to confirm whether this is indeed a trend.

As observed so far, both monotonic and cyclic interface shear tests are capable of investigating and characterizing interface bonding. Shear strength is the criterion monotonic interface shear test, while for cyclic interface shear tests, the criterion is the number of cycles to failure. These two parameters are distinct; however, they are influenced by test condition, including the tack coat rate, loading rate, asphalt mixture type, temperature, and other factors.

Studies have been conducted to establish correlation between monotonic and cyclic interface shear tests. Isailović and Wistuba (2018) ranked the results of 10 asphalt interface combinations without paving geosynthetic according to their performance in monotonic shear and shear fatigue tests. Isailović and Wistuba (2018) observed that some combinations were ranked differently depend on the test type and suggested that shear strength derived from monotonic testing can only be used as an approximate indicator of long-term interface bonding performance. Figure 2.42 illustrates the observations made by Isailović and Wistuba (2018).

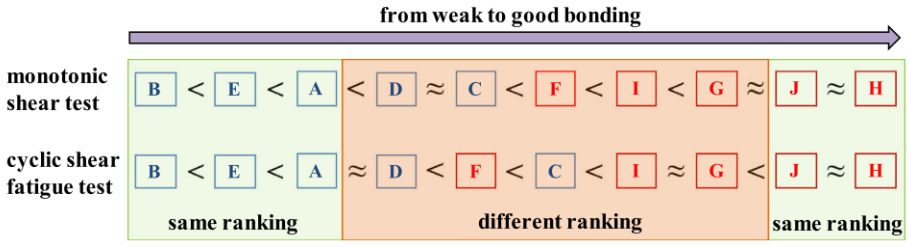

Figure 2.42 – Bond type ranking in monotonic shear test (based on resulting shear strengths) and in cyclic shear test (based on shear fatigue life). Source: Isailović and Wistuba (2018).

Yang et al. (2020) conducted a regression analysis between the parameters obtained in the monotonic shear test (*ISS* e *k*) and the shear fatigue life (N_f), indicating a strong correlation between these parameters. Figure 2.43 illustrates the variation of shear fatigue life with the *k* determined through monotonic interface shear testing.

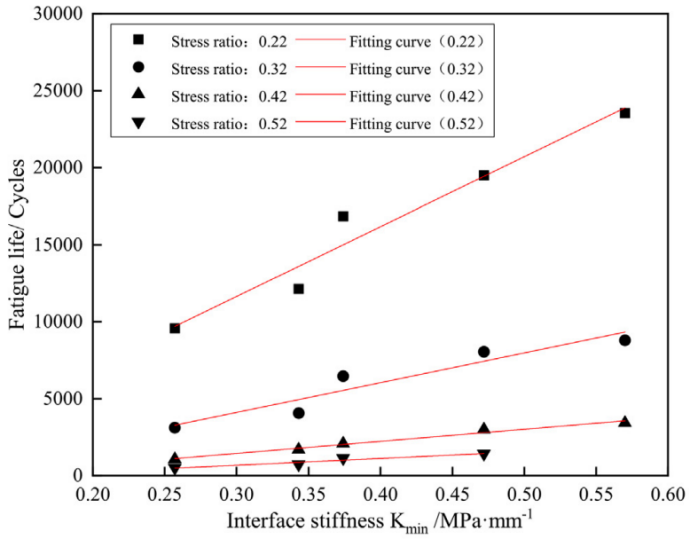

Figure 2.43 – Correlation between fatigue life and interface shear stiffness modulus. Source: Yang et al. (2020).

The investigation of the behavior of asphalt overlays through shear fatigue testing has advanced regarding the influence of test frequency, load amplitude, temperature, tack coat rate and type, as well as temperature. However, there is still a lack of studies addressing the influence of these factors on asphalt overlays with paving geosynthetic.

CHAPTER 3. MATERIALS

3.1 Asphalt mixture

The materials that compose the asphalt mixture used in this study are: a) crushed stone classified as size number 67 (ASTM D448, 2012), b) crushed stone classified as size number 8 (ASTM D448, 2012); c) stone dust classified as size number 89 (ASTM D448, 2012), d) stone dust classified as size number 10 (ASTM D448, 2012); e) calcitic hydrated lime (ASTM C1097, 2019), f) Performance grade (PG) 82-16 binder. Figure 3.1 presents these materials.

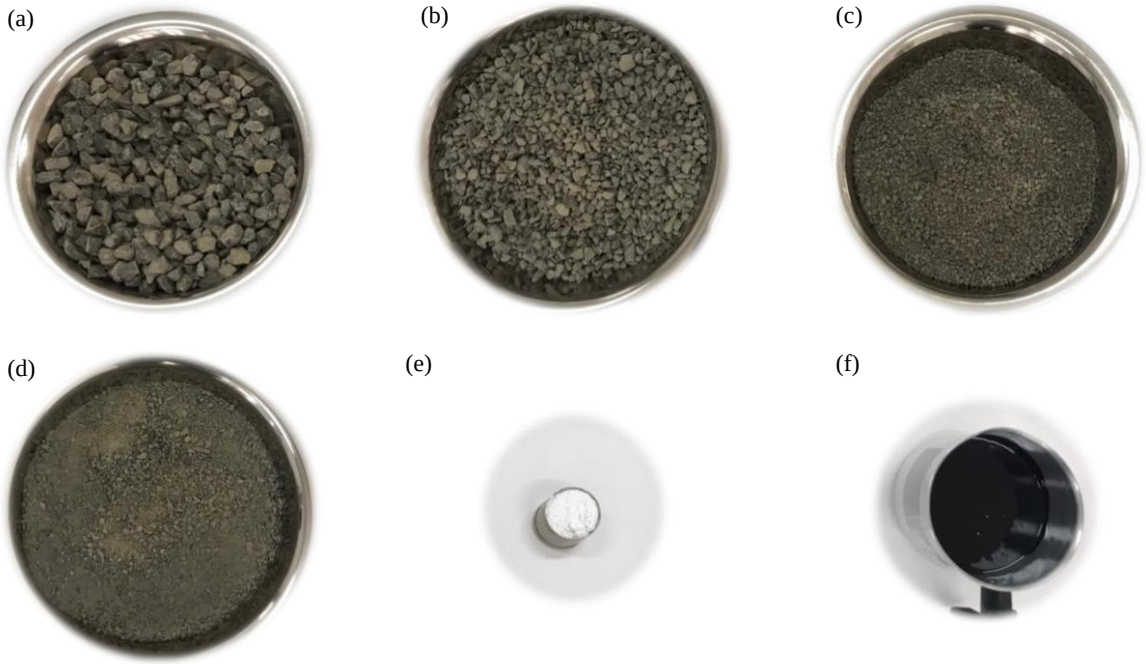

Figure 3.1 – Asphalt mixture materials: (a) crushed stone size number 67, (b) crushed stone size number 8, (c) stone dust size number 89, (d) stone dust classified as size number 10, (e) calcitic hydrated lime, (f) PG 82-16.

These materials were donated by the Bandeirantes quarry and asphalt plant in Sao Carlos, Sao Paulo, Brazil. This company also provided the laboratorial characterization of these materials and the HMA design. The stone aggregates are crushed from diabase rock. Both the aggregates and the filler were characterized through particle size analysis, according to the AASHTO T27 (2020) and T37 (2007). As the asphalt mixture was employed to high-traffic highways in the state of São Paulo, the hot mix asphalt (HMA) design was conducted to meet the requirements established by

ARTERIS ES027 (2021). Figure 3.2 presents the aggregate proportions, defined based on the individual particle size distribution curves. The aggregate mix design consists of 46% of crushed stone size number 67, 12% of crushed stone size number 8, 20% of stone dust size number 89, 20.5% of stone dust size number 10, and 1.5% of calcite hydrated lime. Figure 3.3 shows the hot mix asphalt design curve. As can be observed in Figure 3.3 the hot mix asphalt design curve falls within Range 3 - SPV 19 of ARTERIS ES027 (2021), as well as Range C of DNIT ES031 (2006), as shown in Figure 3.3.

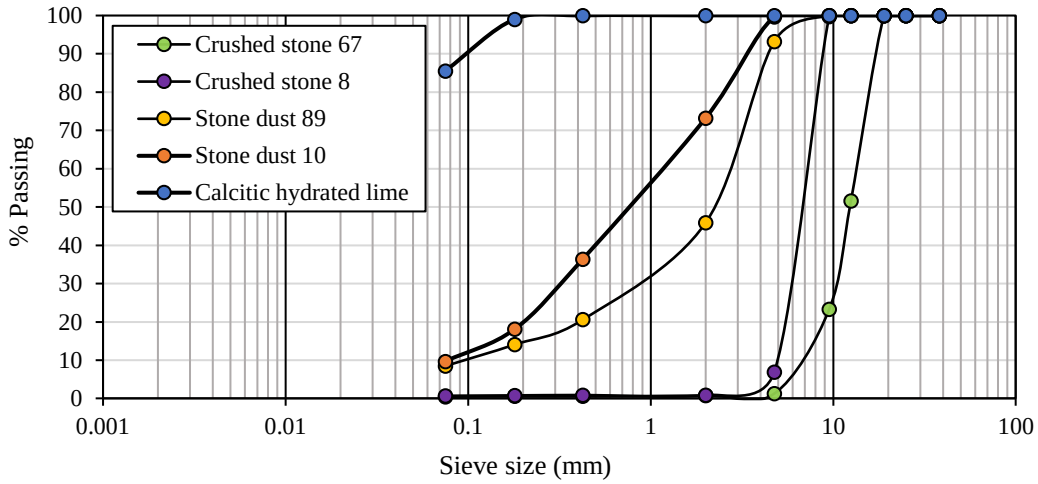

Figure 3.2 – Particle size distribution curves for each material composing the asphalt mixture.

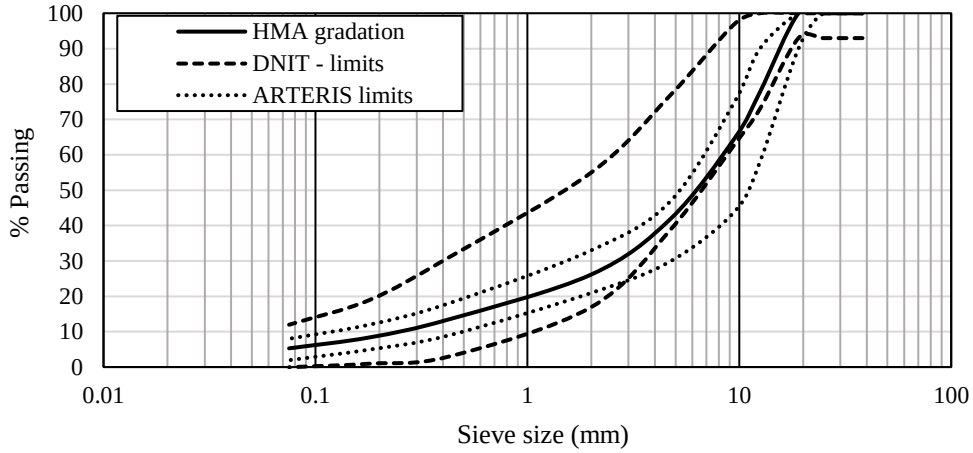

Figure 3.3 – HMA gradation.

The mixture curve exhibits a composition of 73.8% coarse aggregate, 20.9% fine aggregate, and 5.3% filler material, with a Nominal Maximum Size of 19 mm. The coarse aggregates underwent characterization through the Los Angeles abrasion test (ASTM C131, 2020), soundness in sodium sulfate (AASHTO T104, 2003), shape index (ASTM D4791, 2019), absorption, apparent specific gravity (G_{sa}), and bulk specific gravity (G_{sb}) (AASHTO T85, 2021). Characterization of the fine aggregate was conducted through tests for Sand equivalent (ASTM D2419, 2022), uncompacted void content (AASHTO T304, 2017), absorption, bulk and apparent specific gravity (AASHTO T84, 2013). Regarding the filler, the detection of harmful smectite clay was verified using methylene blue (AASHTO T330, 2007), along with specific gravity (AASHTO T133, 2019). These properties are presented in Tables 3.1 and 3.2.

Table 3.1 – Properties of aggregates.

Properties	Unit	Testing standard	Specification		Result
			ARTERIS	DNIT	
Los Angeles abrasion	%	ASTM C131	0-45	0-50	16.3
Soundness in sodium sulfate	%	AASHTO T104	0-12	0-12	2.6
Shape index	%	ASTM D4791	0-20	-	9
Sand equivalent	%	ASTM D2419	55-100	55-100	68.7
Uncompacted void content	%	AASHTO T304	45-100	-	45.7
Methylene blue value	mg/g	AASHTO T330	0-8	-	7

Table 3.2 – Absorption, bulk and apparent specific gravity.

Fraction	Absorption (%)	G_{sa}	G_{sb}
Course	1.49	2.964	2.838
Fine	3.38	2.975	2.703
Filler	-	2.791	2.791

Regarding the binder, ARTERIS ES027 accepts only PG 82-16, as non-modified binder, in its pavement projects. For this reason, PG 82-16 was employed in this study, which also complies with the National Department of Transport Infrastructure specifications in Brazil. Table 3.3 presents the PG 82-16 properties. The HMA design was conducted using the Marshall methodology, and the final proportion of the materials composing the HMA can be found in Table 3.4. Table 3.5 presents the HMA Properties.

Table 3.3 – Properties of PG 82-16.

Properties	Unit	ASTM Standard	Specification		Results
			Min	Max	
Penetration, 100 g, 5s, 25°C	0.1 mm	D5	30	45	31
Softening point	°C	D36	52	-	54
Fire point, °C	°C	D92	235	-	>235
Rotational viscosity, at 135 ºC, 20 r/min			374	-	478
Rotational viscosity, at 150 ºC, 50 r/min	cP	D4402	203	-	232
Rotational viscosity, at 177 ºC, 100 r/min			76	285	82

Table 3.4 – Final proportion of the materials composing the HMA.

Material	Proportion (%)
Crushed stone 67	44.02
Crushed stone 8	11.48
Stone dust 89	19.14
Stone dust 10	19.62
Calcium hydrated lime	1.44
PG 82-16	4.30

Table 3.5 – Properties of HMA.

Property	Unit	Result	Specification			
			ARTERIS		DNIT	
			Min	Max	Min	Max
Optimum binder content	%	4,3	4,1	4,5	4	-
Asphalt binder relative density	kg/m³	1011	-	-	-	-
Measured maximum specific gravity	kg/m³	2647	-	-	-	-
Bulk specific gravity	kg/m³	2540	-	-	-	-
Air void content	%	4	3	5	4	6
Voids filled with asphalt	%	70.1	65	75	65	72
Voids in the Mineral aggregate	%	13.4	13	15	15	-
Indirect tensile strength	MPa	1.9	1	-	0,65	-
Flow	mm	2.0	2	4.5	-	-

3.2 Tack coat

Two types of tack coat were employed to investigate the effect of the tack coat type on the bonding properties. One is a cationic rapid-setting asphalt emulsion type I (CRS-1), recommended in Brazil by DER ET-DE-P00/043 (2006), which provides guidance on reflective crack treatment with paving geosynthetic in road rehabilitation. Given the international recommendation for the use of asphalt cement with paving geosynthetics (Department of Transport and Main Roads, 2021), PG 58-16 was also selected as a tack coat. Table 3.6 presents the properties of PG 58-16, while

Table 3.7 shows those of CRS-1. To investigate the effect of the tack coat rate, three tack coat rates were selected: 400 g/m², 600 g/m², and 800 g/m².

Table 3.6 – Properties of PG 58-16.

Properties	Unit	ASTM standard	Specification		Result
			Min	Max	
Penetration, 100 g, 5s, 25°C, 0,1 mm	0,1 mm	D5	50	70	51
Softening point	°C	D36	52	-	49.3
Ductility, 25 °C	cm	D113			
Fire point, °C	°C	D92	235	-	>235
Relative density	kg/m³	D70			1011
Rotational viscosity, at 135 ºC, 20 r/min			374	-	478
Rotational viscosity, at 150 ºC, 50 r/min	cP	D4402	203	-	232
Rotational viscosity, at 177 ºC, 100 r/min			76	285	82

Table 3.7 – Properties of CRS-1.

Properties	Unit	ASTM standard	Specification		Result
			Min	Max	
Saybolt-furol viscosity at 25 °C	s	D7496	-	90	26
Sieve test	%	D6933	-	0.1	0
Charged particle	---	D7402	Positive		Positive
Content of residual binder	%	D6997	62	-	62.5

3.3 Paving geosynthetics

Nine geosynthetics representing a wide range of paving interlayers currently available in the geosynthetics market were selected to investigate the effect of different properties on bonding. The geosynthetics included paving geogrids, paving composites, and a paving mat. The products feature varied properties, including the presence of a nonwoven fabric backing, different geogrid mesh sizes, coating characteristics, thicknesses, and mechanical properties.

3.3.1 Paving composites and paving mat

The paving composite 1 (Pa-C-1) consists of a fiberglass geogrid, coated with oxidized bitumen, and contains a thermally bonded non-woven PP fabric backing. Pa-C-1 has the peculiar aspect of a top surface sprinkled with sand particles. The paving composite 2 (Pa-C-2) is composed of a fiberglass geogrid needle-punched to an ultralight weight non-woven PP fabric backing, both

coated with bitumen. The paving composite 3 (Pa-C-3) contains a fiberglass geogrid coated with bitumen and thermally bonded to a heavy weight non-woven polyester fabric backing. The paving composite 4 (Pa-C-4) is composed of a polyvinyl alcohol (PVA) geogrid needle-punched to an ultralight weight non-woven PP geotextile, both coated with bitumen. The paving mat (P-M) is manufactured by incorporating a microfiber glass mesh into a non-woven PET fabric with elastomeric coating. Figure 3.4 presents the paving composites and paving mat.

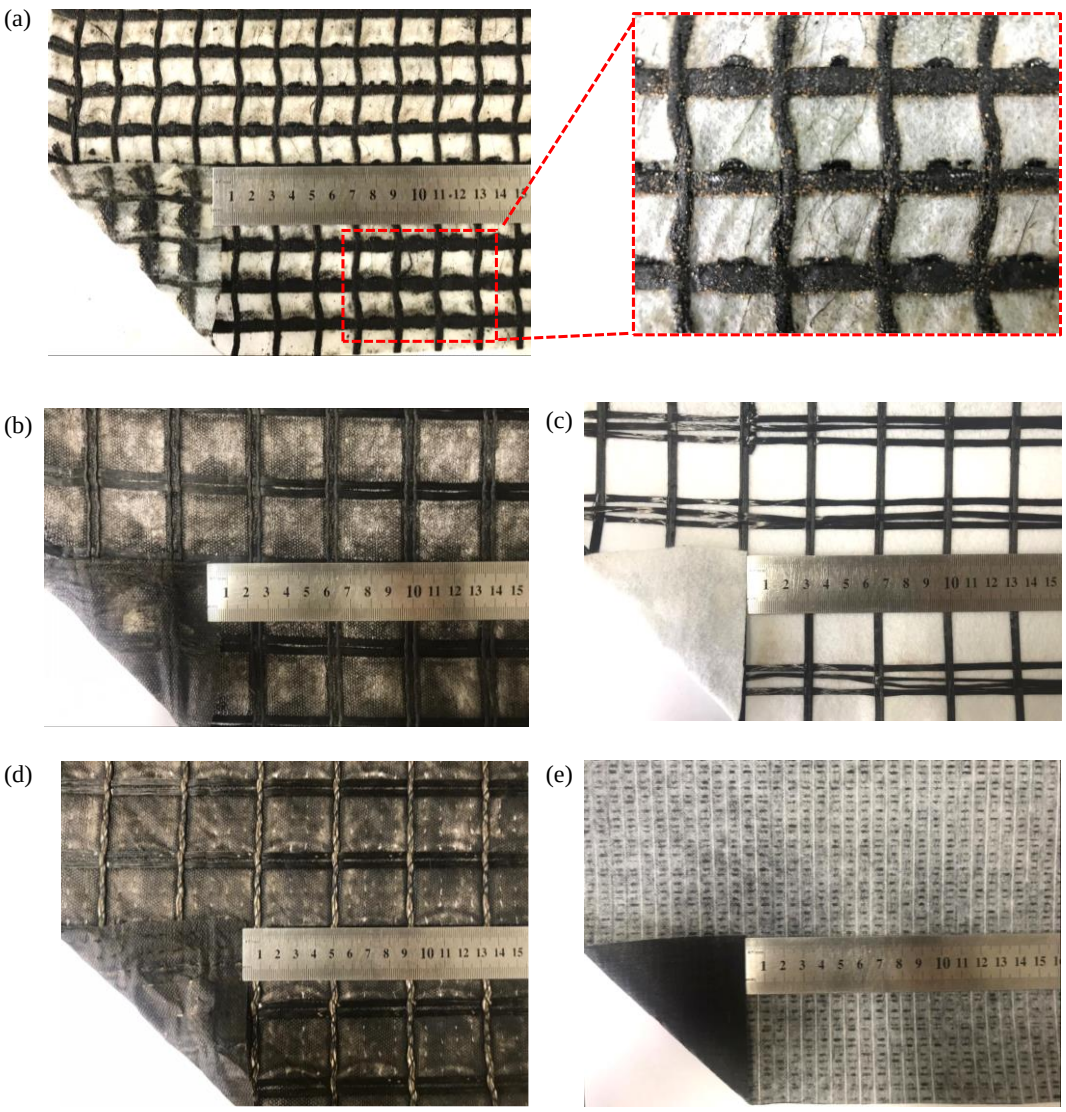

Figure 3.4 – Paving composites and paving mat: (a) Pa-C-1, (b) Pa-C-2, (c) Pa-C-3, (d) Pa-C-4, and (e) P-M.

3.3.2 Paving geogrids

All paving geogrids used in this study are made of fiberglass, with ultimate tensile strength (>50 kN/m). However, the paving grids exhibit different physical properties, such as geogrid mesh and bitumen pre-impregnation coating content. Paving geogrid 1 (Pa-G-1) has a polymer-modified bituminous coating, and contains wide yarns, resulting in a comparatively smaller geogrid mesh. Paving geogrid 2 (Pa-G-2) is self-adhesive, has a bituminous coating, and features a comparatively smaller geogrid mesh. Paving geogrid 3 (Pa-G-3) is self-adhesive, coated with polymeric coating. Paving geogrid 4 (Pa-G-4) is coated with bitumen and contains thin strips of fabric that cross the geogrid mesh. Figure 3.5 shows the paving geogrids.

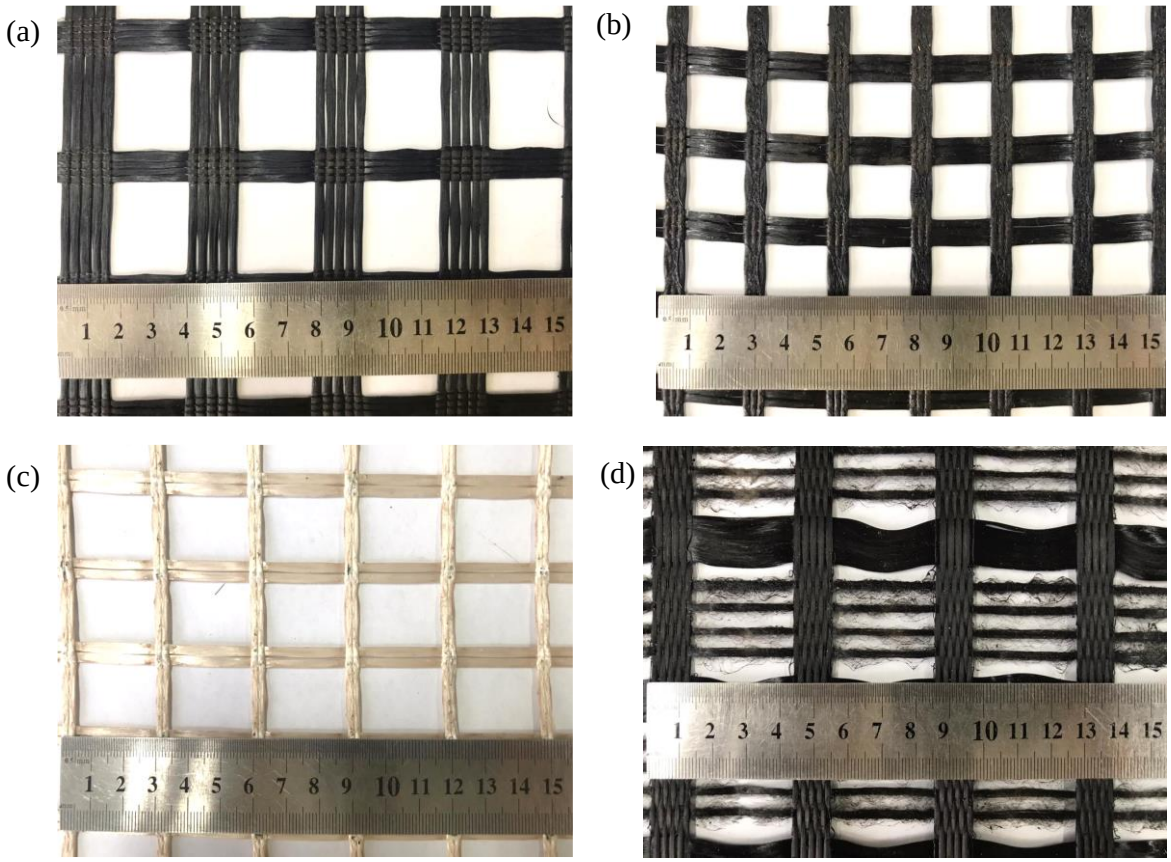

Figure 3.5 – Paving grids: (a) Pa-G-1, (b) Pa-G-2, (c) Pa-G-3, (d) Pa-G-4.

3.3.3 Geosynthetic properties

Tests were conducted to determine the physical properties of the geosynthetics, such as nominal thickness under 2 kPa (ASTM D5199, 2019), longitudinal and transverse thickness and width of the geogrid yarns, mass per unit area of the geosynthetic (ASTM D5261, 2018), and mass per unit area of the fabric backing (ASTM D5261, 2018). Figure 3.6 presents the typical identification of the yarns and the measurements taken.

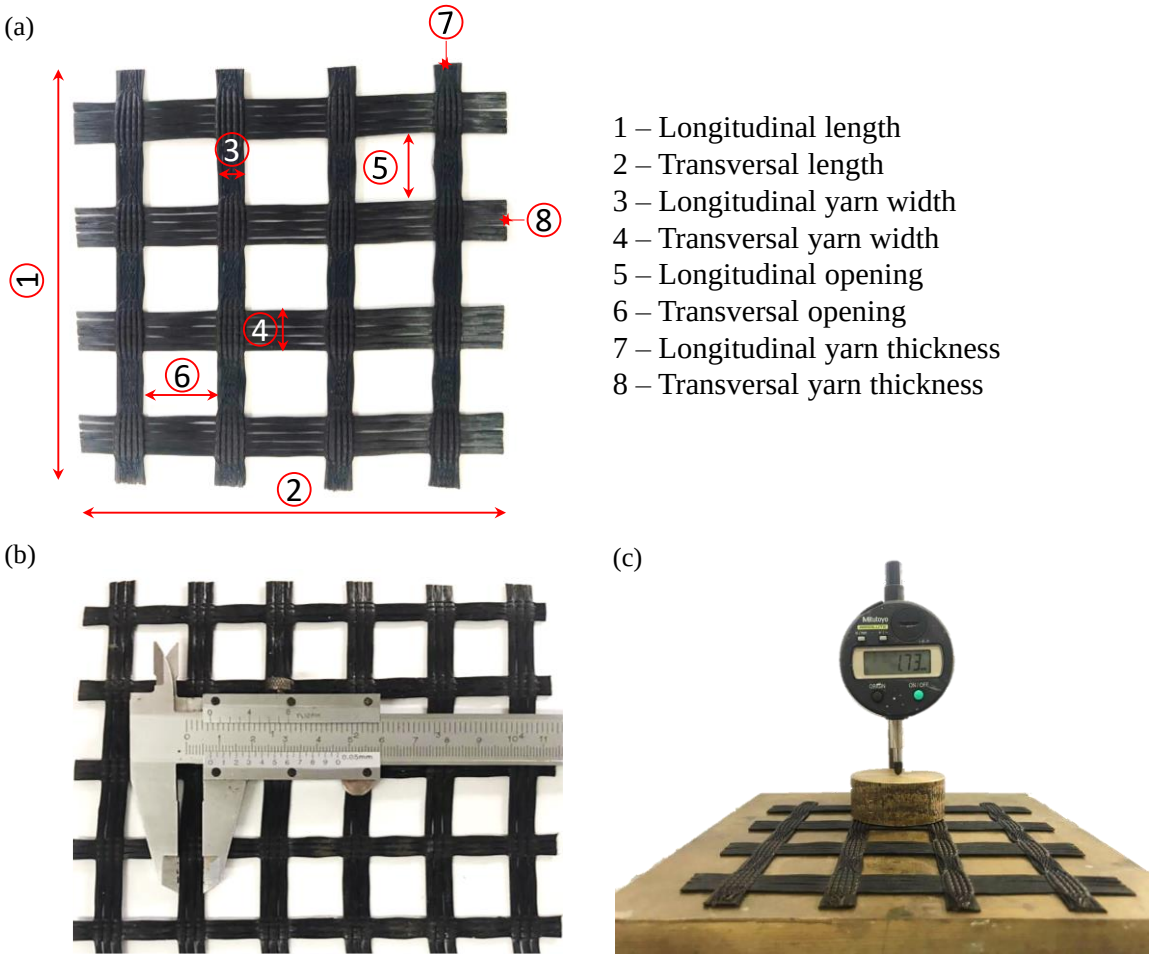

Figure 3.6 – Physical characterization of geosynthetics: (a) identification of measurements, (b) measurement of the longitudinal yarn, (c) nominal thickness under 2 kPa.

The index asphalt retention of the paving composites and the paving mat were determined following the specifications on ASTM D6140 (2022). The tests were conducted using PG 58-16 as well as adaptations for CRS-1. For sampling, 8 specimens of 10 x 20 cm were required, with 4 in

the longitudinal direction and 4 in the transverse direction. The testing method in ASTM D6140 (2022) involves immersing the paving geosynthetic in heated asphalt binder for 30 minutes in an oven at 135 °C, followed by hanging the specimens in the oven to drain. The specimens were hung for 30 minutes at each end. After this process, the specimens are removed from the oven and hung outside the oven for 30 minutes to cool before weighing the saturated material. Figure 3.7 illustrates the procedure with PG58-16.

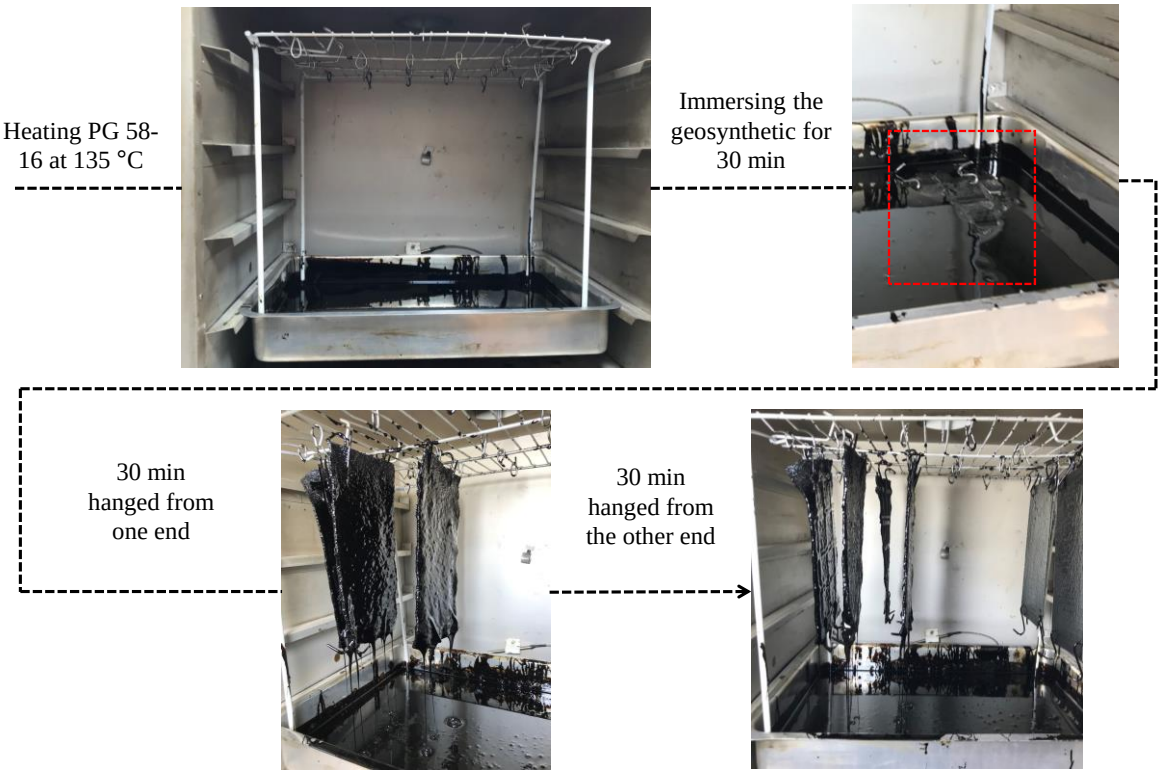

Figure 3.7 – Index asphalt retention procedure using PG 58-16.

In the case of CRS-1, the ASTM D6140 (2022) procedure was adapted by excluding the heating and draining step in the oven. This modification is necessary to replicate the application of the CRS-1 in the field, which is carried out at ambient temperature. Thus, the testing procedure involved immersing the samples in the emulsion at 25ºC for 30 minutes, followed by draining for 30 minutes at each end. Figure 3.8 illustrates the procedure with emulsion CRS-1.

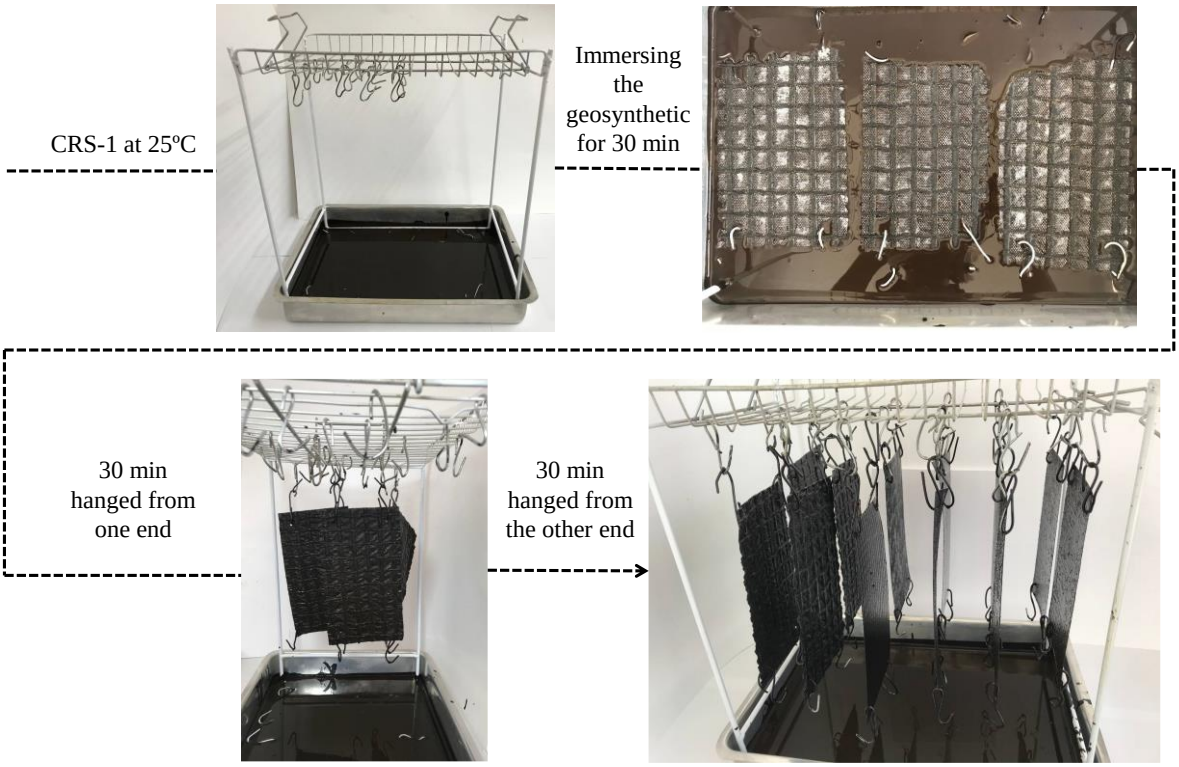

Figure 3.8 – Index asphalt retention procedure using CRS-1, adapted from ASTM D6140.

Most of paving geosynthetics selected contain a bitumen coating that is sprayed during fabrication process and is intended to enhance the bonding between the paving geosynthetic and asphalt layers. To evaluate the bitumen content coating (B_{cc}) of paving geosynthetics, a test methodology was developed since there is no available standard testing procedure to obtain this property. Bitumen content of coating analysis were added to this investigation as an important component to understand if this property can affect the bonding properties.

The test method comprises the following materials:

- Scale with sufficient capacity and sensitivity to weigh specimens with precision of 0.001 g.
- Perchloroethylene solvent.
- Glass container with metallic lid.
- Glass funnel.

The test procedure involved cutting the paving geosynthetic specimens with minimum dimensions of 60 mm x 60 mm. In the presence of a geogrid, samples were cut between nodes to guarantee the mesh connection. Initially, the specimen's initial weight (w_i) is measured. Then, the

specimen is placed inside a glass container. Using a glass funnel, perchloroethylene solvent is poured to ensure the geosynthetic is fully immersed in the solvent. The container is then capped so that the solvent does not evaporate. After 24 hours, the specimens are removed from the container and dried for an additional 24 hours to allow the solvent to evaporate, determining the final weight (w_f) of the sample. The bitumen content of the coating (B_{cc}) is determined according to Equation 3.1:

$$B_{cc} = \frac{w_i - w_f}{w_i} \times 100 \tag{3.1}$$

It is worth noting that the test was also conducted with a 48-hour immersion period. However, either there was no difference in mass, or the difference was at most 0.002 g, resulting in a variation of less than 0.1% in the bitumen content of the coating. For this reason, the test was standardized with a 24-hour immersion. Figure 3.9 illustrates some stages of the procedure, and Table 3.8 summarizes the properties of the paving geosynthetics used in this study.

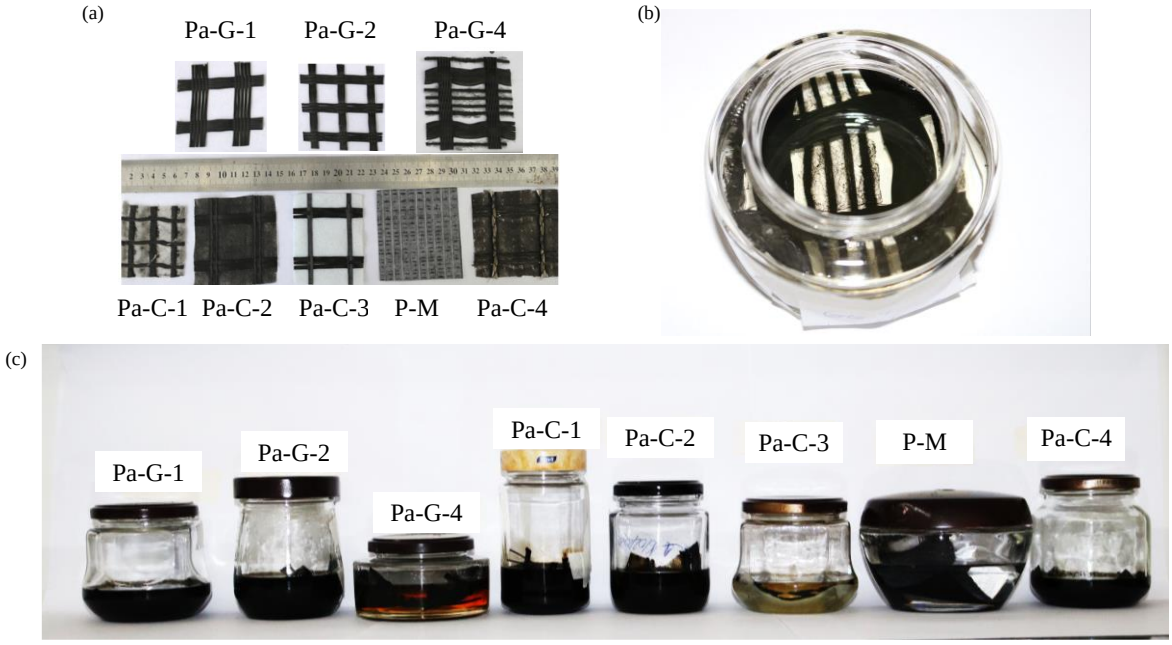

Figure 3.9 – Bitumen content of the coating testing: (a) specimens, (b) geosynthetic immersed in perchloroethylene solvent, (c) test after 24 hours.

Table 3.8 – Properties of the paving geosynthetics.

Property	Pa-G-1	Pa-G-2	Pa-G-3	Pa-G-4	Pa-C-1	Pa-C-2	Pa-C-3	Pa-C-4	P-M
Geogrid composition	Fiberglass	Fiberglass	Fiberglass	Fiberglass	Fiberglass	Fiberglass	Fiberglass	PVA	Micro fiberglass mesh
Fabric composition	-	-	-	-	PP	PP	PET	PP	PET
Coating	Bitumen	Bitumen	Polymeric	Bitumen	Bitumen on geogrid only	Bitumen	Bitumen on geogrid only	Bitumen	Elastomeric
Geogrid aperture dimensions (mm x mm)	24 x 28	17 x 19	20 x 25	35 x 31	13 x 16	31 x 32	31 x 30	32 x 39	-
Mass per unit area (g/m²)	606	664	413	613	691	326	382	232	145
Mass per unit area of nonwoven geotextile backing (g/m²)	-	-	-	-	24.45	27.5	168.4	46.5	-
Longitudinal rib width (mm)	10.15	6.45	4.35	11.35	3.25	5.9	4.05	3.35	-
Longitudinal rib thickness (mm)	1.1	0.9	1.05	0.7	1.1	0.9	1.1	1.05	-
Transversal rib width (mm)	14.15	8.2	6.45	13	5.25	8.5	10.7	9.1	-
Transversal rib thickness (mm)	0.7	0.75	0.65	0.9	1.6	0.6	1.1	0.65	-
Geogrid coverage area	0.57	0.51	0.36	0.54	0.48	0.36	1.00	0.30	-
Geosynthetic thickness (mm)	1.6	1.6	1.5	1.15	1.80	1.35	1.80	1.58	0.45
Nonwoven fabric backing thickness (mm)	-	-	-	-	0.10	0.13	1.35	0.22	-
Tensile strength (kN/m) – Longitudinal*	120	120	100	130	120	50	50	50	25
Tensile strength (kN/m) – Transversal*	120	120	100	130	120	50	50	50	25
Tensile stiffness at 2% strain*	4000	5750	3650	6150	4000	3687	2648	1433	434
Elongation at break*	≤ 3%	≤ 4%	≤ 3%	≤ 3%	≤ 3%	≤ 3%	≤ 3%	≤ 6%	≤ 5%
Asphalt retention (g/m²) – PG 58-16	-	-	-	-	423	421	1554	432	440
Asphalt retention (g/m²) – CRS-1	-	-	-	-	223	407	748	407	204
Bitumen content of the coating (%)	8.6	7.5	-	1.8	49.2	13.5	0.5	12.1	-

*Property provided by the manufacturer.

CHAPTER 4. DOUBLE-LAYERED ASPHALT SPECIMENS WITH PAVING GEOSYNTHETICS

4.1 Compaction method

The test specimens for interface shear bond and shear fatigue tests were produced with a diameter of 150 mm, geometry recommended for double-layered asphalt specimens with paving geosynthetic (Correia et al., 2023; Giri and Panda, 2018; Pasetto et al., 2019; Sudarsanan et al., 2018b). The compaction method adopted for this study was the Marshall method. However, as the asphalt specimens were produced with a diameter of 150 mm, two adaptations were made to the Marshall compaction method. Mold cylinders with a diameter of 150 mm and a pedestal for compaction were fabricated. Figure 4.1 illustrates Marshall apparatus used in this study.

The first adaptation concerns energy compatibility. Thus, Equation 4.1 was used to determine the compaction energy based on data from the traditional methodology, i.e., a hammer with 4540 g of drop mass, free fall length of 457.2 mm, 150 blows, and a volume of 498.73 x 10^3 mm^3, for the specimen with a diameter of 100 mm and a height of 63.5 mm (ASTM D6926, 2020). Next, to determine the number of blows for a 150 mm diameter specimen, a height of 40 mm was standardized at the end of compaction. Consequently, with the energy value and the volume of the asphalt layer, the quantity of 213 blows was obtained. The second adaptation relates to the compaction method. Since the specimens comprises two asphalt layers, it was decided to apply the blows on only one face in each layer, to maintain the same procedure for both asphalt layers. This adaptation was based on studies involving double-layer asphalt specimens with a diameter of 100 mm (D'Andrea and Tozzo, 2016; Tozzo et al., 2016, 2015, 2014b).

(a) (b) (c)

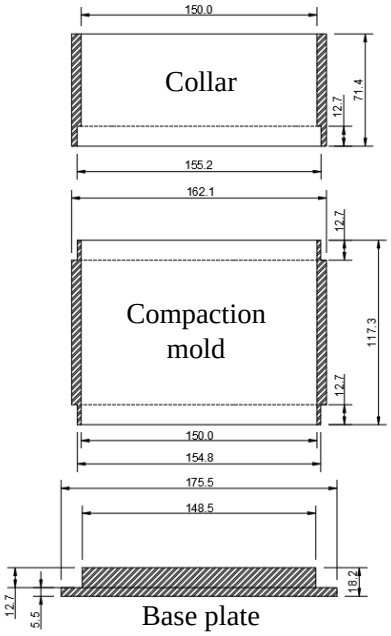

Dimensions in mm

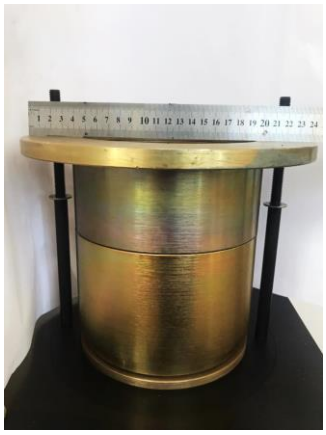

Figure 4.1 – Marshall apparatus: (a) design of the compaction mold assembly, (b) compaction mold assembly, (c) compaction pedestal.

$$E_c = \frac{M \cdot H \cdot N}{V} \tag{4.1}$$

Where E_c is the compaction energy, M is the drop weight, H is the drop height, N is the number of blows, V is the volume of the asphalt layer.

4.2 Specimen preparation

The mixing and compaction temperature ranges were selected to produce a viscosity of 170 ± 20 cP and 280 ± 30 cP based on rheological curve of PG 82-16. Figure 4.2 presents the mixing and compaction temperature ranges. The binder PG 82-16 was heated to the range of the mixing temperature. The aggregates were heated to a temperature above the mixing temperature range by 15 ºC, but not exceedingly more than 177 ºC.

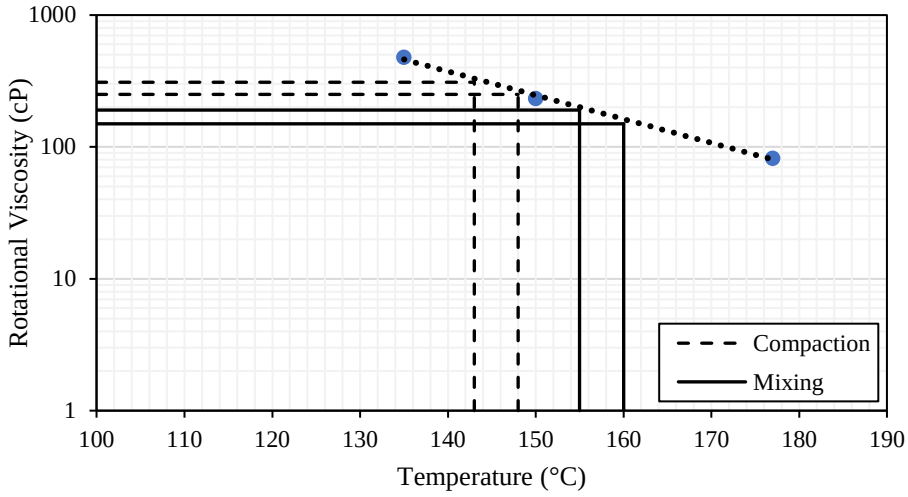

Figure 4.2 – Mixing and compaction temperature ranges.

The HMA for the bottom layer of each specimen was prepared by mixing the preheated aggregates and PG 82-16 at the range of the mixing temperature. The HMA was then poured into a mold cylinder and compacted following the adapted Marshall method. Following compaction, the bottom asphalt layer was allowed to cool for 24 hours before being removed from the mold. Subsequently, a tack coat was applied to its upper surface. For specimens utilizing CRS-1, this tack coat was applied at the target rate using a paint brush. The residual tack coat rate was checked post-emulsion break to ensure proper application. PG 58-16 was heated and poured onto the top surface of the bottom asphalt layer, with the correct amount of tack coat verified during application using a scale. To spread the tack coat evenly, a metal spatula and heat gun were utilized following the procedure outlined in Safavizadeh et al. (2022).

In the case of double-layered asphalt specimens with paving geosynthetics, the paving geosynthetic was placed immediately after the application of PG 58-16 and spreading of the tack coat, instead of following emulsion break. Once placed, the position of the longitudinal geogrid yarns was marked for shear testing alignment. The bottom asphalt layer was then reinserted into the mold, and the upper layer was compacted. Both layers were compacted to a target density of 93 ± 1%, which correspond to an air void of 7 ± 1%, as per the ASTM D2726 (2017). These values align with the recommended range in Report No. FHWA-HIF-21-021 (FHWA, 2020).

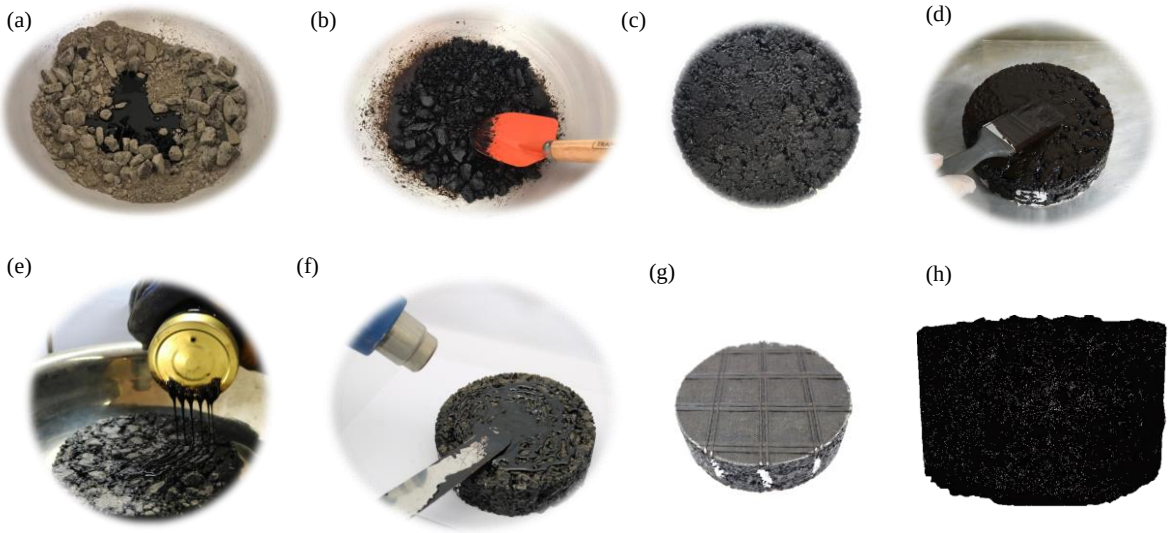

Figure 4.3 – Production of double-layered asphalt specimens with paving geosynthetics: (a) pre-heated binder and aggregates, (b) mixing, (c) compacted bottom asphalt layer, (d) application of CRS-1, (e) application of PG 58-16, (f) spreading PG 58-16, (g) Placement of the geosynthetic, (h) prepared specimen.

CHAPTER 5. INTERFACE SHEAR BOND TEST

5.1 Multifunctional interface shear testing device

A new testing device for performing static and dynamic interface shear testing was designed and developed in this study. The testing device is denominated Multifunctional Interface Shear Tester (MIST). This device is capable of conducting various test configurations: Leutner testing (Leutner, 1979), Cyclic Ancona Shear Testing Research And Analysis (C-ASTRA) testing (Ragni et al., 2019), and Louisiana Interface Shear Strength Tester (LISST) testing (Mohammad et al., 2009). MIST device was designed to accommodate both static and dynamic loading configurations of testing. It is noteworthy that the Leutner testing and ASTRA testing are approved by pr-EN 12.697-48 (European Standard, 2021), and the LISST testing is specified in AASHTO TP 114 (2018). Figure 5.1 depicts the schematic views of the MIST device.

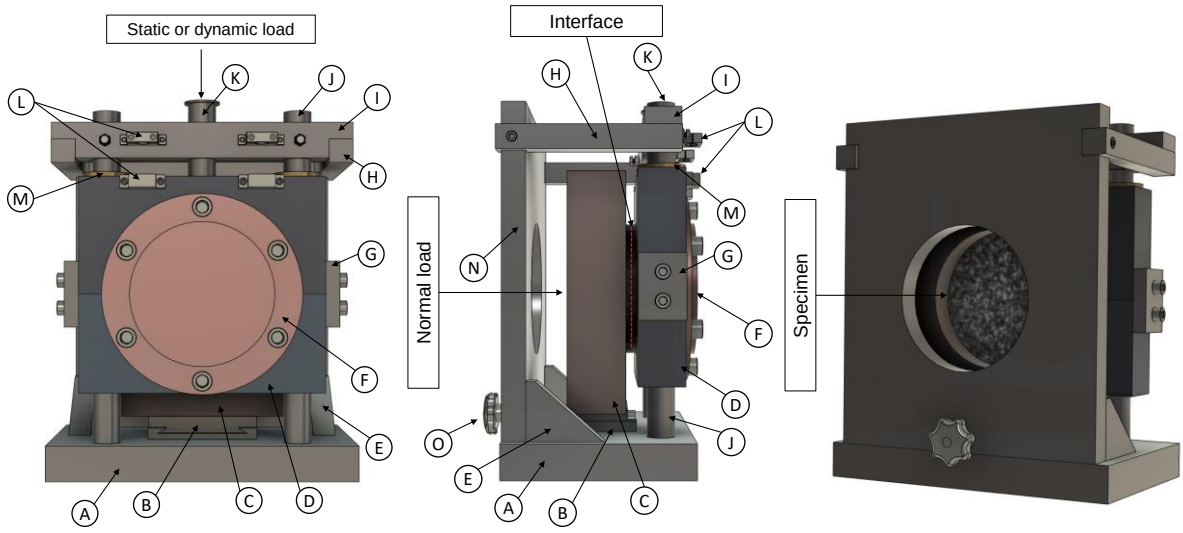

Figure 5.1 – Multifunctional interface shear testing (MIST) device.

The MIST device consists of stationary compartment (C) and bipartite movable compartment (D) separated by an adjustable gap. The movable compartment slides vertically on two vertical bar guides (J) by means of a metal sleeve (M). The vertical bar guides are fixed to a horizontal base (A). A horizontal beam (I) maintains the two vertical bar guides vertically aligned and is connected to the vertical base (N) by means of two horizontal bars (H). A movable pin (K)

allows the application of a vertical load on the movable compartment to shear the interface of the double-layered asphalt specimen. The stationary compartment can move horizontally along a plate guide (B), also fixed to the horizontal base, to adjust the gap (from no gap to 25 mm) using thread star shaped head clamping screw knob (O). The assembly is stiffened by means of two triangular steel plates welded to the horizontal and vertical base. The MIST device allows applying a constant horizontal stress by means of a pneumatic actuator. In the case of applying a horizontal stress, a metal disk (F) can be connected to the movable compartment. The application of normal stress allows conducting LISST and ASTRA tests. Two LVDTs can be installed to measure the shear displacements during dynamic shear tests by means two external supports (L).

The MIST device was primarily based on the C-ASTRA model, with adaptations for Leutner or LISST-type tests. There are two differences between MIST and the C-ASTRA: the first relates to the opening of the compartments (C and D) that receive the test specimen, increasing from 100 mm to 150 mm in diameter, as this geometry is recommended for double-layered asphalt specimen with paving geosynthetic (FGSV 770, 2013). The second is related to the movable compartment (D); in contrast to the model presented by Ragni et al. (2019), the movable compartment was designed to be split horizontally in the center of the diameter with removable connectors on the sides (G). This modification will provide versatile functionality, as by removing the lateral connectors and element "G" the test specimen will be subjected to the shearing action of the upper half of the movable face. Thus, the MIST can also function as a Leutner device (Leutner, 1979). Figure 5.2 presents the test configurations that can be performed by MIST.

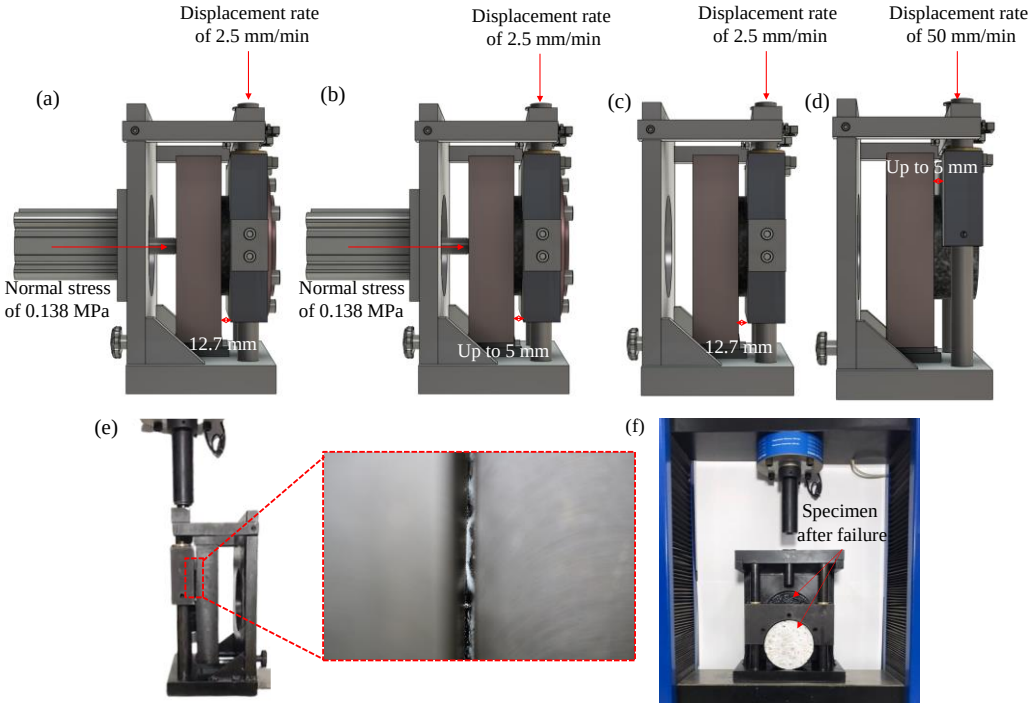

Figure 5.2 – Different test configurations: (a) LISST configuration with normal stress, (b) ASTRA configuration with normal stress, (c) LISST configuration without normal stress, (d) Leutner shear test configuration; (e) side view of the gap interface, (f) front view after conducting Leutner shear test.

5.2 Leutner shear tests

Recommendations for interface shear bond test for double-layered asphalt specimen with paving geosynthetic are issued by Germany Working FGVS 770 (2013), using Leutner shear testing device and testing specimen with a diameter of 150 mm.

In the present study, interface shear bond tests were conducted using a servo-controlled test machine, with tests performed under a shear displacement rate of 50.8 mm/min at a temperature of 20°C, following the European standard EN 12697-48 (2021). The procedure involved fixing the bottom asphalt layer of the specimen in the device, while the upper asphalt layer was subjected to vertical load, without applying normal stress.

As per European standard EN 12697-48 (2021), it is suggested to maintain a gap of up to 5 mm between the shearing compartments to prevent potential edge damage resulting from misalignment of the specimen interface with respect to the shear plane. For this study, a 3-mm-wide gap was chosen, following the procedure recommended by Collop et al. (2009), Petit et al. (Petit et al., 2018) and Canestrari et al. (2018).

Hence, the research conducted in this study utilized the MIST device in the Leutner configuration. The validation of the Leutner configuration involved a comparative analysis between the results derived from the MIST in this specific configuration and those obtained from a commercially available version of the Leutner device present in the Geotechnical Laboratory at the Federal University of Sao Carlos. An independent t-test was conducted to assess whether there existed a significant difference between the MIST and the commercial Leutner devices. If the p-value exceeds the significance level of 0.05, it implies that the outcomes do not exhibit a significant difference from each other. Comparable results were obtained from a double-layered asphalt specimen with the same tack coat rate and type.

Table 5.1 presents the results of equality of means of *ISS* and *k* between the results derived from the MIST in the Leutner shear test configurations and those obtained from a commercial version of the Leutner device. As observed in Table 5.1, the results indicate that MIST can be used in the Leutner shear test configuration, as p-values were greater than 0.05. This suggests that, in terms of *ISS* and *k*, there is no significant difference from the commercial version of the Leutner shear test device.

Table 5.1 – Equality of means of *ISS* and *k* between the results derived from the MIST device in Leutner configuration and those obtained from a commercially available version of Leutner shear test device.

Bonding properties	t	Degrees of freedom	p
ISS	-2.058	4	0.109
k	0.585	4	0.590

5.3 Procedure for determining minimum interface shear strength

According to the German working group FGSV 770 (2013), the minimum interface shear strength (*ISS)* requirement for core fields of asphalt overlays with paving geosynthetic is specified as 0.56 MPa (equivalent to 10 kN) with a core diameter of 150 mm. However, Canestrari et al. (2022b) propose a 50% increase in the minimum acceptable *ISS* value for laboratory-produced specimens, thereby establishing a minimum requirement of 0.84 MPa.

Simply comparing the average Interface Shear Strength (ISS_{meas}) of a sample with the required minimum (ISS_{min}) does not reliably ensure compliance with the minimum ISS requirement. This uncertainty stems from result variability and generally small sample sizes, making it unclear if the true mean (population mean) surpasses ISS_{min}. To adequately assess ISS value against a

specified $ISS_{\min}$, estimating a Confidence Interval (CI) for the true mean of ISS (ISS_{tm}) is necessary. Given the sample size (n) is below 30 and both the true mean and variance are unknown, adopting a CI for the t-distribution is appropriate. This approach allows determination of the lower t confidence limit of a confidence interval on ISS_{tm}. Equation 5.1 shows the estimation of the lower t confidence limit of a confidence interval on ISS_{tm}.

$$ISS_{meas} - t_{\alpha,n-1} \cdot s/\sqrt{n} \leq ISS_{tm} \tag{5.1}$$

Where ISS_{meas} is the sample's average *ISS* value measured, α is the significance level, $t_{\alpha, n-1}$ is 100α percentage point of the t distribution with n – 1 degrees of freedom, *s* is the sample standard deviation, n is the sample size, and ISS_{tm} true mean of the *ISS.* In this case, the lower *t* confidence limit should equal or exceed the ISS_{min}, as follows:

$$ISS_{meas} - t_{\alpha,n-1} \times s/\sqrt{n} \geq ISS_{\min} \tag{5.2}$$

Based on Equation 7.2, a correction coefficient (ϕ) is proposed to facilitate checking the minimum value required in terms of *ISS*. ϕ is given by Equation 5.3 and can be calculated as follows:

$$ISS_{meas} \geq ISS_{\min} + t_{\alpha,n-1} \times s/\sqrt{n}$$

$$ISS_{meas} \geq ISS_{\min}\left(1 + \frac{t_{\alpha,n-1} \times s/\sqrt{n}}{ISS_{\min}}\right)$$

$$ISS_{meas} \cdot 1\Big/\left(1 + \frac{t_{\alpha,n-1} \times s/\sqrt{n}}{ISS_{\min}}\right) \geq ISS_{\min}$$

$$\phi = 1 \Big/ \left(1 + \frac{t_{\alpha,n-1} \times s / \sqrt{n}}{ISS_{\min}} \right) \tag{5.3}$$

Table 5.2 presents different values of ϕ for 95% confidence level based on the type of specimen, sample size, and standard deviation. This means that if ISS_{mens} times ϕ is equal to or greater than the ISS_{min}, as presented by Equation 5.4, the true mean of the interface shear strength (ISS_{tm}) will be greater than the minimum interface shear strength (ISS_{min}) required at a minimum 95% confidence level.

Table 5.2 – Values of ϕ for 95% confidence level.

			ϕ							
Type of specimen	ISS_{min} (MPa)	Sample size	Standard deviation (MPa)							
			0.35	0.30	0.25	0.20	0.15	0.10	0.05	0.01
Extracted from the field	0.56	2	0.26	0.29	0.33	0.39	0.46	0.56	0.71	0.93
		3	0.49	0.53	0.57	0.62	0.69	0.77	0.87	0.97
		4	0.58	0.61	0.66	0.70	0.76	0.83	0.90	0.98
		5	0.63	0.66	0.70	0.75	0.80	0.85	0.92	0.98
		6	0.66	0.69	0.73	0.77	0.82	0.87	0.93	0.99
		7	0.69	0.72	0.75	0.79	0.84	0.88	0.94	0.99
		8	0.70	0.74	0.77	0.81	0.85	0.89	0.94	0.99
		10	0.73	0.76	0.79	0.83	0.87	0.91	0.95	0.99
Laboratory-prepared	0.84	2	0.35	0.39	0.43	0.48	0.56	0.65	0.79	0.95
		3	0.59	0.62	0.67	0.71	0.77	0.83	0.91	0.98
		4	0.67	0.70	0.74	0.78	0.83	0.88	0.93	0.99
		5	0.72	0.75	0.78	0.81	0.85	0.90	0.95	0.99
		6	0.74	0.77	0.80	0.84	0.87	0.91	0.95	0.99
		7	0.77	0.79	0.82	0.85	0.88	0.92	0.96	0.99
		8	0.78	0.81	0.83	0.86	0.89	0.93	0.96	0.99
		10	0.81	0.83	0.85	0.88	0.91	0.94	0.97	0.99

$$ISS_{meas} \cdot \phi \geq ISS_{\min} \tag{5.4}$$

5.4 Experimental program for interface shear bond tests

According to Montgomery (2017), when multiple factors influence the response variable, the correct approach is to conduct a factorial experiment. In this strategy, the selected factors are

varied simultaneously, rather than one at a time. For this reason, the experimental design was implemented through a factorial experiment.

The experimental design for interface shear bond tests was conducted to evaluate the effect of different paving geosynthetics, tack coat type and application rate on shear bond properties. Table 5.3 outlines the factors and their respective levels. Regarding the chosen tack coat rates, it encompasses the range of tack coat rates typically applied in the field. In total, 60 combinations of different interfaces will be tested, each conducted with a minimum of three replications, resulting in a total of 180 specimens.

Table 5.3 – Experimental program for interface shear bond tests.

Factor	level 1	level 2	level 3	level 4	level 5	level 6	level 7	level 8	level 9	level 10
Geosynthetic type	control	Pa-G-1	Pa-G-2	Pa-G-3	Pa-G-4	Pa-C-1	Pa-C-2	Pa-C-3	Pa-C-4	P-M
Tack coat type	CRS-1	PG 58-16	-	-	-	-	-	-	-	-
Tack coat rate (g/m²)	400	600	800	-	-	-	-	-	-	-

In accordance with the recommendations of Montgomery (2017), for a proper data analysis through statistical methods, leading to valid and objective conclusions, it is necessary to adhere to the principles of randomization, replication, and blocking. Hence, throughout the execution of the experiments in the present study, these principles were rigorously followed.

CHAPTER 6. SHEAR FATIGUE TEST

6.1 Dynamic testing machine

This study involved the development of an electropneumatic dynamic testing machine equipped with integrated software tailored for conducting shear fatigue tests. The dynamic testing machine was designed to perform cyclic tests with a frequency range between 1 and 10 Hz, featuring a loading pulse with a duration of 0.1 s in haversine waveform and a maximum applied load of 16 kN. This is approximately corresponded to a maximum stress of 900 kPa for a test specimen with a diameter of 150 mm. Figure 6.1 presents the electropneumatic dynamic testing machine developed for the present study.

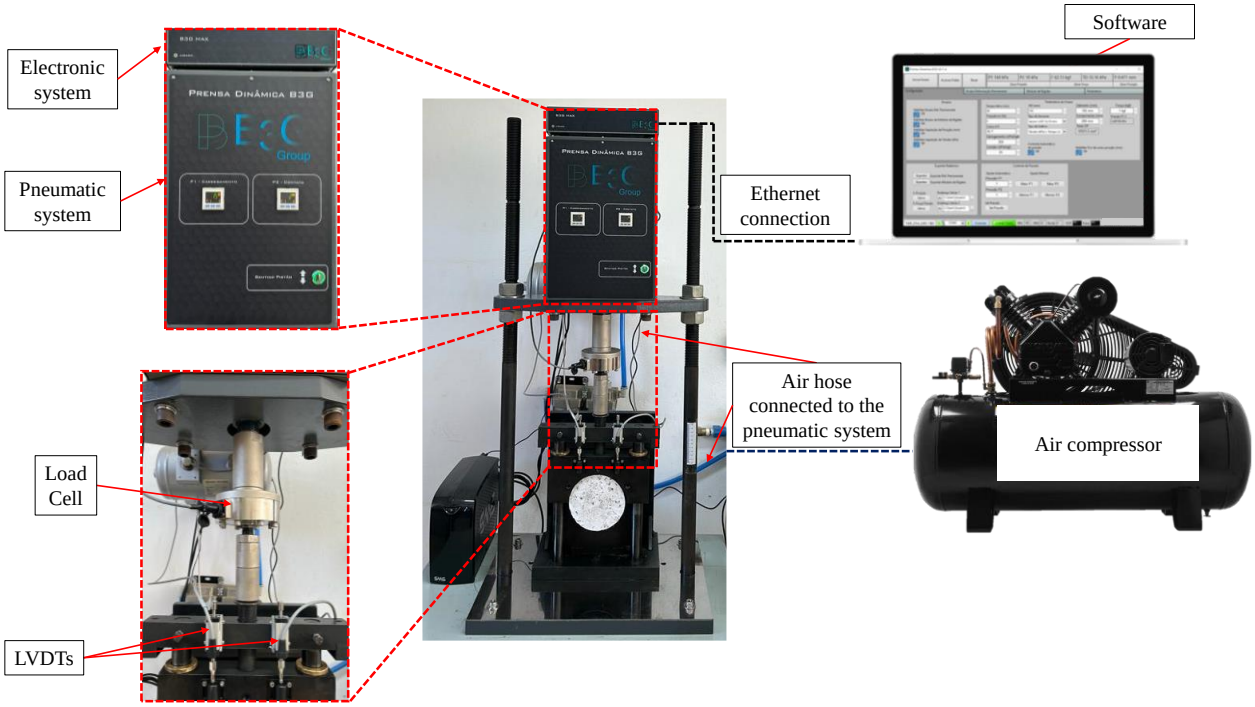

Figure 6.1 – Electropneumatic dynamic testing machine.

As detailed in Figure 6.1, the dynamic testing machine comprises two systems: a pneumatic system and an electronic system. The pneumatic system includes two directional valves, precision pressure regulators, and a low-friction compact actuator with a diameter of 160 mm, and stroke of 30 mm. The pneumatic system is powered by a 5-horsepower, 20-foot, 200-liter air compressor.

The electronic system features a 16-bit microprocessor-based electronic board to acquire load data with a resolution of 0.05 N and displacement data with a resolution of 0.001 mm. Displacement is measured using two 10 mm stroke linear variable displacement transducers (LVDT), while the load is measured by a load cell with a maximum capacity of 20 kN.

A software with a graphical interface was developed using LabView® to configure tests through user interaction. Input data are applied to logical functions with proportional–integral–derivative controller to perform test frequency control. The output data is recorded by the controller board through LVDTs and a load cell. In order to establish communication between the dynamic testing machine and the software, the electronic board communicates with the computer via Ethernet. At the end of the test, the software provides the recorded displacement and load data in text format.

The software presents three tabs: (I) test configuration, (II) real-time visualization of the permanent displacement curve versus the number of cycles, load and displacement pulses, and (III) real-time visualization of the cyclic interface shear stiffness modulus. Figures 6.2 to 6.4 present the software tabs. The capability to have real-time visualization of the fatigue parameters provides to check the progress of the test.

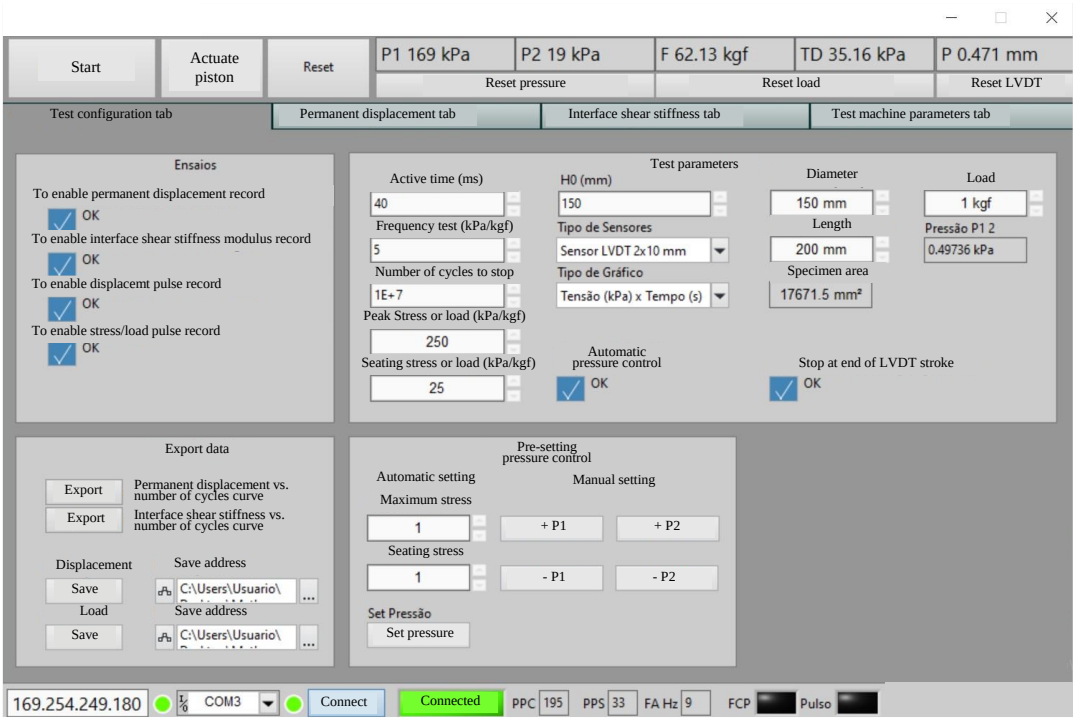

Figure 6.2 – Test configuration tab.

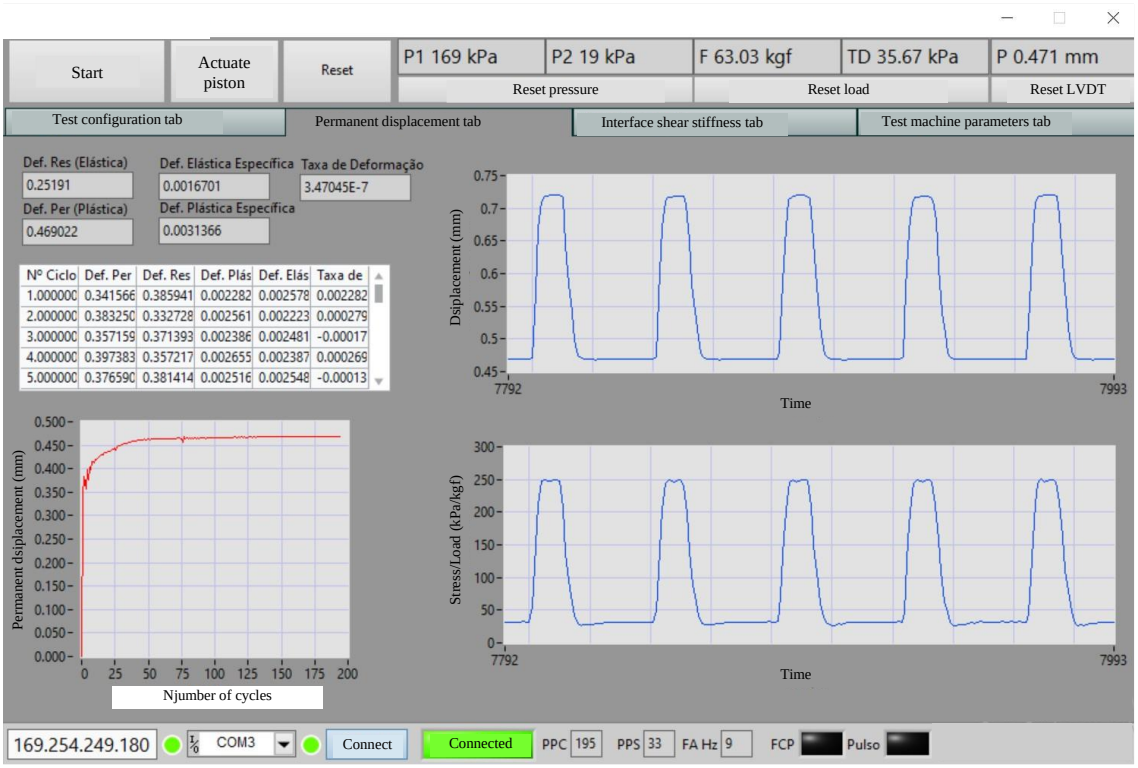

Figure 6.3 – Permanent displacement tab.

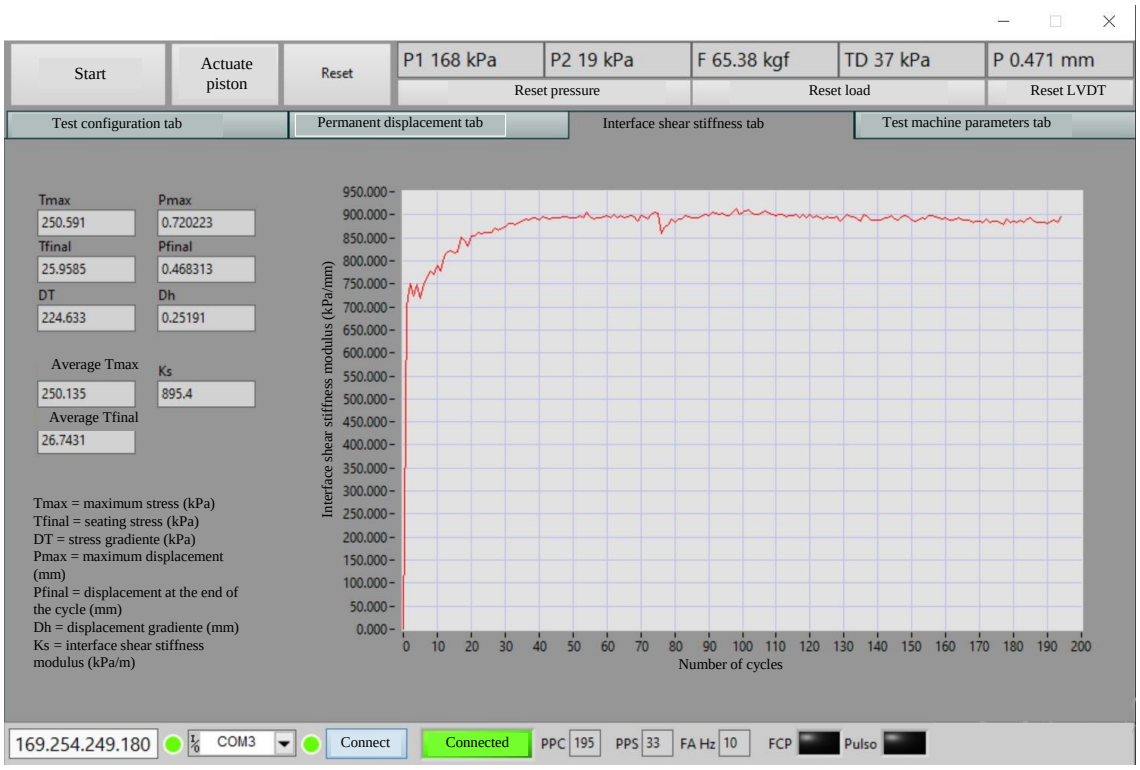

Figure 6.4 – Interface shear stiffness modulus tab.

6.2 Dynamic testing machine validation

The dynamic testing machine was validated checking the pulse load waveform, and the variability of the shear stress with different test configurations. Figure 6.5 shows the theoretical haversine waveform and the measured pulse waveform varying the test frequency (1 Hz, 5 Hz, and 10 Hz). It is noted that the measured pulse waveform is close to the haversine waveform and also respects the pulse duration of 0.1s, validating the proposed dynamic system relative to the waveform and pulse duration.

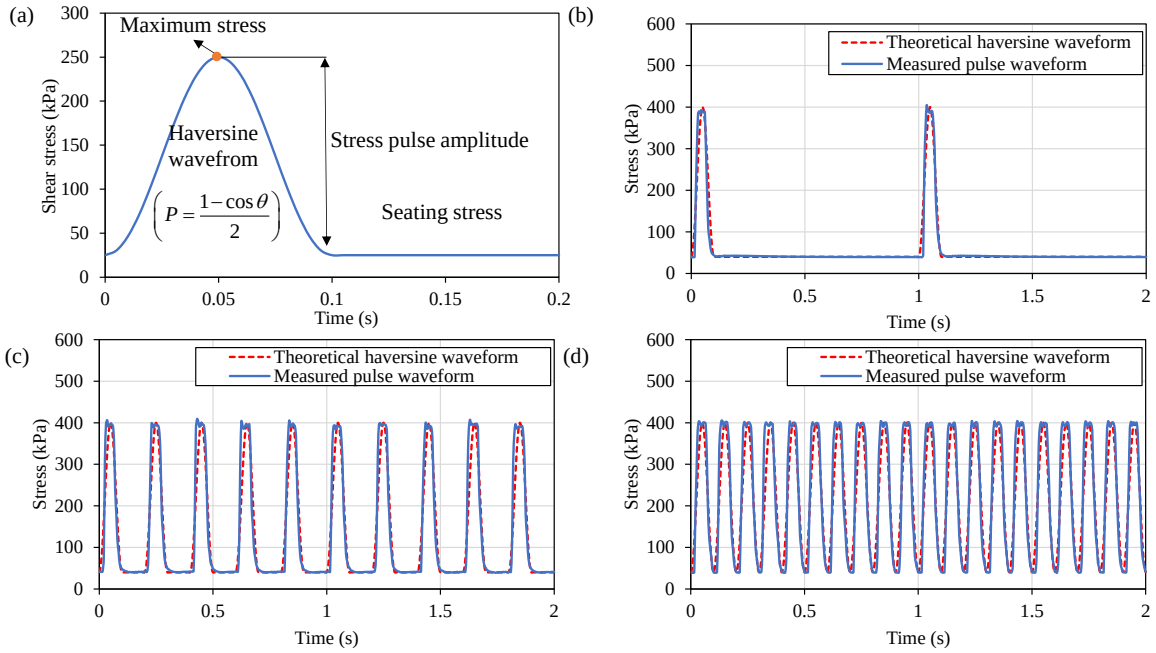

Figure 6.5 – Comparison between theoretical and measured pulse waveform: (a) haversine waveform, (b) 1 Hz, (c) 5 Hz, (d) 10 Hz.

To assess the variability of peak shear stress and pulse shear stress amplitude, dummy double-layered asphalt specimens were prepared and tested with varying peak shear stresses (200 kPa, 400 kPa, and 800 kPa) and seating shear stresses (10% of the peak shear stress). For each peak shear stress, the test frequency was also varied (1 Hz, 5 Hz, and 10 Hz). The tests were conducted until the failure of the asphalt specimens. Tables 6.1 present the coefficient of variation for each parameter for the different test configurations. As shown in Table 6.1, the highest coefficient of variation was 1.65%. Since there is no standard test method for the shear fatigue test, according to

DNIT ME 184 (2018) for dynamic creep test for asphalt mixtures, the coefficient of variation of peak stress should range between ± 2%. Thus, the dynamic testing machine developed in this study presented an acceptable coefficient of variation for different test conditions. As observed in Table 6.1, the dynamic testing machine developed in this study was not capable of performing dynamic tests with a peak shear stress of 800 kPa and a test frequency of 10 Hz due to the compressor air capacity.

Table 6.1 – Coefficient of variation for each parameter for the different test configurations.

Parameters	200 kPa			400 kPa			800 kPa		
	1 Hz	5 Hz	10 Hz	1 Hz	5 Hz	10 Hz	1 Hz	5 Hz	10 Hz
Peak stress	1.47%	0.86%	0.55%	0.66%	0.51%	0.41%	0.35%	0.42%	-
Pulse stress amplitude	1.65%	0.98%	0.66%	0.98%	0.61%	0.51%	0.40%	0.50%	-

6.3 Proposed test method and analysis procedures

6.3.1 Summary of the test method

The shear fatigue test for double-layered asphalt specimens follows a load-controlled approach, wherein vertical loads are repetitively applied in a haversine waveform. The application of the vertical load is parallel to the interface, specifically on the upper asphalt layer of the double-layered asphalt specimen. Subsequently, the resulting shear loads applied, and shear displacements are measured. For each cycle, the values of permanent shear displacements and the cyclic interface shear stiffness modulus are calculated. The test outcomes include the interface shear flow number, interface shear fatigue life, and cyclic interface shear stiffness modulus at failure.

6.3.2 Apparatus

6.3.2.1 Testing machine

The testing machine must be an electro-hydraulic or electro-pneumatic system capable of performing stress-controlled tests using a haversine waveform load pulse. It should have the

capacity to cover a wide range of load levels, rest periods, and test frequencies within the range of 1 to 10 Hz. Additionally, it should be capable of maintaining the selected load pulse until the specimen fails.

6.3.2.2 Loading device

The loading device must be capable of testing specimens with a diameter of 150 mm and heights up to 100 mm. It should consist of a stationary compartment and a movable compartment with adjustable gaps up to 5 mm. The movable compartment should be guided by two columns, positioned on either side of the specimen and equidistant from the loading axis. This design ensures minimal translational or rotational motion during specimen loading. The movable compartment must be sufficiently rigid to prevent excessive deflection. Additionally, the loading device should be equipped with LVDTs to measure shear displacement resulting from the movement of the movable compartment parallel to the interface.

6.3.3 Asphalt concrete specimens

The test specimen can be obtained from field coring or from laboratory-compacted specimen.. The shear fatigue testing shall be performed on a 150 mm ± 2 mm diameter specimen, consisting of two asphalt layers, each with a minimum thickness of 40 mm ± 2 mm. The axis parallel to the traffic direction shall be marked. This marking is required for applying loading parallel to the traffic direction.

6.3.4 Procedure

The procedure involves shear fatigue testing at a peak shear stress of 250 ± 5 kPa, with seating shear stress set at 10% of the peak shear stress. The testing parameters include a loading frequency of 5 Hz, a load duration of 0.1 s, and a rest period of 0.1 s at a temperature of 20 ± 1 ºC. This procedure was established based on prior studies in shear fatigue testing (D'Andrea and Tozzo, 2016; Miró et al., 2021; Romanoschi and Metcalf, 2001; Safavizadeh et al., 2022a; Tozzo et al., 2016, 2015, 2014b). Optionally, the test series can be conducted at different temperatures, peak

shear stress levels, or loading frequencies. However, in these alternative test scenarios, the load duration of 0.1 s should be maintained, while the rest period depends on the defined loading frequency.

The test specimen for the shear fatigue test shall undergo a minimum of 6 hours of conditioning at 20 ± 1 ºC before testing to ensure temperature uniformity. If there is not a temperature-controlled cabinet large enough to house the loading device, the test room temperature shall be controlled at 20 ± 1 ºC at the time of testing.

The test specimen must be placed horizontally, aligning the traffic direction parallel to the load application. The interface should be marked with white tape to facilitate easy alignment at the center of the 3 mm gap between the stationary and movable compartments of the loading device. The white tape should be fixed to the bottom asphalt layer, ensuring its upper boundary sits slightly below the interface. The bottom asphalt layer of the specimen was placed in the stationary compartment, while the upper asphalt layer was placed under the movable compartment for vertical loading, without the application of normal stress. Figure 6.6 shows the alignment and seating of the test specimen.

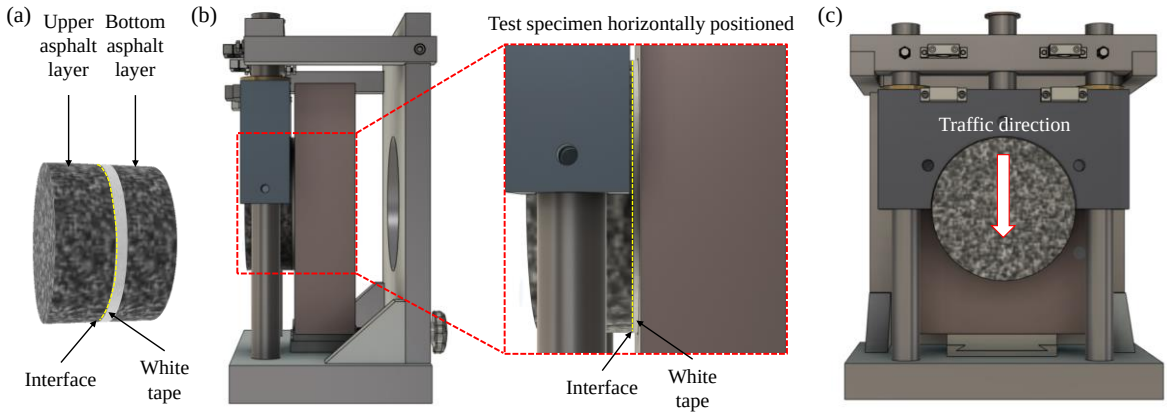

Figure 6.6 – Alignment and seating of the test specimen: (a) interface marking, (b) test specimen horizontally positioned, (c) traffic direction alignment.

A preconditioning stage shall be conducted to verify the correct accommodation of the test specimen in the loading device. This stage also aims to identify and address any issues with instrumentation or other aspects of the testing setup before the shear fatigue test begins. The pre-conditioning consists of applying the seating load for 60 seconds. At the end of the preconditioning the measurement of the LVDT should be reset and the shear fatigue test shall be conducted

according to the selected test parameters. The shear stress pulse shall be applied continuously through the entire test. The measured shear displacement and shear stress pulse applied shall be recorded. The test should be terminated after complete failure of the specimen or at 10 mm of shear displacement.

6.3.5 Calculation and interpretation of results

The following calculations at the end of each load cycle should be performed:

- Maximum shear stress (kPa):

$$\tau_{\max} = \frac{4 \times P_{\max}}{\pi \times D^2} \times 1000 \tag{6.1}$$

Where $\tau_{\max}$ is the maximum shear stress, $P_{\max}$ is the peak shear load (N), and D is the specimen diameter (mm).

- Seating shear stress (kPa):

$$\tau_s = \frac{4 \times P_s}{\pi \times D^2} \times 1000 \tag{6.2}$$

Where τ_p is the seating shear stress, P_s is the seating shear load (N), and D is the specimen diameter (mm).

- Shear stress amplitude (kPa):

$$\Delta\tau = \tau_{\max} - \tau_s \tag{6.3}$$

- Permanent shear displacement (mm):

$$u_{p,n} = \sum_{i=1}^{n} u_{e,n} - u_{0,n} \tag{6.4}$$

Where $u_{p,n}$ is permanent shear displacement at nth cycle, $u_{e,n}$ is the shear displacement at the end nth cycle (mm), and $u_{0,n}$ is initial shear displacement at nth cycle (mm).

- Shear displacement amplitude (mm):

$$\Delta u = u_{max} - u_0 \tag{6.5}$$

Where Δu is shear displacement amplitude, u_{max} is maximum shear displacement (mm), and u_0 is initial shear displacement of the shear displacement pulse (mm).

- Cyclic interface shear stiffness modulus (mm):

$$k_s = \frac{\Delta \tau}{\Delta u} \tag{6.6}$$

- Normalized cyclic interface shear stiffness modulus x normalized cycles:

$$k_s \times N = \frac{k_{s,n} \times N_n}{k_{s,0} \times N_0} \tag{6.7}$$

Where $k_s \times N$ is normalized cyclic interface shear stiffness modulus x normalized cycles shear displacement amplitude, $k_{s,n}$ is cyclic interface shear stiffness modulus at nth cycle, N_n is the cycle n, $k_{s,0}$ is the initial cyclic interface shear stiffness modulus, estimated at approximately 50 cycles, N_0 is the actual cycle number where initial cyclic interface shear stiffness modulus is estimated.

6.3.5.1 Result charts

After calculating the permanent shear displacement, the curve for permanent shear displacement versus the number of cycles can be plotted. Figure 6.7 illustrates a typical curve of permanent shear displacement versus the number of cycles. The permanent shear displacement rate can be obtained from the first derivative fitted model equation of the permanent shear displacement versus the number of cycles curve.

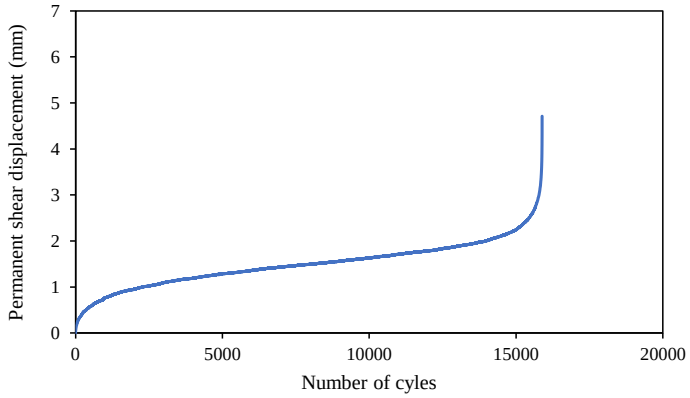

Figure 6.7 – Typical curve of permanent shear displacement versus the number of cycles.

According to AASHTO T 378 (2022), the Francken model is able to fit various shapes of permanent deformation curves. However, the Francken model is not able to fit the permanent shear displacement versus the number of cycles from shear fatigue tests. In this study, sixty experimental data from different shear fatigue test configurations were analyzed using Lab Fit software to find the fitted model equation for permanent shear displacement versus the number of cycles curve. To fit the experimental data curve, Lab Fit perform a nonlinear regression analysis using the least squared method and suggests ten fitted model equations based on a database containing 500 functions. The ten fitted model equations are ranked according to chi-square value. The curve fitting search was done considering four regression coefficient, same number presented in Francken model. The model equation that best fits for the sixty experimental data is given by Equation 6.8.

$$u_{pf,n} = \left(A \times N^{B}\right) \times \left(C - N\right)^{D} \tag{6.8}$$

Where $u_{pf,n}$ is the fitted permanent shear displacement at nth cycle (mm), N is the number of cycles, A, B, C, and D are the regression coefficients.

The permanent shear displacement rate in μm is given by Equation 6.9, which is obtained from the derivative of Equation 6.8 times 1000. Figure 6.8 presents the curves of permanent shear displacement, fitted permanent shear displacement, and permanent shear displacement rate versus number of cycles together.

$$\frac{du_{pf,n}}{dN} = \left(A \times \left(B \times N^{B-1}\left(C-N\right)^{D} - D \times N^{B}\left(C-N\right)^{D-1}\right)\right) \times 1000 \tag{6.9}$$

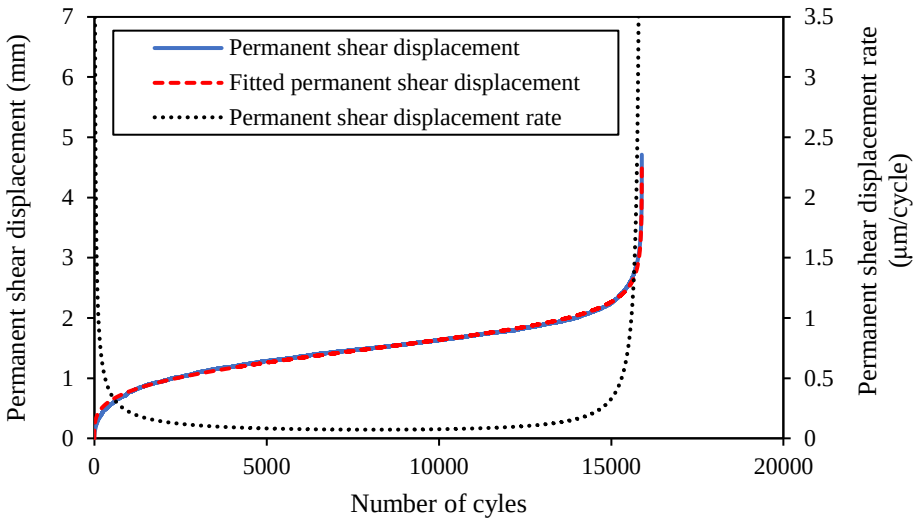

Figure 6.8 – Curves of permanent shear displacement, fitted permanent shear displacement, and permanent shear displacement rate versus number of cycles together.

After calculating the cyclic interface shear modulus and the normalized cyclic interface shear stiffness modulus x normalized cycles, both parameters can be plotted versus number of cycles. Figure 6.9 shows both parameters plotted versus number of cycles. As can be observed in Figure 6.9, the parameters relating to cyclic interface shear modulus are sensitive to the variation of the shear stress applied and shear displacement measured. For that reason, both curves can be fitted to interpret the experimental data. The first step is fit the normalized cyclic interface shear stiffness modulus x normalized cycles curve to the model presented by Equation 6.10. After the first step, the cyclic interface shear modulus can be fitted using the Equation 6.11.

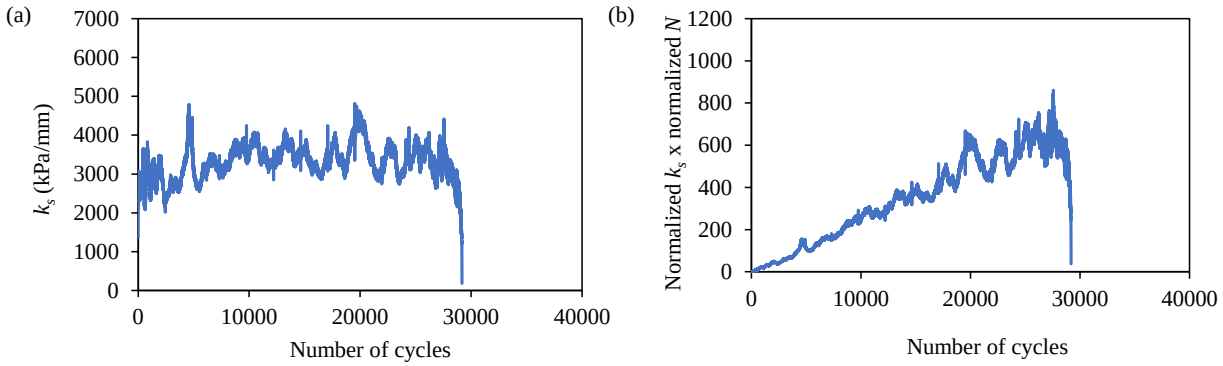

Figure 6.9 – Typical results related to cyclic interface shear stiffness modulus: (a) cyclic interface shear stiffness modulus versus number of cycles, (b) the normalized cyclic interface shear stiffness modulus x normalized cycles versus number of cycles.

$$\left(k_s \times N\right)_{f,n} = \left(A \times N^B\right) \times \left(C - N\right)^D \tag{6.10}$$

Where $(k_s \times N)_{f,n}$ is the fitted normalized cyclic interface shear stiffness modulus x normalized cycles at nth cycle, N is the number of cycles, A, B, C, and D are the regression coefficients.

$$k_{sf,n} = \frac{\left(\left(k_s \times N\right)_{f,n} \times k_{s,0} \times N_0\right)}{N_n} \tag{6.11}$$

Where $k_{sf,n}$ is fitted cyclic interface shear stiffness modulus at nth cycle, $(k_s \times N)_{f,n}$ is the fitted normalized cyclic interface shear stiffness modulus x normalized cycles at nth cycle obtained using Equation 6.10, N_n is the cycle n, $k_{s,0}$ is the initial cyclic interface shear stiffness modulus, estimated at approximately 50 cycles, N_0 is the actual cycle number where initial cyclic interface shear stiffness modulus is estimated.

Figure 6.10 shows the raw and fitted cyclic interface shear stiffness modulus and normalized cyclic interface shear stiffness modulus x normalized cycles versus number of cycles. The fitted cyclic interface shear stiffness modulus curve presents similar behavior compared to the curve presented by Tozzo et al. (2014b).

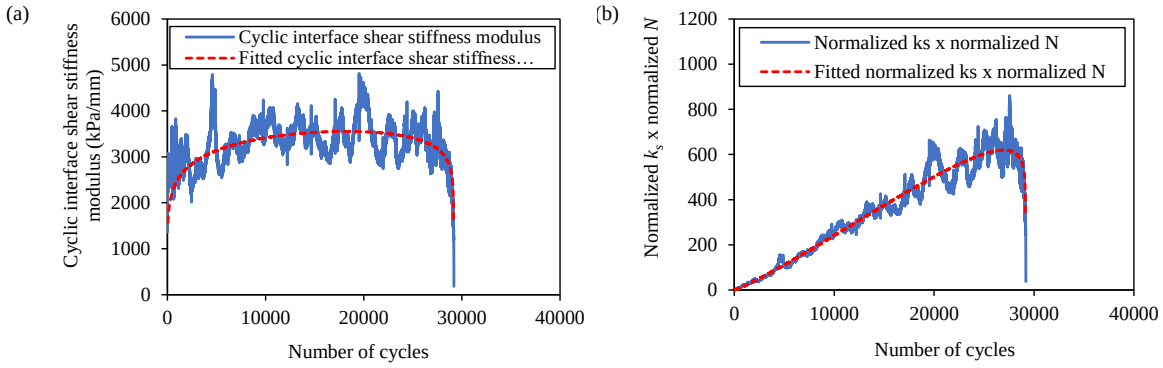

Figure 6.10 – (a) raw and fitted cyclic interface shear modulus curve, (b) raw and fitted normalized cyclic interface shear stiffness modulus x normalized cycles versus number of cycles.

6.3.5.2 Approaches to determine the failure point

Figure 6.11 presents the different approaches to determine the failure point. As depicted in Figure 6.11a, the permanent shear displacement curve exhibits three distinct stages (primary, secondary, and tertiary), as depicted in Figure 6.11a. During the primary stage, the permanent shear displacement experiences a rapid increase due to the initial interface adjustment. In the second stage, shear displacement grows gradually, displaying an approximately constant trend. This constancy is discernible by the inclination of the tangent line to the primary and tertiary stages. The tertiary reveals a very fast propagation of the failure mechanism, which is noted by the very fast increase in displacement.

In stress-controlled tests, the conventional method for determining the failure point is identifying the number of cycles corresponding to complete debonding ($N_{f,c}$) of the test specimen. However, in this scenario, the interface shear stiffness modulus (k_s) at complete debonding is comparatively lower than the k_s during the shear fatigue test (Figure 6.11c). An alternative approach for determining the failure point in dynamic tests involving asphalt specimens is the flow number, termed as the shear flow number (N_{sfn}) for shear fatigue tests. N_{sfn} is defined as the point where the permanent shear displacement rate reaches a minimum value (Figure 6.11a). Notably, as observed in Figure 6.11c, the corresponding k_s occurs before the test specimen reaches the peak value of k_s. The last recommended method to determine the failure point is the normalized cyclic interface shear stiffness modulus x normalized cycles approach. In this case, the number of cycles to failure ($N_{f,nks}$) coincides with the peak value of the normalized cyclic interface shear stiffness

modulus x normalized cycles curve, as illustrated in Figure 6.11b. This approach is proposed for determining the failure point in the tertiary stage. Moreover, this method offers a cyclic interface shear stiffness modulus that can be employed in future design methods to predict the bearing capacity of pavement structures ($k_{s,d}$), as $k_{s,d}$ occurs between the peak k_s and the k_s corresponding to complete debonding. For that reason, this study suggests employing the normalized cyclic interface shear stiffness modulus x normalized cycles to determine the failure point (N_f).

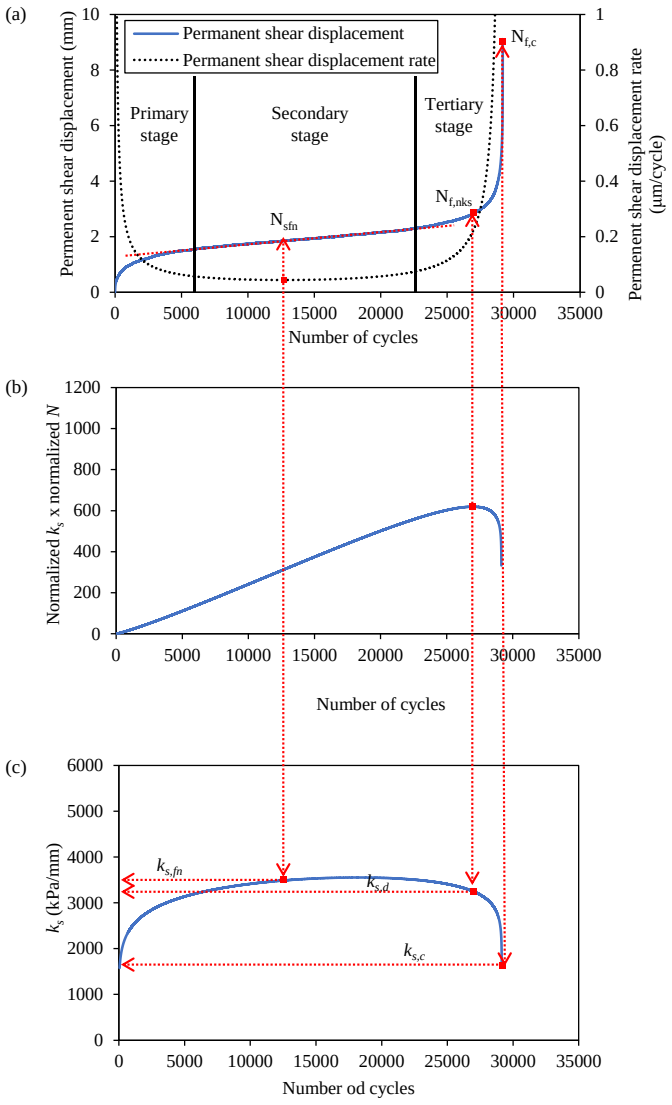

Figure 6.11 – Different approaches to determine the failure point: (a) shear flow number approach, (b) normalized cyclic interface shear stiffness modulus x normalized cycles approach, (c) design cyclic interface shear stiffness modulus.

6.3.6 Precision and Bias

The within-laboratory repeatability standard deviation of $N_{f,nks}$ has been determined to be 20%, based on one laboratory, three test replicates, and eighteen different types of test specimens. It is essential to investigate the between-laboratory reproducibility of the shear fatigue test. Consequently, it is not recommended to employ this proposed test method for the purpose of accepting or rejecting material purchases. Additionally, no information can be presented on the bias of this proposed method for measuring $N_{f,nks}$ because there is not an accepted reference value available.

6.4 Experimental program for shear fatigue tests

Table 6.2 presents the test program conducted regarding shear fatigue testing. The test program was designed to investigate the influence of different paving geosynthetics, tack coat rates, tack coat types, and test frequency on shear fatigue properties.

Table 6.2 – Experimental test program of the shear fatigue testing.

Type of investigation	Test	Geosynthetic	Tack coat	Tack coat rate (g/m^2)	Maximum shear stress (kPa)	Frequency (Hz)
Effect of different paving geosynthetics	1	Control	PG 58-16	600	250	5
	2	Pa-G-1	PG 58-16	600	250	5
	3	Pa-G-2	PG 58-16	600	250	5
	4	Pa-G-3	PG 58-16	600	250	5
	5	Pa-G-4	PG 58-16	600	250	5
	6	Pa-C-1	PG 58-16	600	250	5
	7	Pa-C-2	PG 58-16	600	250	5
	8	Pa-C-3	PG 58-16	600	250	5
	9	Pa-C-4	PG 58-16	600	250	5
	10	P-M	PG 58-16	600	250	5
Effect of the tack coat rate	11	Pa-G-2	PG 58-16	200	250	5
	12	Pa-C-1	PG 58-16	200	250	5
Effect of the tack coat type	13	Pa-G-2	CRS-1	600	250	5
	14	Pa-C-1	CRS-1	600	250	5
Effect of the test frequency	15	Pa-G-2	PG 58-16	600	250	1
	16	Pa-C-1	PG 58-16	600	250	1

CHAPTER 7. INTERFACE SHEAR BOND TEST RESULTS AND ANALYSIS

7.1 Interface shear stress-displacement curve

Figure 7.1 illustrates the typical interface shear stress-displacement curve for a test series involving nine paving geosynthetics, a control interface, two types of tack coats, and three tack coat rates. The peak shear stress and post-peak shear stress loss are influenced by the paving geosynthetic type, tack coat type, and rate, as depicted in Figure 7.1.

In Figure 7.1a, the interface shear stress-displacement curve for the control test specimens reveals a higher peak shear stress compared to specimens with paving geosynthetic. However, control test specimens with CRS-1 at a residual rate of 600 g/m² or PG 58-16 applied at a rate of 400 g/m² exhibit peak shear stress values similar to those specimens with paving geosynthetics, depending on the paving geosynthetic type, tack coat type, and rate. This behavior aligns with findings reported by Canestrari et al. (2018), Correia et al. (2023), and Correia and Mugayar (2021). The observed behavior can be attributed to the geosynthetic's properties, enhancing its bond with surrounding asphalt layers, as well its interaction with tack coat type and rate. In the control test specimen, there is a rapid overall decrease in shear stress following the peak.

Regarding post-peak shear stress behavior for the test specimens with paving geosynthetic, it was observed different trends. Pa-G-1 (Figure 7.1b), Pa-G-2 (Figure 7.1c), Pa-G-3 (Figure 7.1d) showed a comparatively faster decrease in shear stress following the peak when CRS-1 was applied then PG 58-16 was applied. It can be attributed to the presence of openings in the paving geogrids. Pa-G-4 (Figure 7.1e) and Pa-C-3 (Figure 7.1h) presented a slower decrease in shear stress following the peak independent of the tack coat type and rate when compared to the others paving geosynthetic. This behavior can be due to the presence of the fabric strips crossing the geogrid mesh in Pa-G-4, and the comparatively thicker fabric backing in Pa-C-3. Pa-C-2 (Figure 7.1g) and Pa-C-4 (Figure 7.1i) that are similar products presented different post-peak shear stress behavior, which can be attributed to the differences in geogrid composition and mesh. Overall, it can be observed that the interface shear stress-displacement curve shape depends on the geosynthetic's properties and its interaction with tack coat type and rate.

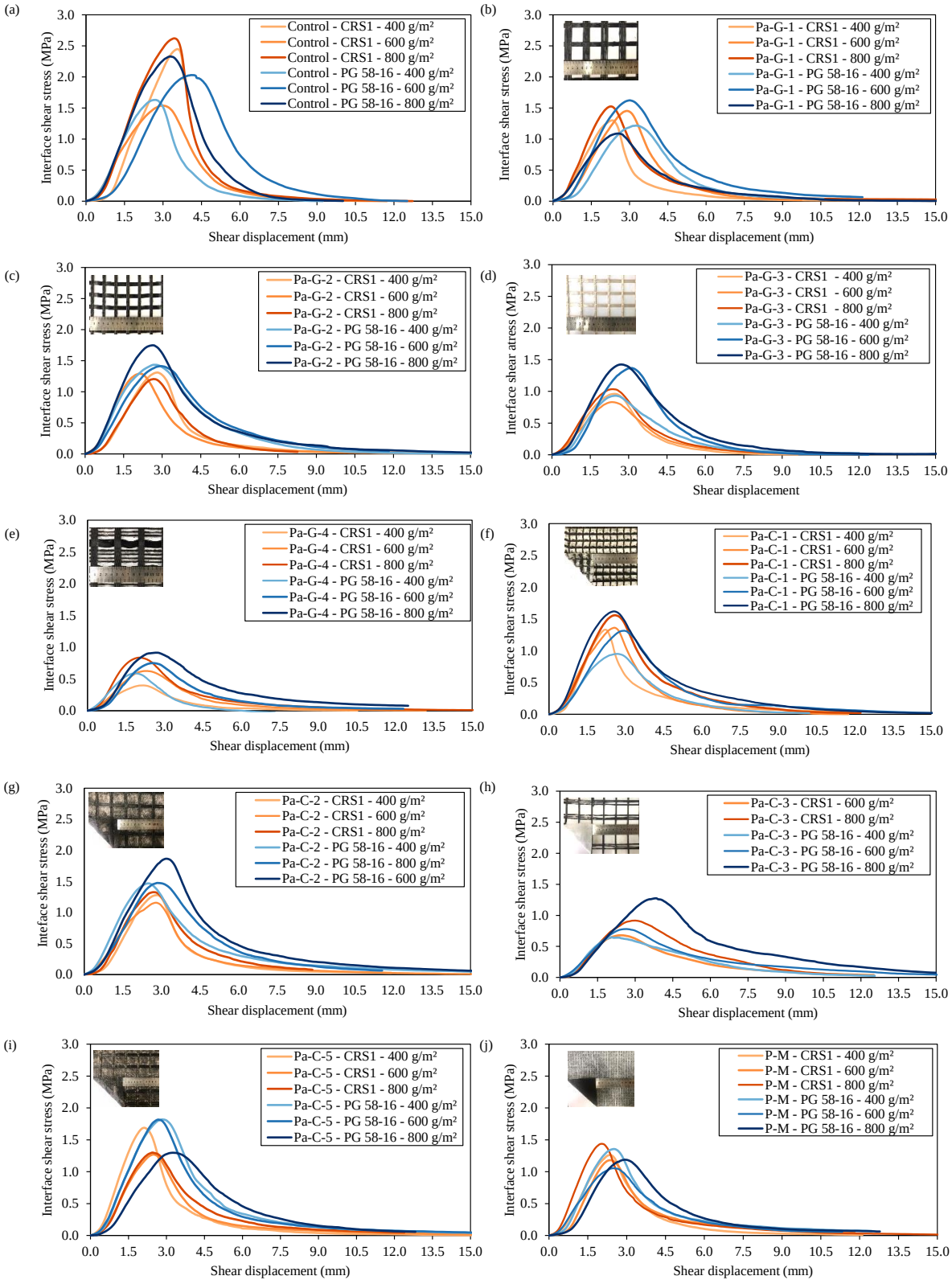

Figure 7.1 - Typical interface shear stress-displacement for different interface conditions: (a) control, (b) Pa-G-1, (c) Pa-G-2, (d) Pa-G-3, (e) Pa-G-4, (f) Pa-C-1, (g) Pa-C-2, (h) Pa-C-3, (i) Pa-C-4, and (j) P-M.

7.2 Results and analysis of Interface shear strength

Figure 7.2 presents average *ISS* values obtained through testing nine different paving geosynthetics, considering two tack coat types, and employing three tack coat rates in this study. The figure also displays one standard deviation in the test results for each combination of tested specimens. As shown in Figure 7.2, the overall *ISS* values ranged from 0 to 1.86 MPa. Similar *ISS* value ranges (0 to 2.0 MPa) have been reported in other studies evaluating asphalt layers with paving geosynthetic (Ante, 2016; Canestrari et al., 2018, 2022b; Correia et al., 2023; Correia and Mugayar, 2021; Elsing and Leite-Gembus, 2019; Fonseca, 2015; Leite-Gembus and Elsing, 2020; Sudarsanan et al., 2018b; Walubita et al., 2018, 2019).

Figure 7.2 also shows the minimum *ISS* required (ISS_{min}) of 0.56 MPa, corresponding to 10 kN, for field core of asphalt layers with paving geosynthetic and 150 mm diameter, as specified by the German Working FGVS 770 (2013). However, Canestrari et al. (2022b) suggest a 50% increase in the minimum *ISS* value required when using laboratory-produced specimens. The ISS_{min} for the present study corresponds to 0.84 MPa as also shown in Figure 7.2.

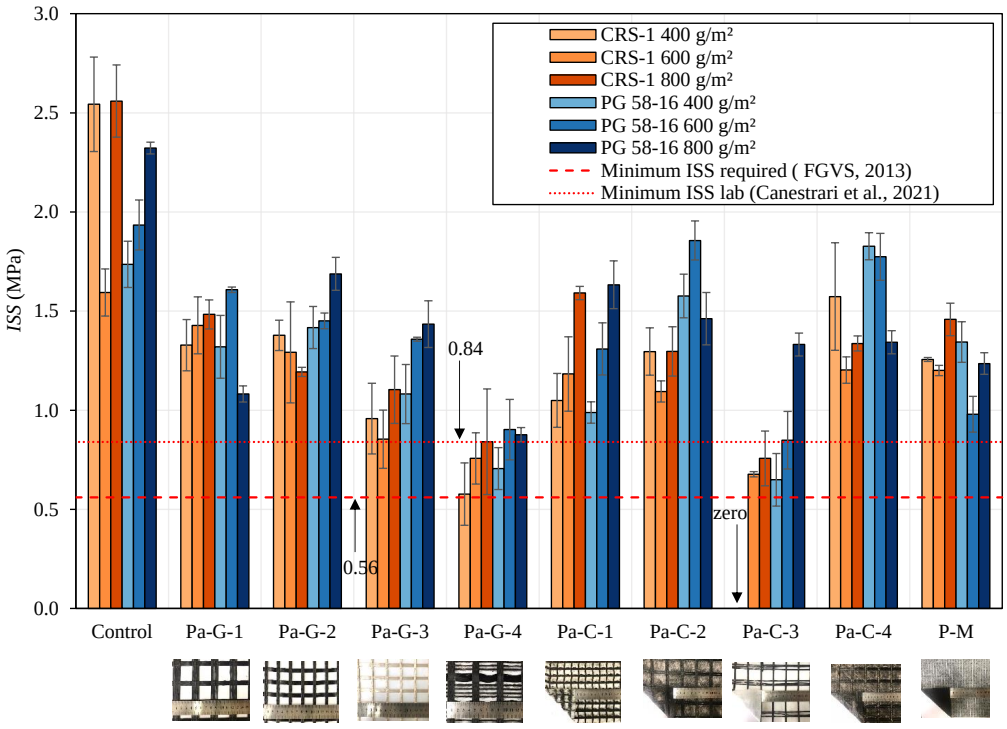

Figure 7.2 – Average *ISS* values for different variables in asphalt layers with paving geosynthetic.

To determine whether the average ISS_{meas} values exceed ISS_{min}, Equation 5.4 was employed using the ϕ values from Table 5.2. Results indicate that Pa-G-1, Pa-G-2, Pa-C-2, and Pa-C-4 consistently met the ISS_{min} of 0.84 MPa for all tack coat types and rates. Pa-C-1 met the ISS_{min} only when the tack coat rate was equal to or greater than 600 g/m². Similarly, Pa-G-3 met the ISS_{min} when using PG 58-16 as the tack coat at rates equal to or greater than 600 g/m². Additionally, Pa-C-3 met the ISS_{min} when PG 58-16 was applied at a rate of 800 g/m². P-M met the ISS_{min} for all tack coat rates except when PG 58-16 was applied at a rate of 600 g/m². However, Pa-G-4 failed to meet the ISS_{min} under any condition.

Analyzing the results depicted in Figure 7.2 for various paving geosynthetics, adopting PG 58-16 demonstrated superior *ISS* performance. However, the effectiveness of PG 58-16 varied depending on the paving geosynthetic and the applied tack coat rates. Different *ISS* trends were observed across various combinations: (i) *ISS* increased with tack coat rate for combinations of CRS-1 with Pa-G-1, Pa-G-4, Pa-C-1, Pa-C-3, and PG 58-16 with Pa-G-2, Pa-G-3, Pa-C-1, and Pa-C-3; (ii) *ISS* increased up to 600 g/m² tack coat rate, then decreased for combinations of PG 58-16 with Pa-G-1, Pa-G-4, and Pa-C-2; (iii) *ISS* initially decreased with tack coat rate up to 600 g/m², then increased for CRS-1 with Pa-G-3, Pa-C-2, Pa-C-4, and P-M; (iv) For CRS-1 with Pa-G-2 and PG 58-16 with Pa-C-4, an increase in tack coat rate led to a reduction in *ISS*. These trends were also noted by Correia et al. (2022) and Sagnol et al. (2019), suggesting diverse interactions between geosynthetic properties and tack coat type and rate.

7.3 Evaluation of the significant factors for interface shear strength

The findings depicted in Figure 7.2 indicate that the ISS is significantly influenced by various factors, including geosynthetic properties, tack coat type, and rate. Furthermore, different geosynthetic properties may interact differently with tack coat type and rate. To analyze the impact of these factors (i.e., paving geosynthetic type, tack coat type, and rate) on the dependent variable (*ISS*) and explore potential interactions, it is advisable to conduct a multi-factorial analysis of variance (ANOVA). The significance of each factor can be determined using the Fisher-statistic, also referred to as the F-statistic, in an ANOVA test with a significance level (α) of 0.05. If the p-value resulting from Fisher's test is significantly less than 0.05, it indicates a substantial effect of the factor or interactions (Montgomery and Runger, 2014).

A multi-factorial ANOVA analysis was conducted to evaluate the influence of paving geosynthetic type, tack coat type, tack coat rate, and their interactions on *ISS*, with a significance level (α) set at 0.05. Table 7.1 presents the results of multi-factorial ANOVA analysis for paving geosynthetic type, tack coat type, tack coat rate and interactions. The results exhibit p-values below 0.05, signifying a significant impact of paving geosynthetic type, tack coat type, tack coat rate, and their interactions on *ISS*. Additionally, the findings validate the interaction between various geosynthetic properties and tack coat type and rate.

Table 7.1 – ANOVA for paving geosynthetic type, tack coat type, tack coat rate and interactions.

Factor	Sum of squares	Degrees of freedom	Mean square	F-statistic	*p*-value
Tack coat rate	0.491	2	0.2456	15.11	< .001
Tack coat type	1.415	1	1.4151	87.1	< .001
Paving geosynthetic type	12.246	7	1.7494	107.67	< .001
Tack coat type x Tack coat rate	0.25	2	0.1252	7.71	< .001
Paving geosynthetic type x Tack coat rate	2.584	14	0.1846	11.36	< .001
Paving geosynthetic type x Tack coat type	1.355	7	0.1936	11.91	< .001
Paving geosynthetic type x Tack coat type x Tack coat rate	1.398	14	0.0999	6.15	< .001
Errors	1.56	96	0.0162		

Since all factors significantly impact *ISS*, it is crucial to quantify the specific impact of each factor and their interactions. The effect size of the ANOVA can be measured using Omega squared (ω), explaining the variance contributed by each factor and interaction in the *ISS*. Further insights on ω^2 can be found in Güllü's (2014). Table 7.2 displays the ω^2 values for each factor and their interactions, along with the interpretation of the effect level based on Keppel and Wickens (2004). As depicted in Table 7.2, the paving geosynthetic type exhibited the highest ω^2 value, surpassing those for tack coat type, tack coat rate, and interactions. This underscores a substantial impact on *ISS*. The effect sizes for tack coat type and rate were medium and small, respectively, while the interaction effects varied from small to medium. These findings suggest that distinct geosynthetic properties significantly influence *ISS*.

Table 7.2 – Effect size of factors and interactions.

Factor	ω^2	Effect size
Tack coat rate	0.02	Small
Tack coat type	0.07	Medium
Paving geosynthetic type	0.57	Large
Tack coat type x Tack coat rate	0.01	Small
Paving geosynthetic type x Tack coat rate	0.11	Medium
Paving geosynthetic type x Tack coat type	0.06	Medium
Paving geosynthetic type x Tack coat type x Tack coat rate	0.06	Medium

The ANOVA results reveal moderate interactions between the type of paving geosynthetic and other factors. To fully understand the impact of various geosynthetic properties on *ISS*, it's imperative to assess each interface condition (including tack coat type and rate) individually. Given the significant influence of different geosynthetic properties on *ISS*, a multiple linear regression analysis can be performed. This analysis aims to uncover potential relationships between geosynthetic properties and *ISS*, enabling independent prediction of *ISS* for each interface condition (tack coat type and rate).

7.4 Multiple linear regression analysis for Interface shear strength

Multiple Linear Regression (MLR) analysis serves as a valuable tool for exploring the connections between ISS and various factors, including geogrid mesh area, thickness, and the presence of bitumen coating on paving geosynthetics. It aids in predicting ISS based on the properties of geosynthetics. Previous research has utilized MLR to forecast the mechanical behavior of geosynthetic systems. For example, MLR has been employed to predict the bearing capacity of geosynthetic-reinforced sand beds (Latha et al., 2013), the shear strength of soil-geosynthetic interfaces (Debnath and Dey, 2017), and the rutting resistance of asphalt layers with paving geosynthetic (Qadir et al., 2021). In this study, MLR analysis was conducted on *ISS*, taking

into account geosynthetic properties and interface conditions such as tack coat type and rate. Ultimately, empirical models were proposed to predict the ISS of asphalt-geosynthetic interfaces based on geosynthetic properties. An MLR model defines the relationship between a dependent variable (y) and multiple predictor variables (x) as follows:

$$y = \beta_0 + \beta_1 x_1 + \beta_2 x_2 + ... + \beta_k x_k \pm \varepsilon \quad (7.1)$$

Where, y is the dependent variable; $\beta_0, \beta_1, \ldots, \beta_k$ are the regression coefficients; $x_0, x_1, \ldots, x_k$ are the predictor variables; k is the number of significant predictor variables and the ε is the error. This model defines a hyperplane in a k-dimensional space of the independent variables. The parameter β_0 represents the intercept of the hyperplane with dependent variable axis.

Validation of a MLR model should be carried out to confirm its assumptions. Table 7.3 outlines the MLR model assumptions, their consequences upon violation, and the procedures employed in this study to verify each assumption.

Table 7.3 – Assumptions of MLR model.

Assumption	Impact of assumption violation	Check test
The errors have a normal distribution (normality).	p-value of F-test is not valid	Shapiro-Wilk (Shapiro and Wilk, 1965)
The independent variables are not highly correlated.	Multicollinearity	Variance Inflation Factor (VIF) (Montgomery and Runger, 2014)
The errors do not correlate with the independent variables (homoscedasticity)	Heteroskedasticity	Breusch-Pagan (Breusch and Pagan, 1979)
The errors are randomized and independent. (Absence of correlation)	Autocorrelation of errors	Durbin-Watson (Durbin and Watson, 1950, 1951, in Kotz and Johnson, 1992)

The Shapiro-Wilk, Breusch-Pagan, and Durbin-Watson tests provide p-values to assess adherence to assumptions of normality, homoscedasticity, and absence of autocorrelation. When comparing these p-values with α (set at 0.05), if the p-value exceeds α, there is insufficient evidence to reject the null hypothesis, validating the assumptions. To prevent multicollinearity, Variance Inflation Factors (VIF) should remain below 4 (Montgomery and Runger, 2014). Violations of MLR model assumptions may indicate errors in functional form or omission of relevant independent variables, potentially impacting regression coefficients significantly.

The Fisher's test (Equation 7.2) evaluates the overall model significance and determines if a linear relationship exists between the dependent variable and at least one independent variable.

This involves testing the null hypothesis ($\beta_0 = \beta_1 = \ldots = \beta_k = 0$) against the alternative hypothesis ($\beta_i \neq 0$), for at least one i. The Fisher's test, expressed as follows, serves as the statistical procedure for this hypothesis.

$$F = \frac{SS_{\text{mod}}/k}{SS_{error}/(n-p)} = \frac{MS_{\text{mod}}}{MS_{error}} \tag{7.2}$$

Where, SS_{mod} is the regression or model sum of squares; SS_{error} is the sum of squares due to error; k is the number of significant parameters in the model; n is the size sample; p equals $k - 1$; MS_{mod} is the model mean square; and MS_{error} is the mean square due to error.

Upon conducting Fisher's test, a p-value is generated. If this value falls below 0.05, it indicates rejection of the null hypothesis, suggesting a linear relationship between the overall model and at least one independent variable. Conversely, if the p-value exceeds 0.05, it fails to reject the null hypothesis, implying no linear association with any independent variables.

Following the evaluation of the Multiple Linear Regression (MLR) model's significance, further tests are required to assess the significance of partial regression coefficients. Thus, t-tests (Equation 7.3) should be conducted to test the null hypothesis ($\beta_i = 0$) against the alternative hypothesis ($\beta_i \neq 0$). If the resulting p-value is less than 0.05, the null hypothesis is rejected, and the partial coefficient persists within the model. Conversely, if the p-value exceeds 0.05, the null hypothesis regarding the partial coefficient cannot be rejected, thus warranting its exclusion from the MLR model.

$$t = \frac{\beta_i}{SE(\beta_i)} \tag{7.3}$$

Where, $SE(\beta_i)$ is the standard error of the partial coefficient β_i.

Assessing the adequacy of fit for a Multiple Linear Regression (MLR) model typically involves evaluating the coefficient of multiple determination, denoted as R^2. This metric quantifies the proportion of variability in the dependent variable accounted for by the independent variables within a linear regression fit (Montgomery and Runger, 2014). R^2 values range between 0 and 1, where higher scores indicate a greater extent of explained variability in the dependent variable by

the regression model, signifying a stronger fit. Conversely, an R^2 approaching 0 suggests a lack of relationship between the independent and dependent variables (Latha et al., 2013). The coefficient of multiple determination is calculated as follows:

$$R^2 = \frac{SS_{\text{mod}}}{SS_{tot}} \tag{7.4}$$

Where, SS_{mod} is the sum of the square due to model regression; and SS_{tot} is the total sum of the square.

In accordance with the recommendations of Montgomery and Runger (2014), theoretical aspects were considered to select geosynthetic properties for developing the Multiple Linear Regression (MLR) model, such as through-hole bonding and adhesion mechanisms. Simplicity in quantifying geosynthetic properties was also a key factor in selecting the model's geosynthetic properties. Consequently, the geogrid mesh area (A_{gm}), thickness of the paving geosynthetic (T_g), thickness of the fabric backing (T_{fb}), and the presence or absence of a bitumen coating (B_c) were chosen as predictor variables for the model. Descriptions of these variables can be found in Table 7.4. The overall MLR model, predicting *ISS* in MPa, is as follows:

$$ISS = \beta_0 + \beta_1 \cdot A_{gm} + \beta_2 \cdot T_g + \beta_3 \cdot T_{fb} + \beta_4 \cdot B_c \tag{7.5}$$

Table 7.4 – Description of predictor variables for *ISS*.

Predictor variable	Unit	Description
A_{gm}	mm²	geogrid mesh area*
T_g	mm	thickness of the paving geosynthetic
T_{fb}	mm	thickness of the fabric backing**
B_c	-	Dichotomous variable (0 or 1) indicating the presence or not of a bitumen coating***

* In the presence of a heavyweight fabric backing or strips of fabric crossing the geogrid mesh area, A_{gm} should equal 0.

** In the absence of fabric backing, T_{fb} should equal 0.

*** In the absence of bituminous coating, B_c should equal 0.

7.5 Analysis of the Multiple linear regression models for Interface shear strength

The relationships between various geosynthetic properties and *ISS* were assessed for each combination of tack coat type and rate through MLR analysis. Initially, attempts were made to establish MLR models considering the *ISS* results of all paving geosynthetics selected in this study. However, when the *ISS* results of P-M were included in the MLR model development, the p-value for the overall model, independent of the interface condition, exceeded 0.05. This result indicates that it was not possible to establish MLR models to predict *ISS* considering P-M properties. For that reason, the development of MLR models was carried out, considering all paving geosynthetics except P-M. Thus, predictive models for ISS based on geosynthetic properties were derived for each combination. Table 7.5 outlines the MLR models established and the assumption checks.

Table 7.5 – Statistics of the MLR models established for interface shear strength and the assumption checks.

Model	R^2	F	Degrees of freedom		Overall model	Shapiro-Wilk test	Breusch-Pagan test	Durbin-Watson test
			Regression	Error	*p*-value	*p*-value	*p*-value	*p*-value
CRS-1 400 g/m²	0.91	45.4	4	19	<.001	0.810	0.422	0.126
CRS-1 600 g/m²	0.74	13.7	4	19	<.001	0.836	0.163	0.134
CRS-1 800 g/m²	0.73	17.6	3	20	<.001	0.729	0.118	0.060
PG 58-16 400 g/m²	0.89	33.5	4	16	<.001	0.842	0.174	0.060
PG 58-16 600 g/m²	0.87	45.5	3	20	<.001	0.953	0.28	0.088

As outlined in Table 7.5, predictive models were established for various combinations of tack coat type and rate, with the exception of PG 58-16 applied at 800 g/m². In this specific instance, efforts to incorporate different geosynthetic properties resulted in an R^2 of no more than 30%, indicating poor predictability of *ISS* based on the properties of geosynthetics. It is evident that the behavior of *ISS* is predominantly influenced by the higher application rate of PG 58-16 when applied at 800 g/m².

All other predictive models for different tack coat types and rates fulfilled the assumptions of normality, homoscedasticity, and absence of autocorrelation. Additionally, these models displayed a linear relationship with at least one geosynthetic property, with p-values under 0.05 derived from the overall model. The goodness of fit, measured by R^2, ranged from 73% to 91%,

elucidating the linear variation in *ISS* based on the chosen geosynthetic properties in each MLR model.

It's notable that an increase in tack coat rate resulted in a decrease in R^2, indicating diminished variability explained by geosynthetic properties on ISS. Furthermore, the R^2 analysis of the MLR models substantiated the findings of the effect size analysis, underscoring the significant impact of paving geosynthetic type on *ISS*.

The results of significance tests for each regression coefficient concerning geosynthetic properties, selected for each combination of tack coat type and rate, are provided in Table 7.6. It's important to mention that only the individual regression coefficients rejecting the null hypothesis (p-value < 0.05) were retained in the MLR models. In other words, only the geosynthetic properties that significantly linearly influenced ISS were incorporated. Moreover, the selected geosynthetic properties met the assumption of no multicollinearity, with the Variance Inflation Factor (VIF) being less than 4.

The results presented in Table 7.6 demonstrate the linear impact of three geosynthetic properties on the *ISS* as predictor variables: geogrid mesh area, geosynthetic thickness, and fabric backing thickness. Additionally, depending on the tack coat type and rate, the presence or absence of bitumen coating also plays a role. Previous studies have noted that geosynthetic tensile stiffness influences interface shear strength (Sudarsanan et al., 2018b; Walubita et al., 2018). Initially, this study considered incorporating tensile stiffness into the prediction models. However, MLR analysis revealed no significant effect on interface shear strength. Correia and Mugayar (2021) highlighted a negative correlation between geogrid coverage area (defined as the ratio of the area covered by grid yarns to the total specimen cross-sectional area) and *ISS*. Therefore, geogrid coverage area was included in the MLR models. The analysis indicated a negative correlation with interface shear strength, and it emerged as a significant factor. However, including it in the model caused multicollinearity with geogrid mesh area and autocorrelation with fabric backing thickness. Consequently, a decision was made to select predictor variables, considering multicollinearity. Geogrid mesh area and fabric backing thickness, being easily obtainable and commonly used by designers, remained in the models, while geogrid coverage area was disregarded.

Table 7.6 – Significance test results for each regression coefficient selected to predict *ISS*.

Model	Predictor variable	Regression coefficient	Standardized regression coefficient	*p*-value	VIF
CRS-1 400 g/m²	Intercept	-0.495		0.130	
	A_{gm}	0.000647	0.555	<.001	1.12
	T_{fb}	-0.827	-0.720	<.001	1.51
	T_g	0.753	0.310	0.001	1.33
	B_c	0.248	0.489	0.034	1.04
CRS-1 600 g/m²	Intercept	-0.425		0.158	
	A_{gm}	0.000200	0.306	0.022	1.12
	T_{fb}	-0.485	-0.753	<.001	1.51
	T_g	0.786	0.577	<.001	1.33
	B_c	0.320	1.129	0.005	1.04
CRS-1 800 g/m²	Intercept	-0.311		0.303	
	A_{gm}	0.000225	0.326	0.016	1.11
	T_{fb}	-0.504	-0.741	<.001	1.45
	T_g	0.978	0.679	<.001	1.33
PG 58-16 400 g/m²	Intercept	-0.182		0.618	
	A_{gm}	0.000694	0.739	<.001	1.31
	T_{fb}	-0.372	-0.414	0.004	2.228
	T_g	0.611	0.285	0.021	1.87
	B_c	0.241	0.571	0.03	1.1
PG 58-16 600 g/m²	Intercept	0.573		0.029	
	A_{gm}	0.00068	0.813	<.001	1.11
	T_{fb}	-0.266	-0.323	0.003	1.45
	T_g	0.349	0.200	0.042	1.33

The regression coefficients in Table 7.6 reveal the impact of selected geosynthetic properties on *ISS*. Positive coefficients imply that increasing predictor variable values result in increased *ISS*, while negative coefficients indicate a decrease in *ISS* with increasing predictor variable values. Specifically, geogrid mesh area, geosynthetic thickness, and the presence of

bitumen coating positively correlate with *ISS*. Otherwise, the thickness of the fabric backing shows a negative correlation with *ISS.*

The positive correlation with geogrid mesh area is explained by the THB mechanism (Sudarsanan et al., 2018b). This mechanism involves increased asphalt-to-asphalt contact with a larger geogrid mesh area, facilitating effective interlocking among HMA aggregates for higher bond strength. Figure 7.3 illustrates geogrid mesh area causing interlocking of HMA aggregates.

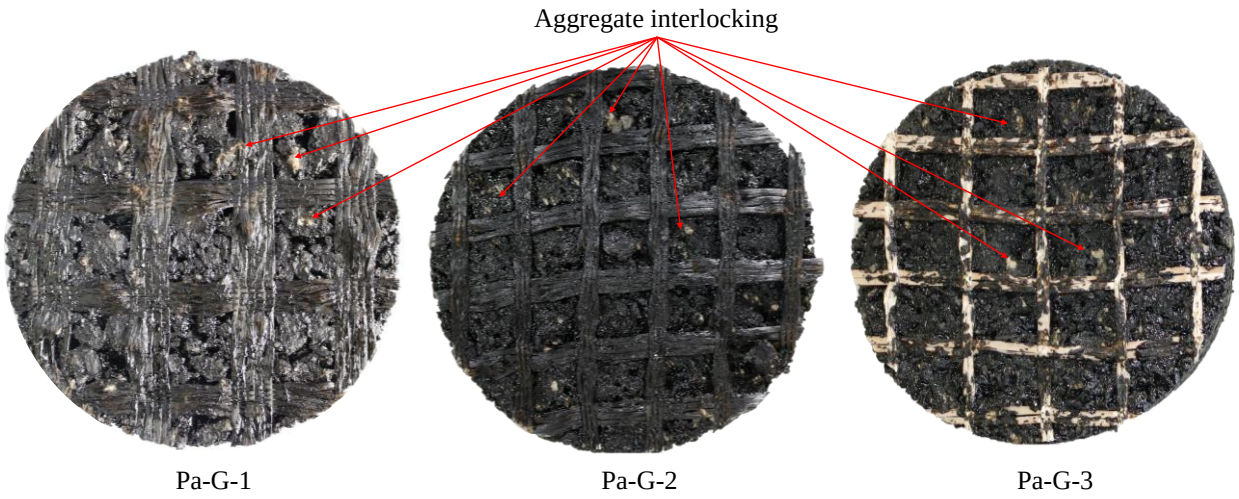

Figure 7.3 – Geogrid mesh area causing interlocking of HMA aggregates.

The increase in geosynthetic thickness shows a positive correlation with *ISS*, which is attributed to the embedding of geogrid ribs into the asphalt layer. Figure 7.4 illustrates the effect of geogrid ribs. Additionally, the presence of bitumen coating enhances bonding between the paving geosynthetic and upper asphalt layer, further positively influencing *ISS*. However, when CRS-1 was applied at 800 g/m² and PG 58-16 at 600 g/m², the impact of bitumen coating on *ISS* became insignificant. Figure 7.5 illustrates the effect of the presence and absence of bitumen coating. Figure 7.5b illustrates the comparison of tack coat impregnation of Pa-G-3 with PG 58-16 at a rate of 400 and 600 g/m². In Figure 7.5b, with PG 58-16 at 600 g/m², the geogrid without bitumen coating is almost entirely covered by the tack coat.

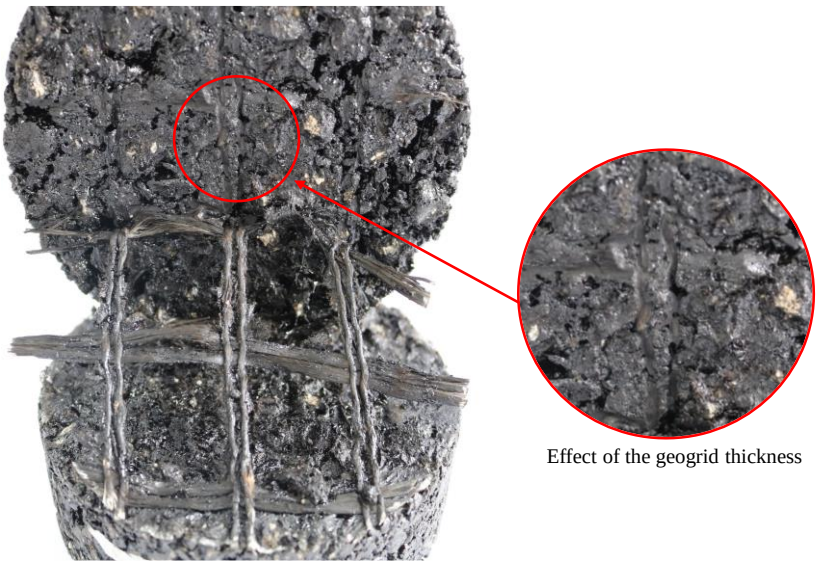

Figure 7.4 – Effect of the geogrid thickness.

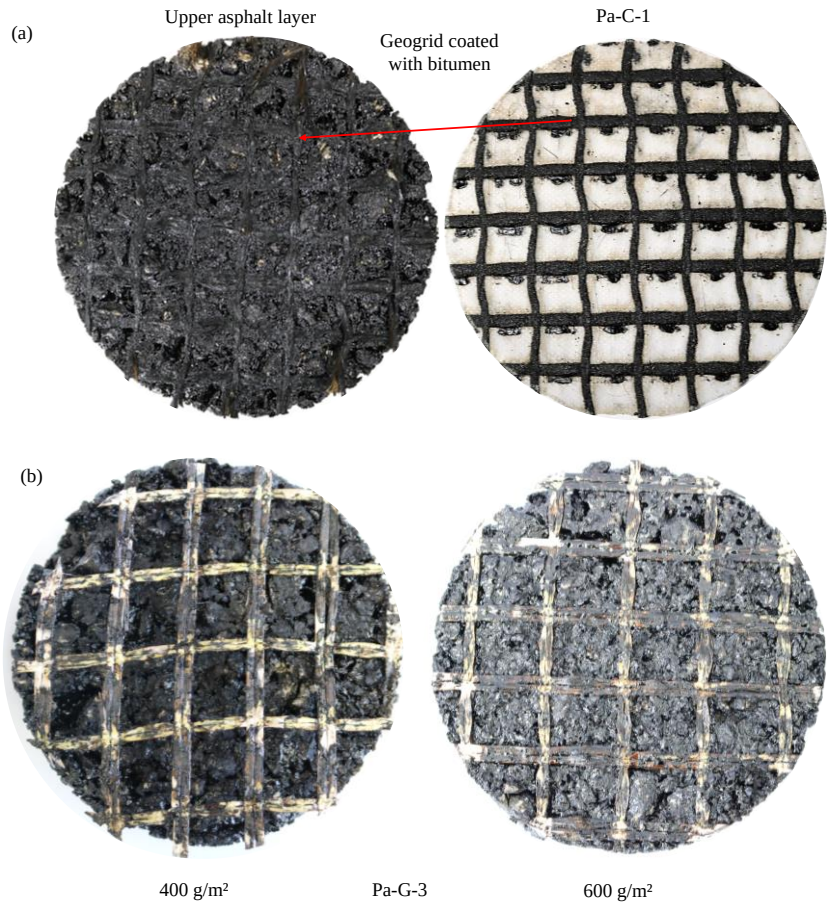

Figure 7.5. Effect of the presence and absence of bitumen coating: (a) geogrid coated with bitumen attached to upper asphalt layer, (b) comparison of tack coat impregnation of paving geogrid with different tack coat rates.

The negative effect of fabric backing thickness is explained by reduced asphalt-to-asphalt contact, impairing the THB mechanism. Figure 7.6a illustrates that a thin fabric backing, when saturated with tack coat, facilitates the adhesion mechanism. In contrast, Figure 7.6b shows that increasing fabric backing thickness requires more tack coat for complete saturation, impairing the THB mechanism and resulting in lower *ISS*.

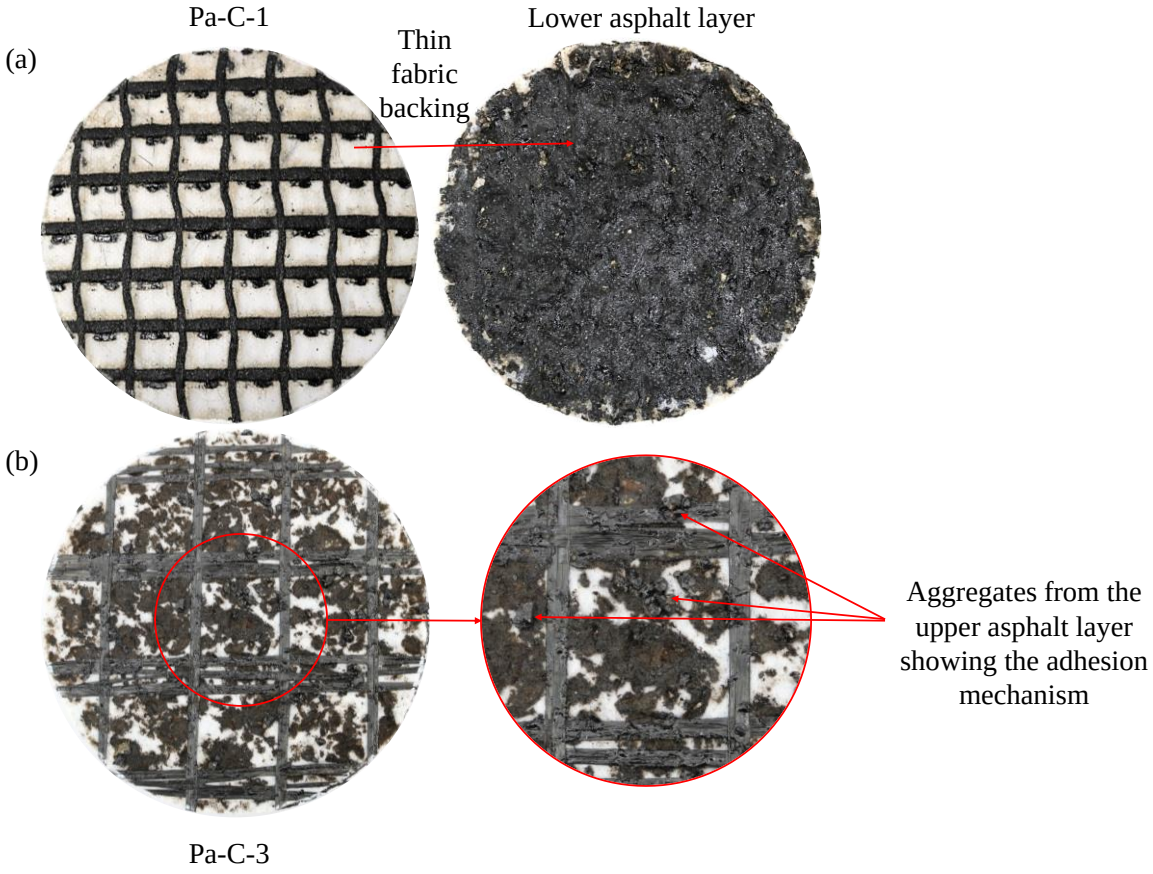

Figure 7.6 – Effect of fabric backing thickness: (a) detached fabric backing saturated with tack coat facilitating adhesion mechanism, (b) Thick fabric backing with lower tack coat saturation impairing THB mechanism.

In Table 7.6, it is evident that regression coefficient values vary for each combination of tack coat type and rate. This variability arises from the interaction between geosynthetic properties and tack coat characteristics. Because predictor variables are measured in diverse units, direct comparison of coefficient magnitudes cannot adequately gauge their impact on the *ISS*. Therefore, standardized regression coefficients were computed to enable a more precise assessment of each predictor variable's influence on the *ISS*.

As indicated by the standardized regression coefficients in Table 7.6, when emulsion was applied, the fabric backing thickness emerged as the geosynthetic property that most significantly affected the *ISS* for all tack coat rates. However, when PG 58-16 was applied, the effect of fabric backing thickness was not particularly significant, likely due to its impregnation by PG 58-16, which enhanced the adhesion mechanism and mitigated the negative impact of fabric backing thickness.

Regarding geogrid mesh area, its effect on *ISS* was observed to diminish further when CRS-1 was applied compared to when PG 58-16 was applied. This suggests that the effect of geogrid mesh area is related to the tack type. The presence of openings in the paving geogrid leads to direct asphalt-to-asphalt contact, and when PG 58-16 is present between the asphalt layers, it amplifies the impact of geogrid mesh area.

7.6 Verification of the MLR models and prediction of Interface shear strength

To evaluate the effectiveness of the MLR models, models incorporating CRS-1 as a tack coat type were verified, cross-referencing experimental findings from studies by Correia and Mugayar (2021) and Correia et al. (2023). Both studies evaluated similar paving geosynthetics, tack coat types, and rates. Unlike the laboratory-prepared specimens used in developing the *ISS* prediction models ($ISS_{l\text{-}predicted}$), the results obtained by Correia and Mugayar (2021) and Correia et al. (2023) were based on field-extracted specimens. To adjust the *ISS* prediction for field conditions, as recommended by Canestrari et al. (2022b), which suggests a 50% increase in *ISS* for laboratory-prepared specimens compared to field-extracted cores. Thus, it was determined the *ISS* prediction for field conditions ($ISS_{f\text{-}predicted}$) accordingly:

$$ISS_{f-predicted} = \frac{ISS_{l-predicted}}{1.5} \tag{7.6}$$

Figure 7.7 displays a scatterplot comparing *ISS* values predicted and measured in this study alongside those from by Correia and Mugayar (2021) and Correia et al. (2023). These investigations focused on specimens treated with emulsion as a tack coat at rates of 400, 600, and 800 g/m². The results obtained in the current study, along with those from Correia et al. (2023),

indicate that all *ISS* values fall within the 95% confidence level regardless of the emulsion application rate. However, in Correia and Mugayar's (2021) study, some *ISS* values exceed the 95% confidence level when emulsion is applied at rates of 600 g/m² (Figure 7.7b) or 800 g/m² (Figure 7.7c). Notably, while Correia and Mugayar (2021) assumed a smooth lower asphalt layer under the paving geosynthetic, both the current study and Correia et al. (2023) considered the surface to be rough.

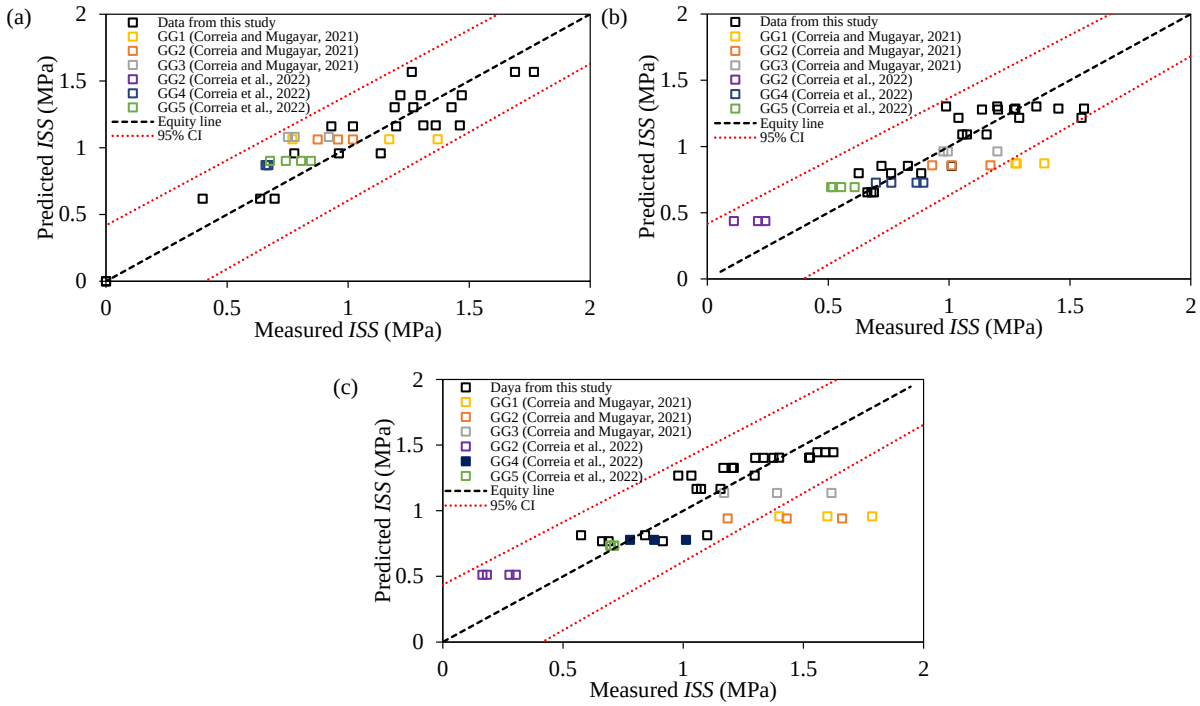

Figure 7.7 – Comparison between measured and predicted ISS values for: (a) CRS-1 at 400 g/m²; (b) CRS-1 at 600 g/m²; and (c) CRS-1 at 800 g/m².

A noteworthy study conducted by Canestrari et al. (2022b) indicated a 50% increase in *ISS* for laboratory-prepared specimens compared to field-extracted cores. These specimens were evaluated at interfaces using emulsion at a residual bitumen rate of 330 g/m². In this context, the *ISS* values from Correia and Mugayar (2021) outside the 95% confidence level limits underlies the potential influence of surface macrotexture and tack coat rate on the ISS relationship between laboratory-prepared and field-extracted specimens. The MLR models' predictions for CRS-1 demonstrate good alignment with measured *ISS* for both types of specimens, particularly when accounting for a rough surface on the asphalt layer where the paving geosynthetic is applied.

In Figure 7.8, the minimum predicted *ISS* necessary to meet the required minimum *ISS* for laboratory-prepared specimens is presented. This prediction is derived from the 95% confidence interval limits of the mean of new observations, with 3 replicates considered for both CRS-1 and PG 58-16. For CRS-1, the minimum predicted *ISS* is 1.11 MPa, while for PG 58-16, it is 1.17 MPa. These values are significant for manufacturers and designers in determining the geosynthetic properties needed to achieve the minimum required *ISS* for their specific applications.

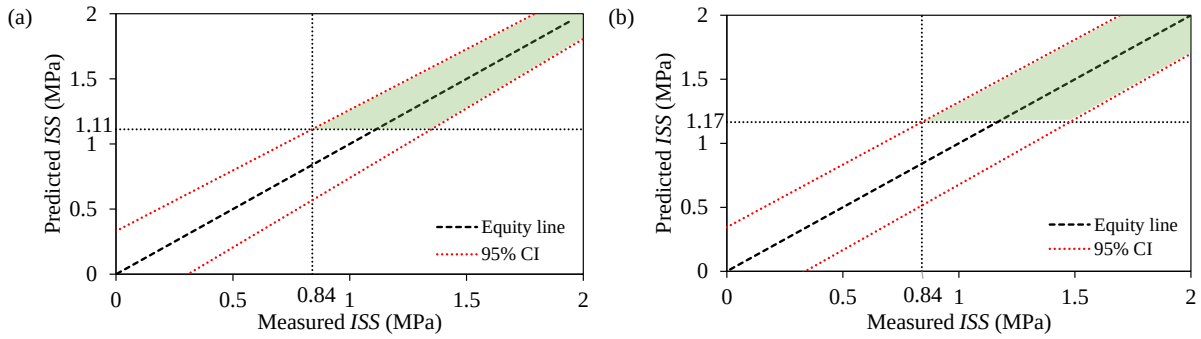

Figure 7.8 – Minimum predicted *ISS* to meet minimum *ISS* required for laboratory-prepared specimens: (a) CRS-1; and (b) PG58-16.

7.7 Prediction of interface shear stiffness modulus based on interface shear strength

Yang and Li (2021) emphasize the significance of the interface shear stiffness modulus as a key variable for comprehending the behavior of interface bonding up to the point of failure. Consequently, several authors have employed it to evaluate the impact of varying bonding levels on the stress-strain distribution of pavement (Ortiz-Ripoll et al., 2020; Ozer et al., 2012; Ragni et al., 2021; Romanoschi e Metcalf, 2001; Uzan et al., 1978). Figure 7.9 illustrates the correlation between *k* and *ISS*, along with the prediction of *k* based on *ISS*. Figure 7.9 also shows the coefficient of determination and Pearson coefficient *r*. R^2 explains the variability in *k* due the *ISS*. The coefficient *r* measures the level of correlation between *k* and *ISS*. As depicted in Figure 7.9, the coefficient r ranged from 0.83 to 0.95, indicating a consistently high to very high positive correlation between *k* and *ISS*, as per Taylor (1990) classification. Additionally, R^2 values ranged approximately from 70% to 90%, signifying that at least 70% of the variability in *k* can be accounted for by the *ISS*. In Figure 7.9, another observed aspect is that, for the same value of ISS, combinations involving CRS-1 exhibited higher values of k compared to those involving PG 58-

16. This difference is attributed to the lower viscosity of CRS-1 compared to PG 58-16, resulting in a lower shear displacement at failure in the CRS-1 combination than in the PG 58-16 combination. This indicates a relatively fragile behavior in the CRS-1 combinations.

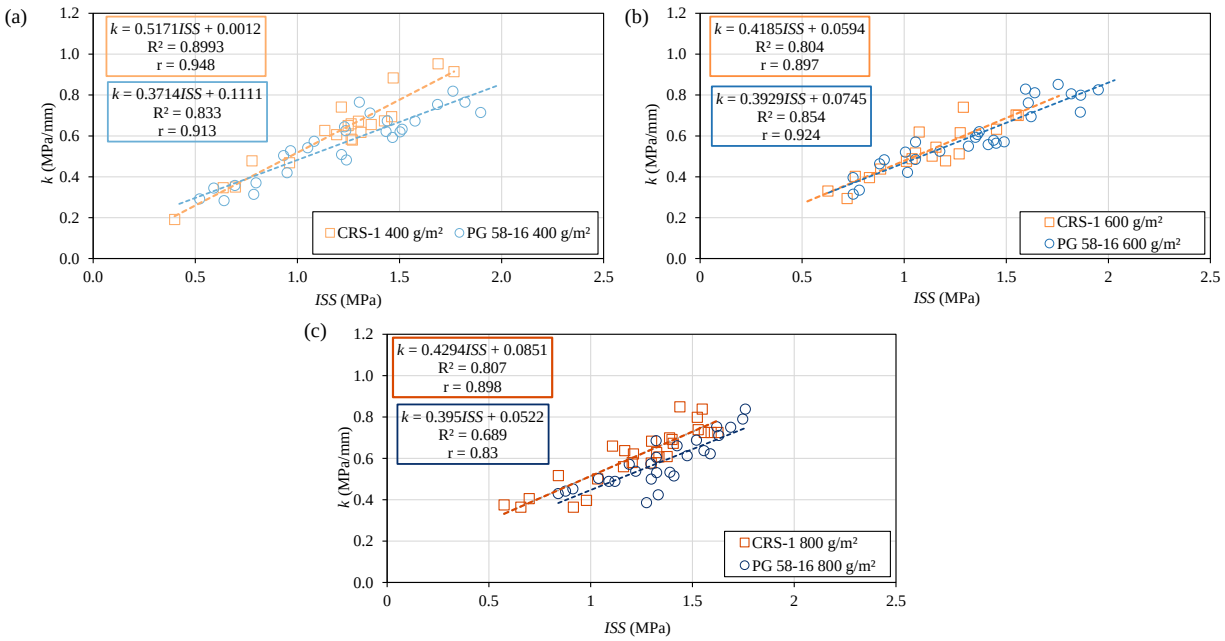

Figure 7.9 – Prediction of interface shear stiffness modulus based on interface shear strength for each interface condition: (a) CRS-1 and PG 58-16 at a rate of 400 g/m², (b) CRS-1 and PG 58-16 at a rate of 600 g/m², (c) CRS-1 and PG 58-16 at a rate of 800 g/m².

Table 7.7 presents the slope coefficient (a) and the intercept (b) from the linear equation for each interface condition along with the minimum k (k_{min}) required to meet the ISS_{min} of 0.84 MPa. The slope explains how *k* changes for every unit increase in *ISS*, on average, in each interface condition. The intercept describes *k* when *ISS* equal zero for each interface condition. The slopes ranged from 0.37 to 0.52, implying sensitivity to *ISS* variations due to changes in interface conditions. Similarly, the intercept ranged from 0.001 to 0.111 MPa/mm, indicating the effect of interface conditions on *k* itself. Regarding k_{min}, it varied between 0.38 and 0.45 MPa/mm. Therefore, the k_{min} ensuring ISS_{min} equal to or greater than 0.84 MPa is 0.45 MPa/mm.

Table 7.7 – Regression coefficients and minimum interface shear stiffness modulus values.

Tack coat type	Tack coat rate (g/m²)	a	b	k_{min} (MPa/mm)
CRS-1	400	0.517	0.001	0.44
PG 58-16		0.371	0.111	0.42
CRS-1	600	0.419	0.059	0.41
PG 58-16		0.393	0.075	0.41
CRS-1	800	0.429	0.085	0.45
PG 58-16		0.395	0.052	0.38

CHAPTER 8. SHEAR FATIGUE ANALYSIS

8.1 Effect of tack coat type on shear fatigue

Figure 8.1 illustrates the typical curves of permanent shear displacement versus the number of cycles for different combinations of paving geosynthetic and tack coat types. As depicted in Figure 8.1, the choice of tack coat influences the behavior of the permanent shear displacement curve, as evident from the differing slopes during the linear stage. This indicates that using CRS-1 as a tack coat results in an increased permanent shear displacement rate, consequently leading to premature failure when compared to the use of PG 58-16 as a tack coat. This behavior can be attributed to the higher viscosity of PG 58-16 when compared to CRS-1. In addition, it also can be observed that the use of Pa-G-2 results in an increased permanent shear displacement rate, independent of the tack coat type. This behavior indicates that the higher bitumen coating content in Pa-C-1 contributes to reducing the permanent shear displacement rate when compared to Pa-G-2.

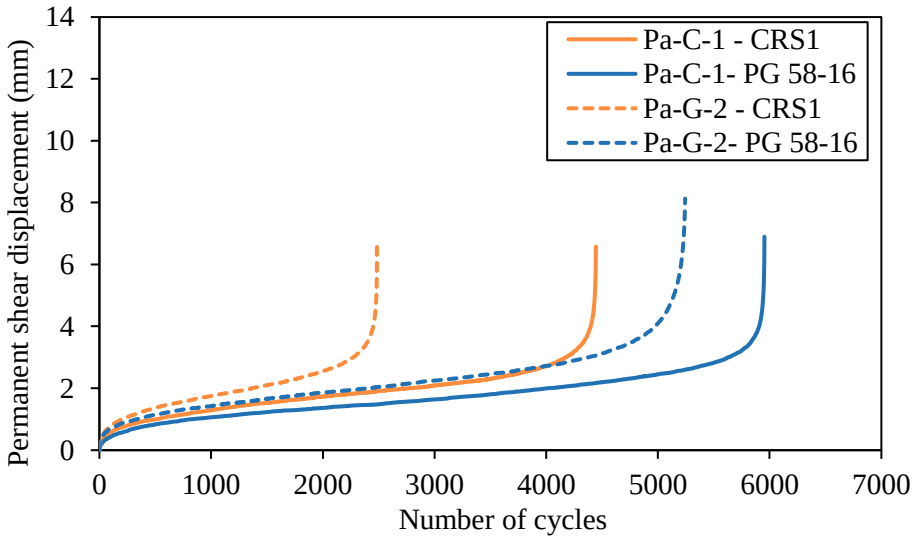

Figure 8.1 – Typical curves of permanent shear displacement versus the number of cycles for different combinations of paving geosynthetic and tack coat types.

Figure 8.2 shows the averages values of shear fatigue life (N_f) and cyclic interface shear stiffness modulus ($k_{s,d}$), along with one standard deviation, for different combinations of paving

geosynthetic and tack coat type. Figure 8.2a demonstrates the impact of tack coat type on N_f. For Pa-G-2 and Pa-C-1, the use of PG 58-16 as a tack coat increased N_f compared to CRS-1. Additionally, the influence of paving geosynthetic type on N_f is evident, as Pa-C-1 exhibited higher N_f than Pa-G-2 regardless of the applied tack coat. Figure 8.2b shows that different types of geosynthetic and tack coat do not affect $k_{s,d}$. Regardless of the type of paving geosynthetic or tack coat, similar values for $k_{s,d}$ are observed.

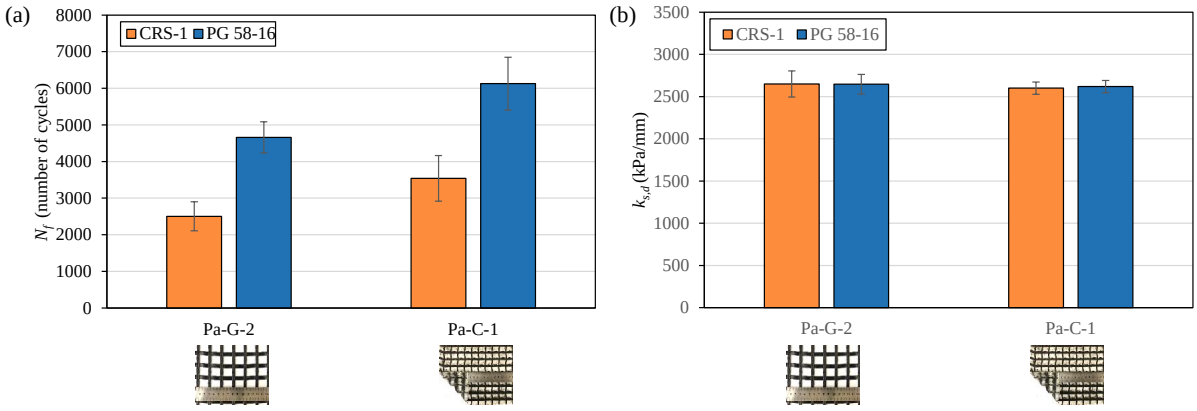

Figure 8.2 Shear fatigue parameters for different types of geosynthetic and tack coat: (a) N_f, (b) $k_{s,d}$.

To confirm the statistical significance of the effects of different types of paving geosynthetics and tack coat on shear fatigue parameters, a two-way ANOVA was conducted. This analysis assists in understanding how two categorical independent variables (paving geosynthetic type and tack coat type) and any potential interactions between them impact a continuous dependent variable (N_f or $k_{s,d}$). The two-way ANOVA reveals statistically significant differences in the averages of the dependent variable across various levels of both independent variables. This is determined by comparing the p-value to the significance level of 0.05. A p-value less than 0.05 indicates a significant effect of the independent variable on the dependent variable. Table 8.1 presents the results of the two-way ANOVA for shear fatigue parameters, considering the factors of paving geosynthetic type and tack coat type. The results from the two-way ANOVA are considered valid since they satisfy the assumptions of normality (Shapiro-Wilk's p-value greater than 0.05) and homoscedasticity (Levene's p-value greater than 0.05).

Table 8.1 – Two-way ANOVA for shear fatigue parameters results considering the paving geosynthetic type and tack coat type.

Shear fatigue parameters	Factors	Sum of squares	Degrees of freedom	Mean square	F	p-value	ω^2	Shapiro-Wilk p-value	Levene p-value
N_f	Paving geosynthetic type	5.22E+06	1	5.22E+06	15.89	0.003	0.176	0.767	0.565
	Tack coat type	1.87E+07	1	1.87E+07	57.10	<.001	0.664		
	Paving geosynthetic type × Tack coat type	1.53E+06	1	1.53E+06	0.47	0.51	-		
	Error	3.28E+06	10	3.28E+05	-	-	-		
$k_{s,d}$	Paving geosynthetic type	4.54E+03	1	4.54E+03	0.2088	0.658	-	0.091	0.913
	Tack coat type	2.89E+02	1	2.89E+02	0.0133	0.91	-		
	Paving geosynthetic type × Tack coat type	4.42E+02	1	4.42E+02	0.0203	0.889	-		
	Error	2.17E+05	10	2.17E+04	-	-	-		

As indicated in Table 8.1, the results of the two-way ANOVA demonstrate a significant effect of both paving geosynthetic type and tack coat type on N_f, with a p-value less than 0.05. However, there is no interaction observed between these two factors, as evidenced by a p-value greater than 0.05. Given that both factors significantly affect N_f, it is crucial to quantify the specific effect of each factor. The effect size of the ANOVA can be measured using Omega squared (ω^2), explaining the variance contributed by each factor. Table 8.1 displays the ω^2 values corresponding to each factor. According to Keppel and Wickens (2004), an ω^2 exceeding 0.15 signifies a large effect. Consequently, as depicted in Table 8.1, both paving geosynthetic type and tack coat type demonstrate a large effect on N_f. Concerning $k_{s,d}$, the results of the two-way ANOVA confirm that there is no significant effect of both paving geosynthetic type and tack coat type on $k_{s,d}$.

8.2 Effect of tack coat rate on shear fatigue properties

Figure 8.3 depicts typical curves of permanent shear displacement versus the number of cycles for different combinations of paving geosynthetic and tack coat rates. As shown in Figure 8.3, tack coat rates influence the behavior of the permanent shear displacement curve, depending on the type of geosynthetic. For Pa-G-2, an increase in the tack coat rate did not change the behavior of the primary and secondary stages. However, the tertiary stage started early when PG 58-16 was

applied at a rate of 200 g/m², leading to premature failure compared to the interface condition with PG 58-16 applied at a rate of 600 g/m². This indicates that an increase in the tack coat rate provides more bonding, prolonging the secondary stage. The same behavior was observed for Pa-C-1 and Pa-G-2 with PG 58-16 at a rate of 200 g/m², suggesting that the higher bitumen coating content in Pa-C-1 provides more bonding, also prolonging the secondary stage. Regarding the effect of the tack coat rate when Pa-C-1 was used, it is observed that an increase to 600 g/m² results in a decreased permanent shear displacement rate, consequently prolonging the number of cycles to failure compared to a tack coat rate of 200 g/m². This can be explained by the bitumen retention capacity of Pa-C-1, which is 423 g/m². The tack coat rate of 600 g/m², saturated with bitumen Pa-C-1, enhances the adhesion mechanism, resulting in a comparatively smaller permanent shear displacement rate.

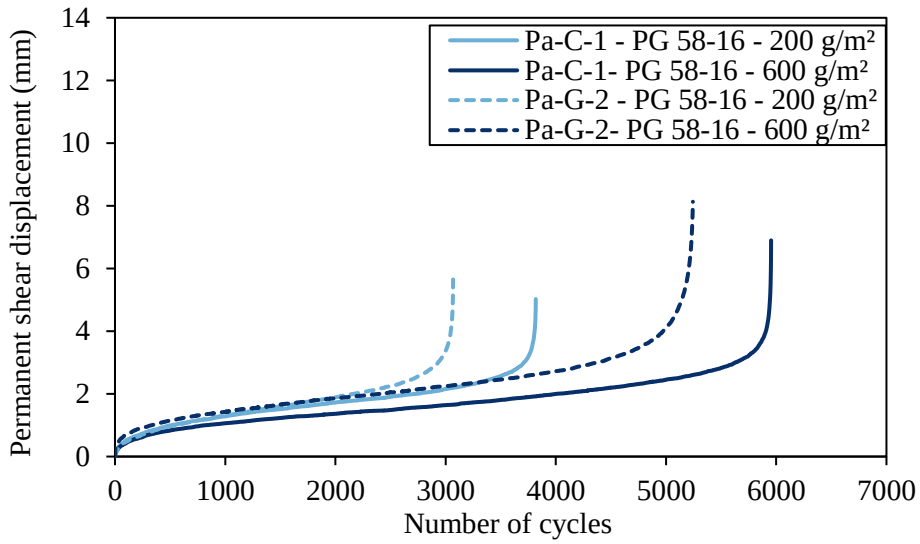

Figure 8.3 – Typical curves of permanent shear displacement versus the number of cycles for different combinations of paving geosynthetic and tack coat rate.

Figure 8.4 shows the averages of N_f and $k_{s,d}$, along with one standard deviation, for different combinations of paving geosynthetic and tack coat rate. Figure 8.4a demonstrates the impact of tack coat rate on N_f. For Pa-G-2 and Pa-C-1, the use of PG 58-16 at rate of 600 g/m² increased N_f compared to the tack coat rate of 200 g/m². Additionally, the influence of paving geosynthetic type on N_f is evident, as Pa-C-1 exhibited higher N_f than Pa-G-2 regardless of the tack coat rate employed.

Figure 8.4b shows the same trend for $k_{s,d}$. However, due to the variance of the results, the different types of paving geosynthetic and tack coat may not affect significantly $k_{s,d}$.

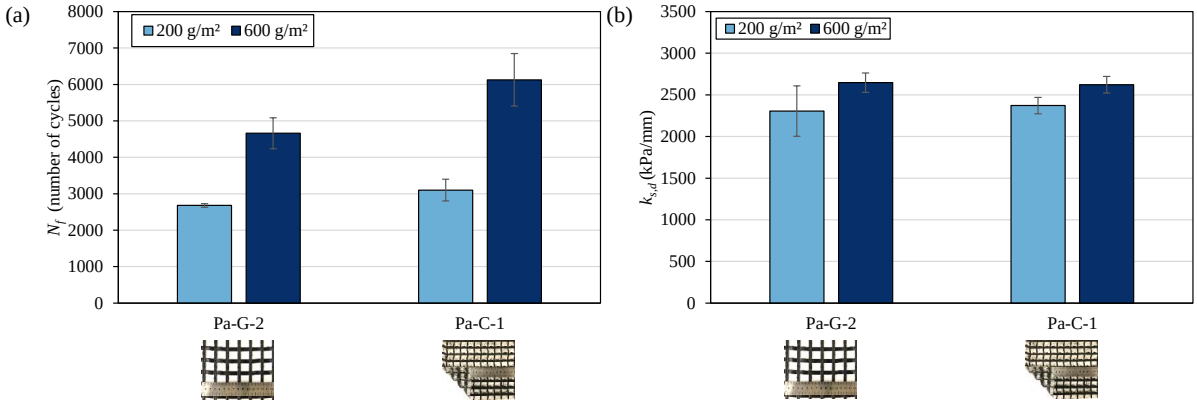

Figure 8.4 –Shear fatigue parameters for different types of paving geosynthetics and tack coat rates: (a) N_f, (b) $k_{s,d}$.

To confirm the statistical significance of the effects of paving geosynthetic type and tack coat rate on shear fatigue parameters, a two-way ANOVA was also conducted. Table 8.2 presents the results of the two-way ANOVA for shear fatigue parameters, considering the factors of paving geosynthetic type and tack coat type. The results from the two-way ANOVA are considered valid since they satisfy the assumptions of normality (Shapiro-Wilk's p-value greater than 0.05) and homoscedasticity (Levene's p-value greater than 0.05). As shown in Table 8.2, the two-way ANOVA results reveal a significant impact of both paving geosynthetic type and tack coat rate on N_f, with a p-value less than 0.05. However, no interaction is observed between these factors, as indicated by a p-value greater than 0.05. Given the significant influence of both factors on N_f, it is essential to quantify the specific effect of each. Table 8.2 presents the ω^2 values corresponding to each factor. According to Keppel and Wickens (2004), an ω^2 between 0.06 and 0.15 signifies a medium effect, while exceeding 0.15 signifies a large effect. Accordingly, Table 8.2 reveals that the paving geosynthetic type has a medium effect on N_f, and the tack coat type has a large effect. This result is particularly interesting, highlighting the importance of selecting an appropriate tack coat rate to enhance shear fatigue life. Regarding $k_{s,d}$, the two-way ANOVA results show no significant effect of either paving geosynthetic type and tack coat rate on $k_{s,d}$.

Table 8.2 – Two-way ANOVA for shear fatigue parameters results considering the paving geosynthetic type and tack coat rate.

Shear fatigue parameter	Factors	Sum of squares	Degrees of freedom	Mean square	F	p-value	ω^2	Shapiro-Wilk p-value	Levene p-value
N_f	Paving geosynthetic type	2.13E+06	1	2.13E+06	8.57	0.026	0.096	0.236	0.953
	Tack coat rate	1.50E+07	1	1.50E+07	60.48	<.001	0.756		
	Paving geosynthetic type × Tack coat rate	6.56E+05	1	6.56E+05	2.64	0.156	-		
	Error	1.49E+06	6	2.49E+05	-	-	-		
$k_{s,d}$	Paving geosynthetic type	9.72E+02	1	9.72E+02	0.0234	0.883	-	0.131	0.523
	Tack coat rate	2.09E+05	1	2.09E+05	5.03	0.066	-		
	Paving geosynthetic type × Tack coat rate	4.97E+03	1	4.97E+03	0.1195	0.741	-		
	Error	2.49E+05	6	4.16E+04	-	-	-		

8.3 Effect of test frequency on shear fatigue properties

Figure 8.5 illustrates typical curves depicting permanent shear displacement versus the number of cycles for various combinations of paving geosynthetics and test frequencies. As shown in Figure 8.5, the behavior of the permanent shear displacement curve is influenced by the test frequency, depending on the type of geosynthetic used. For Pa-G-2, an increase in the test frequency did not alter the behavior of the primary and secondary stages. However, the tertiary stage started earlier during the shear fatigue test with a frequency of 1 Hz, resulting in premature failure compared to the test with a frequency of 5 Hz. A similar trend in the primary and secondary stages is observed when the test specimen with Pa-C-1 is tested at 1 Hz, in comparison to different combinations with Pa-G-2. However, it is noted that the test frequency of 5 Hz for the test specimen with Pa-C-1 results in a decreased permanent shear displacement rate, thereby prolonging the number of cycles to failure compared to the fatigue test with a frequency of 1 Hz. Dynamic tests with a frequency of 1 Hz simulate lower vehicle speeds in the field compared to tests with a frequency of 5 Hz. According to Wang et al. (2020), lower vehicle speeds result in higher shear strain, elucidating the premature failure observed in shear fatigue tests conducted at a frequency of 1 Hz.

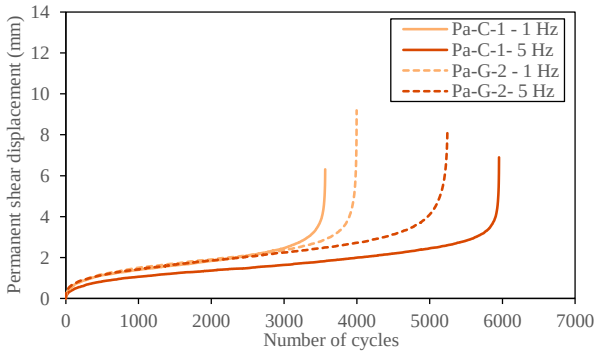

Figure 8.5 – Typical curves of permanent shear displacement versus the number of cycles for different combinations of paving geosynthetic and test frequency.

Figure 8.6 displays the averages of N_f and $k_{s,d}$, along with one standard deviation, for various combinations of paving geosynthetics and test frequencies. Figure 8.4a illustrates the impact of the test frequency on N_f. For Pa-G-2 and Pa-C-1, a test frequency of 5 Hz increased N_f compared to a test frequency of 1 Hz. Additionally, the paving geosynthetic type influenced N_f, depending on the test frequency. Pa-C-1 and Pa-G-2 exhibited similar N_f values when the test specimens underwent a test frequency of 1 Hz, suggesting that for lower vehicle speeds, Pa-C-1 and Pa-G-2 behave similarly in terms of N_f. On the other hand, the test specimen with Pa-C-2 demonstrated superior performance in terms of N_f compared to Pa-G-2 when subjected to a test frequency of 5 Hz. Regarding $k_{s,d}$, Figure 8.4b shows that a test frequency of 5 Hz slightly increased $k_{s,d}$ compared to a test frequency of 1 Hz. However, when considering the same test frequency, Pa-G-2 and Pa-C-1 showed similar values. Due to the variance in results, the different types of paving geosynthetics and test frequencies may not significantly affect $k_{s,d}$.

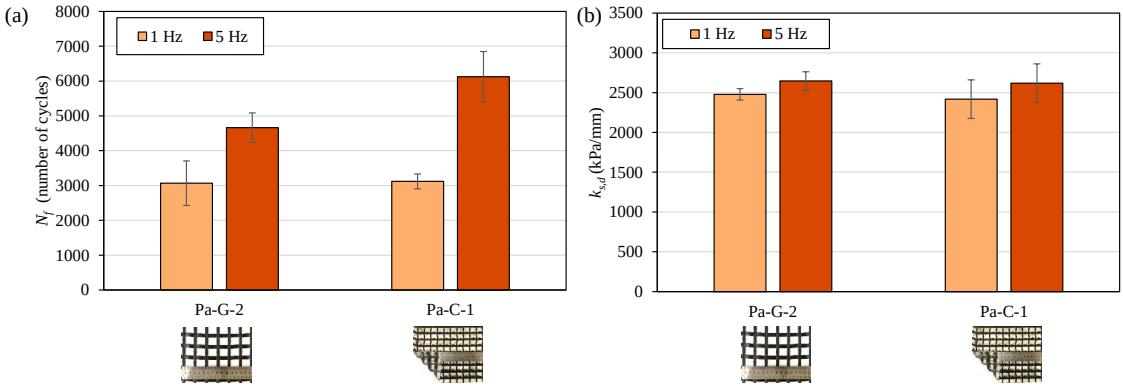

Figure 8.6 – Shear fatigue parameters for different types of paving geosynthetic and test frequency: (a) N_f, (b) $k_{s,d}$.

To confirm the statistical significance of the effects of paving geosynthetic type and test frequency on shear fatigue parameters, a two-way ANOVA was also conducted. Table 8.3 presents the results of the two-way ANOVA for shear fatigue parameters, considering the factors of paving geosynthetic type and test frequency. The results from the two-way ANOVA are considered valid since they satisfy the assumptions of normality (Shapiro-Wilk's p-value greater than 0.05) and homoscedasticity (Levene's p-value greater than 0.05). As shown in Table 8.3, the two-way ANOVA results reveal a significant effect of both paving geosynthetic type and test frequency on N_f, with a p-value less than 0.05. However, no interaction is observed between these factors, as indicated by a p-value greater than 0.05. Table 8.2 presents the ω^2 values corresponding to each factor. According to Keppel and Wickens (2004) classification, the paving geosynthetic type has a medium effect on N_f, and the test frequency has a large effect. Regarding $k_{s,d}$, the two-way ANOVA results show no significant effect of either paving geosynthetic type and test frequency on $k_{s,d}$.

Table 8.3 – Two-way ANOVA for shear fatigue parameters results considering the paving geosynthetic type and test frequency.

Shear fatigue parameter	Factors	Sum of squares	Degrees of freedom	Mean square	F	p-value	ω^2	Shapiro-Wilk p-value	Levene p-value
N_f	Paving geosynthetic type	1.73E+06	1	2.13E+06	5.99	0.040	0.066	0.281	0.483
	Test frequency	1.59E+07	1	1.50E+07	55.10	<.001	0.718		
	Paving geosynthetic type × Test frequency	1.50E+08	1	6.56E+05	5.21	0.052	-		
	Error	2.30E+06	8	2.88E+05	-	-	-		
$k_{s,d}$	Paving geosynthetic type	5.50E+03	1	5.50E+03	0.1592	0.700	-	0.1115	0.993
	Test frequency	1.04E+05	1	1.04E+05	3.0107	0.121	-		
	Paving geosynthetic type × Test frequency	9.14E+02	1	9.14E+02	0.0264	0.875	-		
	Error	2.76E+05	8	3.46E+04	-	-	-		

8.4 Effect of different paving geosynthetics on shear fatigue properties

Figure 8.7 shows the typical curves of permanent shear displacement versus the number of cycles for combinations with different paving geosynthetics combined with PG 58-16 at a tack coat rate of 600 g/m². As can observed in Figure 8.7, the presence of paving geosynthetic within asphalt overlays reduce in more than fifty percent the shear fatigue life when compared to the control test

specimen. This behavior was expected since non-reinforced asphalt overlays exhibit greater interface bonding compared to asphalt systems with paving geosynthetic. However, they do not provide the advantages of reducing reflective cracking and enhancing pavement performance. Therefore, it is crucial to comprehend the geosynthetic properties that enhance shear fatigue life.

The influence of paving geosynthetic type on the curve of permanent shear displacement versus the number of cycles can also be observed in Figure 8.7. There is difference in the number of cycles required for the complete failure of the interface between the various combinations with paving geosynthetics, as well as a distinction in the linear segment of the curve. This signifies varying permanent displacement rates between the paving geosynthetics.

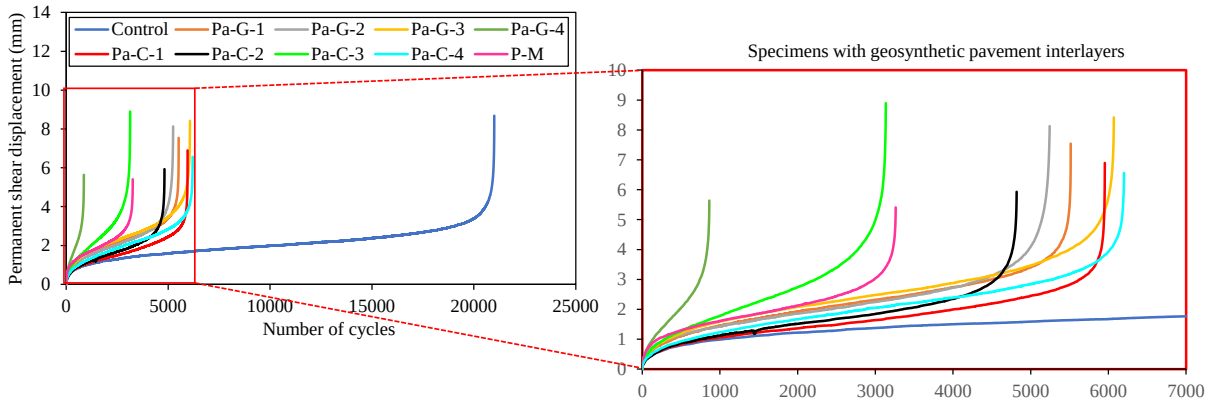

Figure 8.7 – Typical curves of permanent shear displacement versus the number of cycles for combinations with different paving geosynthetics combined with PG 58-16 at a tack coat rate of 600 g/m².

Figure 8.8 illustrates the average N_f for the combinations with different paving geosynthetics. The average values are plotted with one standard deviation. The average values of N_f ranged from 735 to 6125, indicating the influence of different geosynthetic properties on N_f. These results align with those obtained by Safavizadeh et al. (2022a), despite variations in the testing device and configuration.

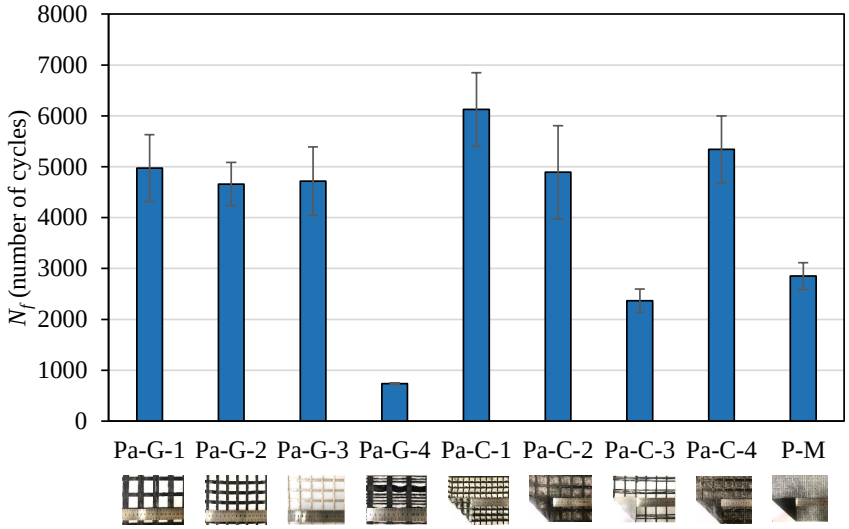

Figure 8.8 – Average shear fatigue life for the combinations with different geosynthetics.

Figure 8.8 shows that Pa-C-1 exhibited the highest N_f value, suggesting the impact of bitumen coating content (B_{cc}) on N_f, as Pa-C-1 has the highest Bcc among all geosynthetics. Among the paving geogrids, Pa-G-1 demonstrated the highest N_f value compared to Pa-G-2 and Pa-G-3, indicating the influence of the geogrid mesh area, with Pa-G-1 having the larger geogrid mesh area. However, despite Pa-G-3 having a larger geogrid mesh area than Pa-G-2, both exhibited similar N_f values, supporting the influence of B_{cc}, since Pa-G-3 lacks bitumen coating while Pa-G-2 has it.

Pa-G-4 showed the lowest N_f, suggesting a negative influence of the presence of fabric strips crossing the geogrid mesh. Pa-C-3 and P-M also had comparatively lower N_f values, indicating a negative influence from the absence of mesh opening. Conversely, Pa-C-2 and Pa-C-4 had comparatively higher N_f values, suggesting that the presence of ultra-thin fabric backing did not completely impair the through-hole bonding mechanism. This also supports the influence of the geogrid mesh area, as both paving geosynthetics have the largest geogrid mesh area among all the paving geosynthetics.

Figure 8.9 depicts the average cyclic interface shear stiffness modulus ($k_{s,d}$), along with one standard deviation, for the control test specimen and for test specimen with different paving geosynthetics. As can be observed in Figure 8.9, the control test specimen showed $k_{s,d}$ value of 3041 kPa/mm, while the test specimens with paving geosynthetic ranged between 2158 and 2886 kPa/mm, indicating that the presence of paving geosynthetic within asphalt overlays also reduces the $k_{s,d}$. It also suggests the influence of the different properties of geosynthetics on $k_{s,d.}$

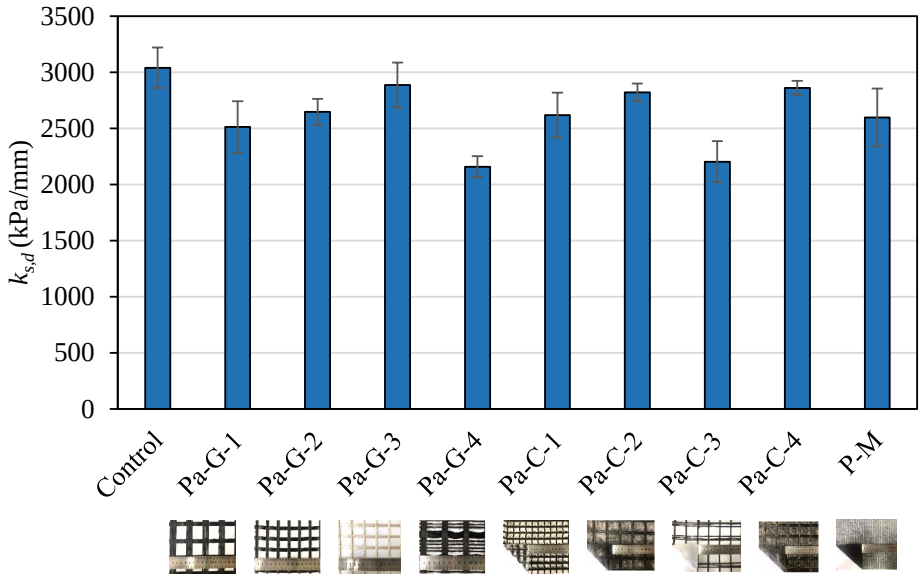

Figure 8.9 – Average cyclic interface shear stiffness modulus for the control test specimen and for test specimen with different paving geosynthetics.

In order to confirm if the effect of the different paving geosynthetics on shear fatigue parameters is statistically significant, a one-way ANOVA was performed. One-way ANOVA helps determine if any of the differences between the average values are statistically significant by comparing the p-value to the significance level of 0.05. If the p-value is less than 0.05, it indicates that some of the average values differ significantly. Table 8.4 presents the result of one-way ANOVA and reveals the existence of a significant difference in shear fatigue parameters due to the different paving geosynthetics. This finding is specific significant because, unlike previous ANOVA tests, a greater quantity of paving geosynthetic revealed a significant impact of the paving geosynthetic type on $k_{s,d}$.

Table 8.4 – One-way ANOVA of shear fatigue parameters for different paving geosynthetics.

		Degrees of	Degrees of	ANOVA	Shapiro-Wilk	Levene
Shear fatigue parameters	F	freedom 1	freedom 2	p-value	p-value	p-value
N_f	26.73	8	18	<.001	0.597	0.073
$k_{s,d}$	6.61	8	18	<.001	0.620	0.174

Figure 8.10 illustrates the correlation between $k_{s,d}$ and N_f. As shown in the figure, the correlation coefficient (r) is 0.78, indicating a high positive correlation between $k_{s,d}$ and N_f, according to Taylor's classification (Taylor, 1990). This result is particularly noteworthy because

an understanding of the geosynthetic properties that enhance N_f also contributes to the increase in $k_{s,d}$.

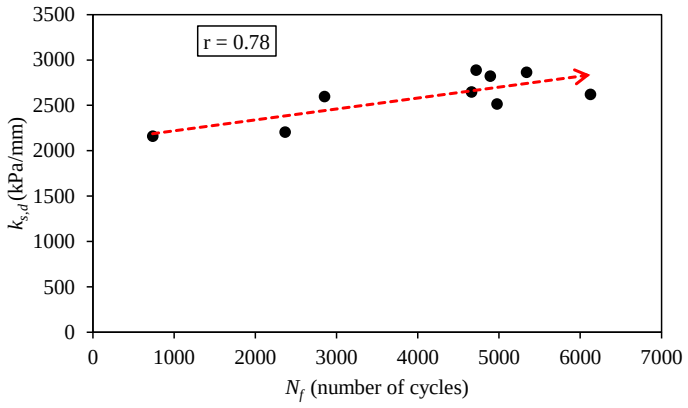

Figure 8.10 – Correlation between $k_{s,d.}$ and N_f..

8.4.1 Multiple linear regression analysis for shear fatigue life based on geosynthetic properties

Given the significant effect of the different paving geosynthetics on N_f, a multiple linear regression (MLR) analysis can also be conducted to understand potential relationships between geosynthetic properties and N_f. Additionally, this analysis allows for predicting N_f under the interface condition with PG 58-16 at a rate of 600 g/m². The same approach used to develop MLR models for *ISS* was applied in developing the MLR model for N_f.

The development of MLR models considered various factors, including the suspected influence of the geogrid mesh area (A_{gm}), bitumen coating content (B_{cc}), and the presence of different fabric types on paving geosynthetics. Additionally, other properties, such as tensile stiffness, were evaluated during the development stage of the MLR models. The development stage revealed that tensile stiffness does not affect N_f. Additionally, it confirmed suspicions that A_{gm}, B_{cc}, and the presence of different fabric types on paving geosynthetics are the predictor variables significantly affecting N_f. Descriptions of these variables can be found in Table 8.5. The MLR model, predicting N_f, is as follows:

$$N_f = \beta_0 + \beta_1 \cdot A_{gm} + \beta_2 \cdot B_{cc} + \beta_3 \cdot F_{strips} + \beta_4 \cdot F_{thin} + \beta_5 \cdot F_{thick} \quad (8.1)$$

Table 8.5 – Description of predictor variables for N_f.

Predictor variable	Unit	Description
A_{gm}	mm²	geogrid mesh area*
B_{cc}	%	bitumen coating content
F_{strips}	-	dichotomous variable (1 or 0) indicating the presence or not of fabric strips crossing the geogrid mesh
F_{thin}	-	dichotomous variable (1 or 0) indicating the presence or absence of a fabric backing with a thickness less than 0.5 mm.**
F_{thick}	-	dichotomous variable (1 or 0) indicating the presence or absence of a fabric backing with a thickness greater than 0.5 mm.

* A_{gm} should equal 0, in the presence of a thick fabric backing, strips of fabric crossing the geogrid mesh area, or paving mat.

** F_{thin} should equal 1, when a paving mat is used.

Table 8.6 outlines the statistics of the predictive model established and the assumption checks. As can be observed in Table 8.3, the proposed predictive model exhibited a linear relationship with at least one geosynthetic property, as the p-value from the overall model is less than 0.05. The goodness of fit, measured by R², explain the linear variation in N_f based on the selected geosynthetic properties in approximately 92%. It is noteworthy that predictive model meets the assumptions of normality, homoscedasticity, and absence of autocorrelation.

Table 8.6 – Statistics of the predictive model established for shear fatigue life and the assumption checks.

Model	R²	F	Degrees of freedom		Model	Shapiro-Wilk test	Breusch-Pagan test	Durbin-watson test
			Regression	Residual	*p*-value	*p*-value	*p*-value	*p*-value
PG 58-16 600 g/m²	0.917	46.2	5	21	<.001	0.620	0.061	0.918

Table 8.7 presents the results of significance tests for each regression coefficient related to geosynthetic properties selected. It should be noted that only the individual regression coefficients rejecting the null hypothesis (p-value < 0.05) remained in the predictive model. In other words, only the geosynthetic properties that significantly linearly affected the N_f were included. The selected geosynthetic properties also satisfied the assumption of no multicollinearity, as the Variance Inflation Factor (VIF) is less than 4.

Table 8.7 – Significance test results for each regression coefficient selected to predict shear fatigue life.

Model	Regressor	Regression coefficient	Standardized regression coefficient	SE	*p*-value	VIF
PG 58-16 600 g/m²	Intercept	3810.30		247.40	<.001	
	B_{cc}	59.07	0.511	8.655	<.001	1.19
	A_{gm}	1.30	0.332	0.302	<0.001	1.22
	F_{strips}	-3181.29	-1.851	400.92	<.001	1.12
	F_{thin}	-909.80	-0.529	273.523	0.003	1.12
	F_{thick}	-1473.16	-0.857	402.688	0.001	1.12

The results presented in Table 8.7 demonstrate the linear impact of three geosynthetic properties on the N_f as predictor variables: geogrid mesh area (A_{gm}), bitumen coating content (B_{cc}), and the presence of different types of fabric in the paving geosynthetics (F_{strips}, F_{thin}, F_{thick}). As the positive coefficients are related to numerical variables, it implies that increasing predictor variable values result in increased N_f. The negative coefficients are related to categorical variables, indicating that the presence of geosynthetic property decrease N_f. Specifically, geogrid mesh area, and the bitumen coating content positively affect N_f. Otherwise, the the presence of different types of fabric in the paving geosynthetics negatively impact N_f.

The positive impact of the geogrid mesh area is explained by the THB mechanism (Sudarsanan et al., 2018b). This mechanism involves increased asphalt-to-asphalt contact with a larger geogrid mesh area, facilitating effective interlocking among HMA aggregates. This mechanism also enhances the shear fatigue life. Figure 8.11 illustrates the effect of the geogrid mesh area in shear fatigue tests.

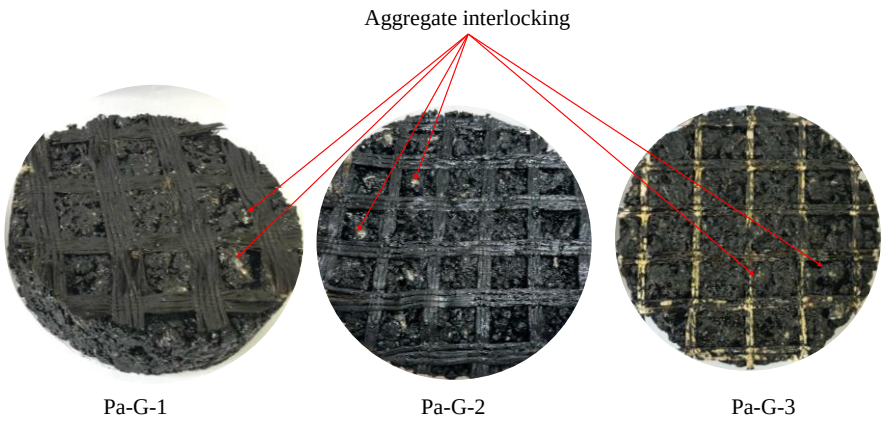

Figure 8.11 – Effect of geogrid mesh area causing aggregate interlocking.

Figure 8.12 illustrates the geosynthetic properties affecting shear fatigue life. The positive effect of bitumen coating content can be explained by the enhancement of adhesion mechanism between the paving geosynthetic and surrounding asphalt layers, as can be observed in Figure 8.12a. The standardized regression coefficients indicate the level of impact of each geosynthetic property on N_f. As shown in Table 8.7, bitumen coating content has a more positive effect on shear fatigue life than the geogrid mesh area. Examining the negative impact levels of different types of fabric in paving geosynthetics in Table 8.7 reveals that fabric strips crossing the geogrid mesh have the most significant effect on N_f, followed by the presence of a thick fabric backing and, lastly, a thin fabric backing. The presence of fabric strips reduces the effect of the THB mechanism (Figure 8.12b) but does not enhance the adhesion mechanism, resulting in the highest negative impact. A thick fabric backing impairs the THB mechanism but enhances the adhesion mechanism when impregnated with bitumen (Figure 8.12c). Lastly, a thin fabric backing reduces the effect of THB but does not impair it (Figure 8.12d).

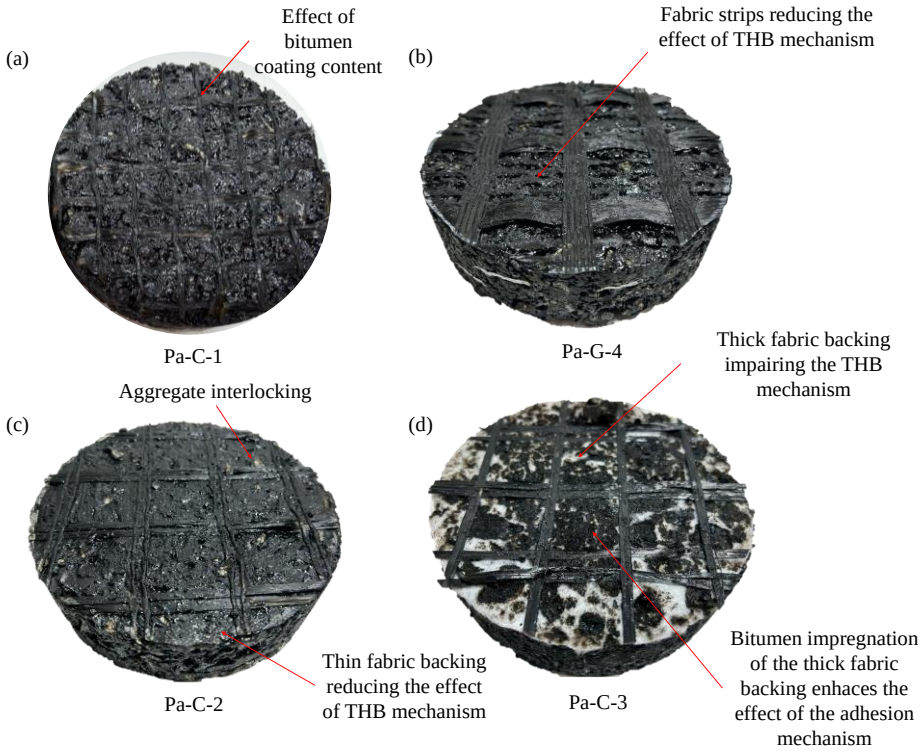

Figure 8.12 – Illustration of the geosynthetic properties affecting shear fatigue life: (a) bitumen-coated geogrid of Pa-C-1 attached to surrounding asphalt layer facilitating adhesion, (b) fabric strips reducing the effect of THB mechanism, (c) Thin fabric backing reducing the effect of THB mechanism, and (d) thick fabric backing with lower tack coat saturation impairing THB mechanism.

Fig. 8.13 illustrates the scatterplot comparing predicted and average measured N_f values in this study. As shown in Figure 8.13, there is a good agreement between the predicted and average measured N_f values, as the results closely align with the equity line. This indicates that the MLR model established demonstrates high accuracy in predicting average measured N_f. Figure 8.13 also displays the 95% confidence intervals for future average N_f values obtained from future shear fatigue tests.

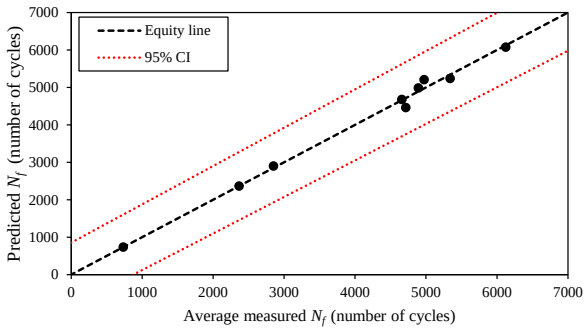

Figure 8.13 – Scatterplot comparing predicted and average measured N_f values in this study.

8.5 Correlation between shear fatigue life and interface shear strength

Figure 8.14 depicts the correlation between the average values of N_f and *ISS* in test specimens using paving geosynthetics, tested through shear fatigue and interface shear bond tests. The Figure 8.14 also presents the results of linear regression to predict N_f based on average *ISS* values. All specimens feature an interface condition with PG 58-16 as the tack coat, applied at a rate of 600 g/m². According to Taylor (1990), a correlation coefficient *r* between 0.6 and 0.9 signifies a high correlation, while exceeding 0.90 signifies a very high correlation.

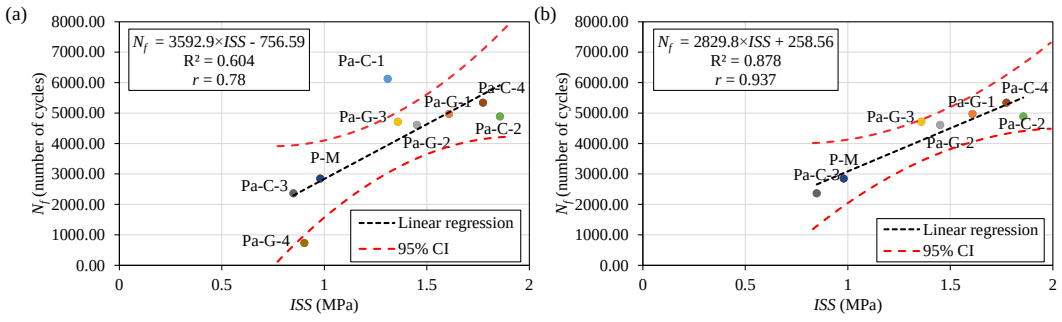

Figure 8.14 – Linear regression and correlation between shear fatigue life and interface shear strength: (a) considering all paving geosynthetics, (b) after excluding Pa-C-1 and Pa-G-4.

Figure 8.14a shows a high correlation between average N_f and *ISS* values for all paving geosynthetics selected in this study. However, the linear regression results inaccurately predict the average N_f value based on ISS for Pa-C-1 and Pa-G-4, as these results fall outside the 95% confidence interval (CI). This discrepancy can be explained by the comparatively high B_{cc} of 49% for Pa-C-1, while other paving geosynthetics have Bcc ranging from the absence of B_{cc} to 13.5%. As observed in the predictive models, B_{cc} has a significant effect on N_f, whereas the predictive model for *ISS*, for the interface condition with PG 58-16 as the tack coat applied at a rate of 600 g/m², does not show a significant effect of B_{cc} on *ISS*.

In the case of Pa-G-4, the presence of fabric strips has a significantly negative effect on N_f, while concerning *ISS*, this property affects similarly to the presence of thick fabric backing. Therefore, Pa-C-1 and Pa-G-4 were excluded from the linear regression analysis. Figure 8.14b illustrates the results of correlation and linear regression after removing Pa-C-1 and Pa-G-4. The results reveal a very high correlation between N_f and *ISS*, demonstrating high accuracy in predicting average N_f values, as the coefficient of determination (R^2) explains 87.8% of the variability of N_f due to *ISS*. It is noteworthy that all the results fall within the 95% CI limit.

Figure 8.15 shows the correlation between the average values of N_f and k. The figure also presents the results of linear regression to predict N_f based on average k values. All specimens feature an interface condition with PG 58-16 as the tack coat, applied at a rate of 600 g/m². As shown in Figure 8.15a, there is a moderate positive correlation with a correlation coefficient (r) of 0.648, as per Taylor's classification (Taylor, 1990). Again, the linear regression results inaccurately predict the average N_f value based on *ISS* for Pa-C-1 and Pa-G-4, as these results fall outside the 95% confidence interval, for the same reason explained for the previous analysis. Therefore, Pa-C-1 and Pa-G-4 were excluded from the linear regression analysis. Figure 8.15b illustrates the results of correlation and linear regression after removing Pa-C-1 and Pa-G-4. The results reveal a very high correlation between N_f and k, demonstrating high accuracy in predicting average N_f values, as the coefficient of determination (R^2) explains 81.8% of the variability of N_f due to k. It is noteworthy that all the results fall within the 95% CI limit.

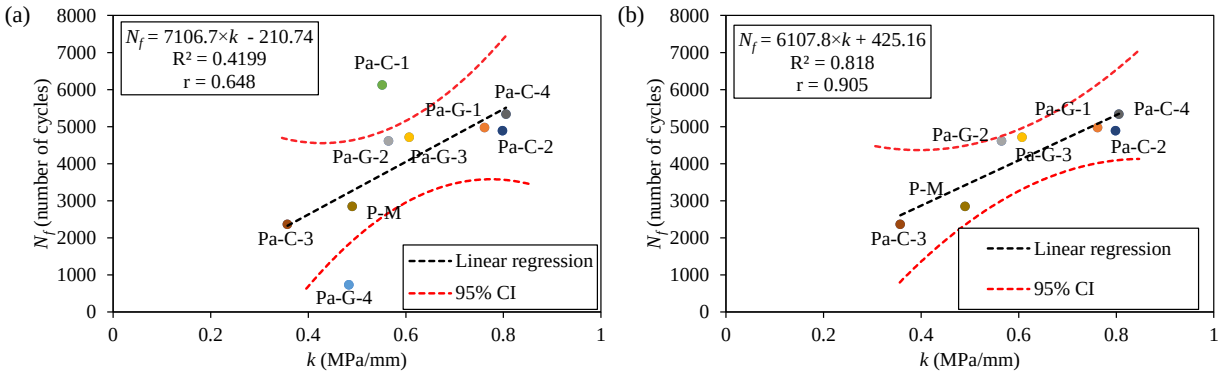

Figure 8.15 – Linear regression and correlation between shear fatigue life and interface shear strength: (a) considering all paving geosynthetics, (b) after excluding Pa-C-1 and Pa-G-4.

CHAPTER 9. CONCLUSIONS AND RECOMMENDATIONS

9.1 Conclusions

The study conducted an analysis involving various factors to comprehend how different paving geosynthetics, tack coat types, and rates interact and influence influencing interface bond and shear fatigue parameters. It involved conducting interface shear bond and shear fatigue tests using a novel loading device and proposed test methods.

Results from the Leutner shear test revealed that meeting the minimum required interface shear strength depended on the specific paving geosynthetic and tack coat characteristics. However, no clear trend in interface bond strength behavior was discernible, indicating complex interactions among the variables. Subsequently, a multifactorial analysis of variance showed significant effects of paving geosynthetic type, tack coat type, application rate, and their interactions on interface shear strength. The paving geosynthetic type showed the larger impact on interface bond strength. Further analysis via multiple linear regression identified specific geosynthetic properties, such as mesh area, thickness, and presence of bitumen coating, that significantly affected interface bond strength. Predictive models based on these properties (mesh area, thickness, and presence of bitumen coating) accurately estimated interface shear strength of geosynthetic-reinforced asphalt systems for different tack coat types (emulsion CRS-1 and PG 58-16), and tack coat rates (400, 600 and 800 g/m2), aligned well with existing literature data, as well as provided insights into achieving the minimum required interface shear strength.

A testing protocol to conduct shear fatigue tests on geosynthetic-reinforced asphalt systems was presented in this study. The shear fatigue test results demonstrated that paving geosynthetic type, test frequency, tack coat type, and rate all influence the behavior of the permanent shear displacement curve. Analysis confirmed their significant impact on shear fatigue life, with paving geosynthetic type, testing frequency, tack coat type, and tack coat rate emerging as prominent factors affecting cyclic interface shear stiffness modulus. Multiple linear regression identified geogrid mesh area, bitumen coating content, and fabric backing type as significant properties affecting shear fatigue life. Moreover, correlation analysis revealed a strong association between shear fatigue life and interface bond parameters. Linear regression analysis further demonstrated

that shear fatigue life of geosynthetic-reinforced asphalt systems can be predicted based on interface shear strength and shear stiffness modulus resulting from monotonic tests.

In summary, this study sheds light on the various geosynthetic properties influencing interface bond and shear fatigue parameters, as well as the impact of tack coat type and rate, along with test frequency in the case of shear fatigue tests. The findings of this study are limited to the specific geosynthetics, tack coat type and application rate, as well as the test conditions employed, including displacement rate, temperature, gap distance, frequency, peak load, and seating load. The extrapolation of the findings of this study to other paving geosynthetics and other interface conditions requires careful considerations. The predictive models and correlations obtained in this study should be checked and improved for different paving geosynthetic types, tack coat type and rate, as well as different types of asphalt mixture.

9.2 Recommendations for future work

Additional studies should be conducted to verify the impact of macrotexture surface on asphalt layers, considering various paving geosynthetic types, tack coat types, and rates. Additionally, it is suggested to examine the influence of specimen type (whether laboratory-prepared or field-extracted specimens) along with different paving geosynthetic types, tack coat types, and rates. This additional investigation aims to determine if the previously observed 50% increase in *ISS* for laboratory-prepared specimens compared to extracted cores from the field remains consistent across different tack coat rates and types. The experimental data generated from this study can be utilized to model and assess long-term pavement response, providing a valuable tool in the absence of specifications addressing interface bonds in pavement systems with paving geosynthetics.

REFERENCES

AASHTO T27, 2020. Standard Method of Test for Sieve Analysis of Fine and Coarse Aggregates.

AASHTO T37, 2007. Standard Method of Test for Sieve Analysis of Mineral Filler for Hot Mix Asphalt (HMA).

AASHTO T84, 2013. Standard Method of Test for Specific Gravity and Absorption of Fine Aggregate.

AASHTO T85, 2021. Standard Method of Test for Specific Gravity and Absorption of Coarse Aggregate.

AASHTO TP 114, 2018. Determining the Interlayer Shear Strength (ISS) of Asphalt Pavement Layers.

AASHTO T133, 2019. Standard Method of Test for Density of Hydraulic Cement.

AASHTO T304, 2017. Standard Method of Test for Uncompacted Void Content of Fine Aggregate.

AASHTO T330, 2007. Standard Method of Test for The Qualitative Detection of Harmful Clays of the Smectite Group in Aggregates Using Methylene Blue.

AASHTO T378, 2022. Determining the Dynamic Modulus and Flow Number for Asphalt Mixtures Using the Asphalt Mixture Performance Tester (AMPT).

Al Hakim, B., 2002. The importance of good bond between bituminous layers, in: 9th International Conference on Asphalt Pavements. Copenhague.

Alavi, A.H., Ameri, M., Gandomi, A.H., Mirzahosseini, M.R., 2011. Formulation of flow number of asphalt mixes using a hybrid computational method. Constr. Build. Mater. 25, 1338–1355. https://doi.org/10.1016/j.conbuildmat.2010.09.010

Ante, J.R.O., 2016. Desempenho de misturas asfálticas reforçadas com geossintéticos. Universidade de Brasília. https://doi.org/10.26512/2016.11.T.22587

ARTERIS, 2021. ES027: Concreto asfáltico usinado a quente - CA.

ASTM C131, 2020. Standard Test Method for Resistance to Degradation of Small-Size Coarse Aggregate by Abrasion and Impact in the Los Angeles Machine. https://doi.org/10.1520/C0131

ASTM C1097, 2019. Standard Specification for Hydrated Lime for Use in Asphalt Cement or Bituminous Paving Mixtures. https://doi.org/10.1520/C1097-19.2

ASTM D5, 2020. Standard Test Method for Penetration of Bituminous Materials.

https://doi.org/10.1520/mnl10829m

ASTM D36, 2020. Standard Test Method for Softening Point of Bitumen (Ring-and-Ball Apparatus). West Conshohocken, PA, USA. https://doi.org/10.1520/mnl10830m

ASTM D70, 2017. Standard Test Method for Specific Gravity and Density of Semi-Solid Bituminous Materials (Pycnometer Method).

ASTM D92, 2021. Standard Test Method for Flash and Fire Points by Cleveland Open Cup Tester. West Conshohocken, PA, USA. https://doi.org/10.1520/D0092-18.

ASTM D113, 2017. Standard Test Method for Ductility of Asphalt Materials. West Conshohocken. https://doi.org/10.1520/D0113- 17

ASTM D448, 2012. Standard Classification for Sizes of Aggregate for Road and Bridge Construction. https://doi.org/10.1520/D0448-12R22.2

ASTM D2419, 2022. Standard Test Method for Sand Equivalent Value of Soils and Fine Aggregate. https://doi.org/10.1520/D2419-22.1

ASTM D2726, 2017. Standard test method for bulk specific gravity and density of compacted asphalt mixtures. West Conshohocken. https://doi.org/10.1520/D2726

ASTM D4402, 2023. Standard Test Method for Viscosity Determination of Asphalt at Elevated Temperatures Using a Rotational Viscometer. West Conshohocken, PA, USA. https://doi.org/10.1520/D4402

ASTM D5199, 2019. Standard Test Method for Measuring the Nominal Thickness of Geosynthetics. https://doi.org/10.1520/D5199-12.2

ASTM D5261, 2018. Standard Test Method for Measuring Mass per Unit Area of Geotextiles. https://doi.org/10.1520/D5261-10R18.2

ASTM D6140, 2022. Standard Test Method to Determine Asphalt Retention of Paving Fabrics Used in Asphalt Paving for Full-Width Applications. https://doi.org/10.1520/D6140-00R09.2

ASTM D6926, 2020. Standard Practice for Preparation of Asphalt Mixture Specimens Using Marshall Apparatus. West Conshohocken. https://doi.org/10.1520/D6926-20.2

ASTM D6997, 2020. Standard Test Method for Distillation of Emulsified Asphalt. https://doi.org/10.1520/D6997-12R20.2

ASTM D7239, 2018. Standard Specification for Hybrid Geosynthetic Paving Mat for Highway Applications.

ASTM D7402, 2017b. Standard Practice for Identifying Cationic Emulsified Asphalts.

https://doi.org/10.1520/D7402-09R17.2

ASTM D7496, 2018. Standard Test Method for Viscosity of Emulsified Asphalt by Saybolt Furol Viscometer. https://doi.org/10.1520/D7496-18.2

ASTM D8237, 2021. Standard Test Method for Determining Fatigue Failure of Asphalt-Aggregate Mixtures with the Four-Point Beam Fatigue Device. West Conshohocken, PA, USA. https://doi.org/10.1520/D8237-21.1

Austrian Standards Institute, 1997. ÖNORM B 3639-1: Technische Asphalte für den Straßenbau und verwandte Gebiete - Prüfung - Schubverbund von Asphaltschichten.

Bae, A., Mohammad, L.N., Elseifi, M.A., Button, J., Patel, N., 2010. Effects of temperature on interface shear strength of emulsified tack coats and its relationship to rheological properties. Transp. Res. Rec. 2180, 102–109. https://doi.org/10.3141/2180-12

Bahia, H., Swiertz, D., Mohammad, L.N., 2019. Investigation of Tack Coat Materials Tracking Performance.

Bhasin, A., Castelo Branco, V.T., Masad, E., Little, D.N., 2009. Quantitative Comparison of Energy Methods to Characterize Fatigue in Asphalt Materials. J. Mater. Civ. Eng. 21, 83–92. https://doi.org/10.1061/(asce)0899-1561(2009)21:2(83)

Breusch, T.S., Pagan, A.R., 1979. A Simple Test for Heteroscedasticity and Random Coefficient Variation. Econometrica 47, 1287. https://doi.org/10.2307/1911963

Canestrari, F., Attia, T., Di Benedetto, H., Graziani, A., Jaskula, P., Kim, Y.R., Maliszewski, M., Pais, J.C., Petit, C., Raab, C., Ragni, D., Rys, D., Sangiorgi, C., Sauzéat, C., Zofka, A., 2022a. Interlaboratory Test to Characterize the Cyclic Behavior of Bituminous Interlayers: An Overview of Testing Equipment and Protocols, RILEM Bookseries. Springer International Publishing. https://doi.org/10.1007/978-3-030-46455-4_4

Canestrari, F., Cardone, F., Gaudenzi, E., Chiola, D., Gasbarro, N., Ferrotti, G., 2022b. Interlayer bonding characterization of interfaces reinforced with geocomposites in field applications. Geotext. Geomembranes 50, 154–162. https://doi.org/10.1016/j.geotexmem.2021.09.010

Canestrari, F., D'Andrea, A., Ferrotti, G., Graziani, A., Partl, M.N., Petit, C., Raab, C., Sangiorgi, C., 2018. Advanced Interface Testing of Grids in Asphalt Pavements, in: Partl, M., Porot, L., Di Benedetto, H., Canestrari, F., Marsac, P., Tebaldi, G. (Eds.), Testing and Characterization of Sustainable Innovative Bituminous Materials and Systems: State-of-the-Art Report of the RILEM Technical Committee 237-SIB. Springer International Publishing, pp. 127–202.

https://doi.org/10.1007/978-3-319-71023-5_4

Canestrari, F., Ferrotti, G., Lu, X., Millien, A., Partl, M. N., Petit, C., Phelipot-Mardelé, A., Piber, H., Raab, C., 2013. Mechanical Testing of Interlayer Bonding in Asphalt Pavements, in: Partl, Manfred N., Bahia, H.U., Canestrari, Francesco, de la Roche, C., Di Benedetto, H., Piber, Herald, Sybilski, D. (Eds.), Advances in Interlaboratory Testing and Evaluation of Bituminous Materials: State-of-the-Art Report of the RILEM Technical Committee 206, RILEM State-of-the-Art Reports. Springer Netherlands, Dordrecht, pp. 303–360. https://doi.org/10.1007/978-94-007-5104-0_6

Canestrari, F., Ferrotti, G., Partl, M., Santagata, E., 2005. Advanced Testing and Characterization of Interlayer Shear Resistance. Transp. Res. Rec. J. Transp. Res. Board 1929, 69–78. https://doi.org/10.3141/1929-09

Canestrari, F., Santagata, E., 2005. Temperature effects on the shear behaviour of tack coat emulsions used in flexible pavements. Int. J. Pavement Eng. 6, 39–46. https://doi.org/10.1080/10298430500068720

Chen, J.S., Huang, C.C., 2010. Effect of surface characteristics on bonding properties of bituminous tack coat. Transp. Res. Rec. https://doi.org/10.3141/2180-16

Cheng, H., Sun, L., Wang, Y., Chen, X., 2021. Effects of actual loading waveforms on the fatigue behaviours of asphalt mixtures. Int. J. Fatigue 151, 106386. https://doi.org/10.1016/j.ijfatigue.2021.106386

Cho, S.H., Karshenas, A., Tayebali, A.A., Guddati, M.N., Kim, Y.R., 2017. A mechanistic approach to evaluate the potential of the debonding distress in asphalt pavements. Int. J. Pavement Eng. 18, 1098–1110. https://doi.org/10.1080/10298436.2016.1149837

Choi, Y.K., Sutanto, M.H., Collop, A.C., Airey, G.D., 2005. Bond between asphalt layers. Project Report to the UK Highways Agency.

Collop, A.C., Sutanto, M.H., Airey, G.D., Elliott, R.C., 2009. Shear bond strength between asphalt layers for laboratory prepared samples and field cores. Constr. Build. Mater. 23, 2251–2258. https://doi.org/10.1016/j.conbuildmat.2008.11.017

Correia, N.S., Mugayar, A.N., 2021. Effect of binder rates and geogrid characteristics on the shear bond strength of reinforced asphalt interfaces. Constr. Build. Mater. 269, 121292. https://doi.org/10.1016/j.conbuildmat.2020.121292

Correia, N.S., Souza, T.R., Silva, M.P.S., Kumar, V.V., 2023. Investigations on interlayer shear

strength characteristics of geosynthetic-reinforced asphalt overlay sections at Salvador International Airport. Road Mater. Pavement Des. 24, 1542–1558. https://doi.org/10.1080/14680629.2022.2092021

Correia, N.S., Zornberg, J.G., 2018. Strain distribution along geogrid-reinforced asphalt overlays under traffic loading. Geotext. Geomembranes 46, 111–120. https://doi.org/10.1016/j.geotexmem.2017.10.002

Covey, D., Coleri, E., Mahmoud, A., 2017. Tack Coat Rheological Properties and the Effects on Interlayer Shear Strength. J. Mater. Civ. Eng. 29, 04017221. https://doi.org/10.1061/(asce)mt.1943-5533.0002054

D'Andrea, A., Russo, S., Tozzo, C., 2013. Interlayer shear testing under combined state of stress. Adv. Mater. Res. 723, 381–388. https://doi.org/10.4028/www.scientific.net/AMR.723.381

D'Andrea, A., Tozzo, C., 2016. Dynamic tests on bituminous layers interface. Mater. Struct. 49, 917–928. https://doi.org/10.1617/s11527-015-0548-z

Debnath, P., Dey, A.K., 2017. Prediction of Laboratory Peak Shear Stress Along the Cohesive Soil–Geosynthetic Interface Using Artificial Neural Network. Geotech. Geol. Eng. 35, 445–461. https://doi.org/10.1007/s10706-016-0119-2

Department of Transport and Main Roads, 2021. Transport and Main Roads Specifications - MRTS104: Retarding Pavement Reflective Cracking using Asphalt Geosynthetics. Queensland.

DER, 2006. ET-DE-P00/043: Tratamento Anti-Reflexão De Trincas Com Geossintético.

Diakhaté, M., Millien, A., Petit, C., Phelipot-Mardelé, A., Pouteau, B., 2011. Experimental investigation of tack coat fatigue performance: Towards an improved lifetime assessment of pavement structure interfaces. Constr. Build. Mater. 25, 1123–1133. https://doi.org/10.1016/j.conbuildmat.2010.06.064

Diakhaté, M., Phelipot-Mardelé, A., Millien, A., Petit, C., Pouteau, B., Goacolou, H., 2007. Comportement en cisaillement des couches d'accrochage : comparaison entre essais monotones de cisaillement et de torsion, in: 25e Rencontres de l'AUGC. pp. 23–25.

Diakhate, M., Phelipot, A., Millien, A., Petit, C., 2006. Shear fatigue behaviour of tack coats in pavements. Road Mater. Pavement Des. 7, 201–222. https://doi.org/10.1080/14680629.2006.9690033

DNIT, 2018. ME 184: Pavimentação - Misturas asfálticas - Ensaio uniaxial de carga repetida para

determinação da resistência à deformação permanente – Método de ensaio.

DNIT, 2010. ES 145: Pintura de ligação com ligante asfáltico convencional - Especificação de serviço.

DNIT, 2006a. Manual de restauração de pavimentos asfálticos.

DNIT, 2006b. ES 031: Pavimentos flexíveis: Concreto asfáltico: Especificação de serviço. Rio de Janeiro.

DNV, 2017. Pliego de especificaciones técnicas generales para riegos de liga con emulsiones asfálticas.

Donovan, E.P., Al-Qadi, I.L., Loulizi, A., 2000. Optimization of tack coat application rate for geocomposite membrane on bridge decks. Transp. Res. Rec. 143–150. https://doi.org/10.3141/1740-18

Elsing, A., Leite-Gembus, F., 2019. Parameter to ensure a durable grid-reinforced asphalt pavement. Bitum. Mix. Pavements VII- Proc. 7th Int. Conf. Bitum. Mix. Pavements, ICONFBMP 2019 602–607. https://doi.org/10.1201/9781351063265-81

European Standard, 2021. EN 12697-48:2021 - Bituminous mixtures - Test methods - Part 48: Interlayer Bonding.

Ferrotti, G., Canestrari, F., Pasquini, E., Virgili, A., 2012. Experimental evaluation of the influence of surface coating on fiberglass geogrid performance in asphalt pavements. Geotext. Geomembranes 34, 11–18. https://doi.org/10.1016/j.geotexmem.2012.02.011

FGSV, 2013. ZTV Asphalt-StB 07/13: Zusätzliche Technische Vertragsbedingungen und Richtlinien für den Bau von Verkehrsflächenbefestigungen aus Asphalt.

FGSV 770, 2013. Arbeitspapier fuer die verwendung von vliesstoffen, gittern und verbundstoffen im asphaltstrassenbau.

FHWA, 2020. Density Demonstration Projects and Related Specification - TechBrief - FHWA-HIF-21-020. Washington DC, USA.

Fonseca, L.F., 2015. Avaliação em laboratório do comportamento de camadas asfálticas reforçadas com geossintéticos. Universidade Federal de Minas Gerais.

Ge, Z., Wang, H., Zhang, Q., Xiong, C., 2015. Glass fiber reinforced asphalt membrane for interlayer bonding between asphalt overlay and concrete pavement. Constr. Build. Mater. 101, 918–925. https://doi.org/10.1016/j.conbuildmat.2015.10.145

Giri, J.P., Panda, M., 2018. Laboratory Evaluation of Inter-layer Bond Strength Between

Bituminous Paving Layers. Transp. Infrastruct. Geotechnol. 5, 349–365. https://doi.org/10.1007/s40515-018-0064-z

Goodman, R.E., Taylor, R.L., Brekke, T.L., 1968. A Model for the Mechanics of Jointed Rock. J. Soil Mech. Found. Div. 94, 637–659. https://doi.org/10.1061/JSFEAQ.0001133

Güllü, H., 2014. Factorial experimental approach for effective dosage rate of stabilizer: Application for fine-grained soil treated with bottom ash. Soils Found. 54, 462–477. https://doi.org/10.1016/j.sandf.2014.04.017

Highways England's standards and specifications, 2021. Manual of Contract Documents for Highway Works: Notes for Guidance on the Specification for Highway Works.

Hu, X., Lei, Y., Wang, H., Jiang, P., Yang, X., You, Z., 2017. Effect of tack coat dosage and temperature on the interface shear properties of asphalt layers bonded with emulsified asphalt binders. Constr. Build. Mater. 141, 86–93. https://doi.org/10.1016/j.conbuildmat.2017.02.157

Isailović, I., Falchetto, A.C., Wistuba, M., 2017. Fatigue investigation on asphalt mixture layers' interface. Road Mater. Pavement Des. 18, 514–534. https://doi.org/10.1080/14680629.2017.1389087

Isailović, I., Wistuba, M.P., 2018. Asphalt mixture layers' interface bonding properties under monotonic and cyclic loading. Constr. Build. Mater. 168, 590–597. https://doi.org/10.1016/j.conbuildmat.2018.02.149

Jaskula, P., Rys, D., Stienns, M., Szydlowski, C., Golos, M., Kornacka, K., Zoltko, J., Kawalec, J., Rys, D., Stienns, M., Szydlowski, C., Golos, M., Kornacka, K., 2023. The effect of multiaxial geocomposite reinforcement on fatigue performance and crack propagation delay in double-layered asphalt beams. https://doi.org/10.1080/14680629.2023.2180998

Karshenas, A., Cho, S.H., Tayebali, A.A., Guddati, M.N., Kim, Y.R., 2014. Importance of normal confinement to shear bond failure of interface in multilayer asphalt pavements. Transp. Res. Rec. 2456, 170–177. https://doi.org/10.3141/2456-17

Keppel, G., Wickens, T.D., 2004. Design and Analysis: A Researcher's Handbook, 4th ed. Pearson Prentice-Hall, Upper Saddle River, NJ.

Khodaii, A., Fallah, S., Moghadas Nejad, F., 2009. Effects of geosynthetics on reduction of reflection cracking in asphalt overlays. Geotext. Geomembranes 27, 1–8. https://doi.org/10.1016/j.geotexmem.2008.05.007

Kim, H., Arraigada, M., Raab, C., Partl, M.N., 2011. Numerical and Experimental Analysis for the

Interlayer Behavior of Double-Layered Asphalt Pavement Specimens. J. Mater. Civ. Eng. 23, 12–20. https://doi.org/10.1061/(ASCE)MT.1943-5533.0000003

Kotz, S., Johnson, N.L., 1992. Breakthroughs in Statistics, Technometrics, Springer Series in Statistics. Springer New York, New York, NY. https://doi.org/10.1007/978-1-4612-4380-9

Kumar, V., Saride, S., 2017a. Evaluation of Interface Shear Properties of Asphalt layers Reinforced with Geosynthetic Interlayers, in: Indian Geotechnical Conference 2017 GeoNEst. pp. 14–17.

Kumar, V., Saride, S., 2017b. Use of digital image correlation for the evaluation of flexural fatigue behavior of asphalt beams with geosynthetic interlayers. Transp. Res. Rec. 2631, 55–64. https://doi.org/10.3141/2631-06

Kumar, V. V., Saride, S., 2019. Influence of crack depth on performance of geosynthetic-reinforced asphalt overlays, Lecture Notes in Civil Engineering. Springer Singapore. https://doi.org/10.1007/978-981-13-6713-7_15

Kumar, V. V., Saride, S., Zornberg, J.G., 2021. Fatigue Performance of Geosynthetic-reinforced Asphalt Layers. Geosynth. Int. 28, 584–597. https://doi.org/https://doi.org/10.1680/jgein.21.00013

Kumar, V Vinay, Roodi, G.H., Subramanian, S., Zornberg, J.G., 2022. Geotextiles and Geomembranes Influence of asphalt thickness on performance of geosynthetic-reinforced asphalt : Full-scale field study. Geotext. Geomembranes 50, 1052–1059. https://doi.org/10.1016/j.geotexmem.2022.06.005

Kumar, V.V., Roodi, G.H., Zornberg, J.G., 2023. Evaluation of geosynthetic-asphalt interface characteristics using Leutner shear tester, in: Geosynthetics: Leading the Way to a Resilient Planet. CRC Press, London, pp. 2146–2152. https://doi.org/10.1201/9781003386889-289

Kumar, V. Vinay, Saride, S., Zornberg, J.G., 2022. Behavior of Asphalt Overlays with Geogrids and Geocomposite Interlayer Systems, in: Tutumluer, E., Nazarian, S., Al-Qadi, I., Qamhia, I.I. (Eds.), Lecture Notes in Civil Engineering. Springer International Publishing, pp. 611–619. https://doi.org/10.1007/978-3-030-77234-5_50

Latha, G.M., Somwanshi, A., Reddy, K.H., 2013. A Multiple Regression Equation for Prediction of Bearing Capacity of Geosynthetic Reinforced Sand Beds. Indian Geotech. J. 43, 331–343. https://doi.org/10.1007/s40098-013-0053-7

Lee, J.H., Baek, S.B., Lee, K.H., Kim, J.S., Jeong, J.H., 2019. Long-term performance of fiber-grid-reinforced asphalt overlay pavements: A case study of Korean national highways. J.

Traffic Transp. Eng. (English Ed. 6, 366–382. https://doi.org/10.1016/j.jtte.2018.01.008

Lee, S.L., Mannan, M.A., Wan Ibrahim, W.H., 2020. Shear strength evaluation of composite pavement with geotextile as reinforcement at the interface. Geotext. Geomembranes 48, 230–235. https://doi.org/10.1016/j.geotexmem.2019.11.002

Leite-Gembus, F., Elsing, A., 2020. Shear Bonding Performance of Reinforced Asphalt Pavements by Using Polyester Grids, in: Raab, C. (Ed.), Lecture Notes in Civil Engineering: Proceedings of the 9th International Conference on Maintenance and Rehabilitation of Pavements—Mairepav9. pp. 651–661. https://doi.org/10.1007/978-3-030-48679-2_61

Leutner, R., 1979. Untersuchung des Schichtverbundes beim bituminösen Oberbau. Bitumen 41, 84–9.

Liao, M.-C., Chen, J.-S., Tsou, K.-W., 2012. Fatigue Characteristics of Bitumen-Filler Mastics and Asphalt Mixtures. J. Mater. Civ. Eng. 24, 916–923. https://doi.org/10.1061/(asce)mt.1943-5533.0000450

Masad, E., Castelo Branco, V.T.F., Little, D.N., Lytton, R., 2008. A unified method for the analysis of controlled-strain and controlled-stress fatigue testing. Int. J. Pavement Eng. 9, 233–246. https://doi.org/10.1080/10298430701551219

Ministerio de Transportes Movilidad y Agenda Urbana, 2015. Artículo 531 Riegos de adherencia. Minist. Fom.

Miró, R., Ortiz-Ripoll, J., Martínez, A., Botella, R., Pérez-Jiménez, F., López-Montero, T., 2021. A new proposal to assess shear fatigue resistance of asphalt pavement interfaces. Road Mater. Pavement Des. 22, S462–S481. https://doi.org/10.1080/14680629.2021.1899966

Mohammad, L.N., Bae, A., Elseifi, M.A., Button, J., Patel, N., 2010. Effects of pavement surface type and sample preparation method on tack coat interface shear strength. Transp. Res. Rec. 93–101. https://doi.org/10.3141/2180-11

Mohammad, L.N., Bae, A., Elseifi, M.A., Button, J.W., Scherocman, J.A., 2009. Interface Shear Strength Characteristics of Emulsified Tack Coats. J. Assoc. Asph. Paving Technol. 78, 249–278.

Mohammad, L.N., Elseifi, M.A., Bae, A., Patel, N., 2012. Optimization of Tack Coat for HMA Placement (NCHRP Report 712), NCHRP Report 712.

Mohammad, L.N., Elseifi, M.A., Das, R., Cao, W., 2018. Validation of the Louisiana Interlayer Shear Strength Test for Tack Coat, Validation of the Louisiana Interlayer Shear Strength Test

for Tack Coat. Transportation Research Board, Washington, D.C. https://doi.org/10.17226/25458

Mohammad, L.N., Raqib, M., Huang, B., 2002. Influence of Asphalt Tack Coat Materials on Interface Shear Strength. Transp. Res. Rec. J. Transp. Res. Board 1789, 56–65. https://doi.org/10.3141/1789-06

Montgomery, D.C., Runger, G.C., 2014. Applied Statistics and Probability for Engineers, 6 ed. ed. John Wiley & Sons.

Montgomery, D.C.A.S.U., 2017. Design and Analysis of Experiments, 8 ed. ed. John Wiley & Sons.

Nian, T., Ge, J., Li, P., Guo, R., Liu, W., 2020. Influence of Multiple Factors on the Shear Fatigue Resistance of Asphalt Pavement Interlayer Adhesive Materials. J. Mater. Civ. Eng. 32, 04020251. https://doi.org/10.1061/(ASCE)MT.1943-5533.0003330

NLT-382, 2008. Evaluación De La Adherencia Entre Capas De Firme, Mediante Ensayo De Corte. CEDEX, Madird.

Noory, A., Moghadas Nejad, F., Khodaii, A., 2019. Evaluation of the effective parameters on shear resistance of interface in a geocomposite-reinforced pavement. Int. J. Pavement Eng. 20, 1106–1117. https://doi.org/10.1080/10298436.2017.1394094

Noory, A., Moghadas Nejad, F., Khodaii, A., 2017. Evaluation of shear bonding and reflective crack propagation in a geocomposite reinforced overlay. Geosynth. Int. 24, 343–361. https://doi.org/10.1680/jgein.17.00007

Ortiz-Ripoll, J., Miró, R., Martínez, A.H., 2020. Semi-empirical method for the calculation of shear stress, stiffness and maximum shear strength of bituminous interfaces under in-service conditions. Constr. Build. Mater. 258, 120374. https://doi.org/10.1016/j.conbuildmat.2020.120374

Ozer, H., Al-Qadi, I.L., Wang, H., Leng, Z., 2012. Characterisation of interface bonding between hot-mix asphalt overlay and concrete pavements: Modelling and in-situ response to accelerated loading. Int. J. Pavement Eng. 13, 181–196. https://doi.org/10.1080/10298436.2011.596935

Partl, M., Piber, H., Raab, C., 2009. RILEM interlaboratory test on interlayer bonding of asphalt pavements, in: Advanced Testing and Characterization of Bituminous Materials. CRC Press, pp. 1181–1190. https://doi.org/10.1201/9780203092989.ch115

Partl, M.N., Raab, C., 1999. Shear adhesion between top layers of fresh asphalt pavements in Switzerland., in: Proceedings of the 7th Conference on Asphalt Pavements for Southern Africa. Victoria Falls, Zimbabwe.

Pasetto, M., Pasquini, E., Giacomello, G., Baliello, A., 2019. Innovative composite materials as reinforcing interlayer systems for asphalt pavements : an experimental study. Road Mater. Pavement Des. 20, 1–15. https://doi.org/10.1080/14680629.2019.1628438

Petit, C., Chabot, A., Destrée, A., Raab, C., 2018. Recommendation of RILEM TC 241-MCD on interface debonding testing in pavements. Mater. Struct. 51, 96. https://doi.org/10.1617/s11527-018-1223-y

Petit, C., Millien, A., Canestrari, F., Pannunzio, V., Virgili, A., 2012. Experimental study on shear fatigue behavior and stiffness performance of Warm Mix Asphalt by adding synthetic wax. Constr. Build. Mater. 34, 537–544. https://doi.org/10.1016/j.conbuildmat.2012.02.010

Qadir, A., Gazder, U., Choudhary, K., 2021. Statistical analysis for comparing and predicting rutting resistance of asphalt pavements with rigid and flexible geogrid layers. Constr. Build. Mater. 302, 124136. https://doi.org/10.1016/j.conbuildmat.2021.124136

Raab, C., Grenfell, J., Abd El Halim, A.O., Partl, M.N., 2016. Comparison of interlayer bond behavior due to ageing. RILEM Bookseries 11, 323–334. https://doi.org/10.1007/978-94-017-7342-3_26

Raab, C., Partl, M.N., 2009. Influence of the gap width between the shearing rings on interlayer shear bond testing, in: Proceedings of Second International Conference Environmentally Friendly Roads. pp. 1–8.

Raab, C., Partl, M.N., 1999. Methoden zur Beurteilung des Schichtenverbunds von Asphaltbelägen. Report nº 442.

Raab, C., Partl, M.N., Abd El Halim, A.O., 2010. Effect of Gap Width on Interlayer Shear Bond Results. Int. J. Pavement Res. Technol. 3, 79–85.

Ragni, D., Graziani, A., Canestrari, F., 2019. Cyclic interlayer testing in bituminous pavements, in: Nikolaides, A.F., Manthos, E. (Eds.), Bituminous Mixtures and Pavements VII. CRC Press, pp. 207–212. https://doi.org/10.1201/9781351063265-31

Ragni, D., Sudarsanan, N., Canestrari, F., Kim, Y.R., 2022. Investigation into fatigue life of interface bond between asphalt concrete layers. Int. J. Pavement Eng. 23, 3371–3385. https://doi.org/10.1080/10298436.2021.1894420

Rahman, A., Ai, C., Xin, C., Gao, X., Lu, Y., 2017. State-of-the-art review of interface bond testing devices for pavement layers: toward the standardization procedure. J. Adhes. Sci. Technol. 31, 109–126. https://doi.org/10.1080/01694243.2016.1205240

Romanoschi, S.A., Metcalf, J.B., 2002. The Characterization of Pavement Layer Interfaces, in: Proceedings of the 9th International Conference on Asphalt Pavements (ISAP). International Society for Asphalt Pavements., Copenhague, pp. 624–631.

Romanoschi, S.A., Metcalf, J.B., 2001. Characterization of Asphalt Concrete Layer Interfaces. Transp. Res. Rec. J. Transp. Res. Board 1778, 132–139. https://doi.org/10.3141/1778-16

Roodi, G.H., Morsy, A.M., Zornberg, J.G., 2017. Experimental Evaluation of the Interaction between Geosynthetic Reinforcements and Hot Mix Asphalt, in: Airfield and Highway Pavements 2017. pp. 428–439.

Roque, R., Hernando, D., Park, B., Zou, J., Waisome, J.A.M., 2017. Evaluation of asphalt pavement interface conditions for enhanced bond performance.

Roussel, J.-M., Attia, T., Di Benedetto, H., Sauzeat, C., Broutin, M., 2022. Influence of interface properties on heavy weight deflectometer test results. Road Mater. Pavement Des. 1–16. https://doi.org/10.1080/14680629.2022.2029759

Safavizadeh, A., Kim, Y.R., 2014. Mode II fatigue and reflective cracking performance of GlasGrid-reinforced asphalt concrete under repeated loading. Asph. Pavements - Proc. Int. Conf. Asph. Pavements, ISAP 2014 2, 1893–1902. https://doi.org/10.1201/b17219-228

Safavizadeh, S.A., Cho, S.-H., Kim, Y.R., 2022a. Interface shear strength and shear fatigue resistance of fibreglass grid-reinforced asphalt concrete test specimens. Int. J. Pavement Eng. 23, 2531–2542. https://doi.org/10.1080/10298436.2020.1861447

Safavizadeh, S.A., Cho, S., Kim, Y.R., 2022b. Interface shear strength and shear fatigue resistance of fibreglass grid-reinforced asphalt concrete test specimens. https://doi.org/10.1080/10298436.2020.1861447

Safavizadeh, S.A., Wargo, A., Guddati, M., Kim, Y.R., 2015. Investigating reflective cracking mechanisms in grid-reinforced asphalt specimens: Use of four-point bending notched beam fatigue tests and digital image correlation. Transp. Res. Rec. 2507, 29–38. https://doi.org/10.3141/2507-04

Sagnol, L., Quezada, J.C., Chazallon, C., Stöckner, M., 2019. Effect of glass fibre grids on the bonding strength between two asphalt layers and its Contact Dynamics method modelling.

Road Mater. Pavement Des. 20, 1164–1181. https://doi.org/10.1080/14680629.2018.1439764

Santagata, E., Canestrari, F., Santagata, F.A., 1993. Laboratory shear testing of tack coat emulsion, in: Proceedings of 1st World Congress on Emulsion. Paris.

Santagata, F.A., Ferrotti, G., Partl, M.N., Canestrari, F., 2009. Statistical investigation of two different interlayer shear test methods. Mater. Struct. Constr. 42, 705–714. https://doi.org/10.1617/s11527-008-9414-6

Santagata, F.A., Parti, M. N.Santagata, F. A., Parti, M. N., Ferrotti, G., Canestrari, F., & Flisch, A. (2008). Layer characteristics affecting interlayer shear resistance in flexible pavements. Asphalt Paving Technology: Association of Asphalt Paving Technologists-Procee, 222–256., Ferrotti, G., Canestrari, F., Flisch, A., 2008. Layer characteristics affecting interlayer shear resistance in flexible pavements, in: Asphalt Paving Technology: Association of Asphalt Paving Technologists-Proceedings of the Technical Sessions. pp. 222–256.

Saride, S., Kumar, V.V., 2017. Influence of geosynthetic-interlayers on the performance of asphalt overlays on pre-cracked pavements. Geotext. Geomembranes 45, 184–196. https://doi.org/10.1016/j.geotexmem.2017.01.010

Shapiro, S.S., Wilk, M.B., 1965. An Analysis of Variance Test for Normality (Complete Samples). Biometrika 52, 591. https://doi.org/10.2307/2333709

Sholar, G.A., Page, G.C., Musselman, J.A., Upshaw, P.B., Moseley, H.L., 2004. Preliminary investigation of a test method to evaluate bond strength of bituminous tack coats. J. Assoc. Asph. Paving Technol. 73, 771–806.

Silva, L.F.M., Öchsner, A., Adams, R.D. (Eds.), 2018. Handbook of Adhesion Technology, in: Handbook of Adhesion Technology. Springer International Publishing, Cham, Suíça. https://doi.org/10.1007/978-3-319-55411-2_7

Solatiyan, E., Bueche, N., Carter, A., 2021a. Laboratory evaluation of interfacial mechanical properties in geogrid-reinforced bituminous layers. Geotext. Geomembranes. https://doi.org/10.1016/j.geotexmem.2020.12.014

Solatiyan, E., Bueche, N., Carter, A., 2021b. Experimental Measurements of Interfacial Mechanical Properties between Rehabilitated Bituminous Layers Using Innovative Approaches. J. Mater. Civ. Eng. 33, 04021077. https://doi.org/10.1061/(asce)mt.1943-5533.0003697

Song, W., Shu, X., Huang, B., Woods, M., 2016. Laboratory investigation of interlayer shear

fatigue performance between open-graded friction course and underlying layer. Constr. Build. Mater. 115, 381–389. https://doi.org/10.1016/j.conbuildmat.2016.04.060

Spadoni, S., Ingrassia, L.P., Paoloni, G., Virgili, A., Canestrari, F., 2021. Influence of geocomposite properties on the crack propagation and interlayer bonding of asphalt pavements. Materials (Basel). 14, 1–18. https://doi.org/10.3390/ma14185310

Stöckert, U.., 2001. Schichtenverbund – Prüfung und Bewertungshintergrund. Straße + Autobahn 11, 624–631.

Sudarsanan, N., Arulrajah, A., Karpurapu, R., Amrithalingam, V., 2020. Fatigue Performance of Geosynthetic-Reinforced Asphalt Concrete Beams. J. Mater. Civ. Eng. 32, 04020206. https://doi.org/10.1061/(ASCE)MT.1943-5533.0003267

Sudarsanan, N., Karpurapu, R., Amirthalingam, V., Gedela, R., 2018a. Applications of natural geotextiles in asphalt overlays to retard reflection cracking, in: 11th International Conference on Geosynthetics.

Sudarsanan, N., Karpurapu, R., Amrithalingam, V., 2018b. An investigation on the interface bond strength of geosynthetic-reinforced asphalt concrete using Leutner shear test. Constr. Build. Mater. 186, 423–437. https://doi.org/10.1016/j.conbuildmat.2018.07.010

Sufian, A.A., Swiertz, D., Bahia, H.U., Mohammad, L., Akentuna, M., 2021. Factors affecting the interlayer shear strength of laboratory and field samples. Transp. Res. Rec. 2675, 234–244. https://doi.org/10.1177/0361198120975414

Sun, D., Li, B., Ye, F., Zhu, X., Lu, T., Tian, Y., 2018. Fatigue behavior of microcapsule-induced self-healing asphalt concrete. J. Clean. Prod. 188, 466–476. https://doi.org/10.1016/j.jclepro.2018.03.281

Sutanto, M.H., Collop, A.C., Airey, G.D., Elliott, R.C., 2007. Laboratory measurement of shear interface strength beneath a thin asphalt layer, in: Proceedings Advanced Characterisation of Pavement and Soil Engineering Materials. Taylor and Francis, Atenas, pp. 1327–1336.

Swiss Standard, 2012. SN 640430: Walzasphalt, Konzeption, Ausfuhrung und Anforderungen an die eingebauten Schichten.

Taylor, R., 1990. Interpretation of the Correlation Coefficient: A Basic Review. J. Diagnostic Med. Sonogr. 6, 35–39. https://doi.org/10.1177/875647939000600106

Tozzo, C., D'Andrea, A., Al-Qadi, I.L., 2016. Dilatancy in the analysis of interlayer cyclic shear test results. J. Mater. Civ. Eng. 28, 1–7. https://doi.org/10.1061/(ASCE)MT.1943-

5533.0001690

Tozzo, C., D'Andrea, A., Al-Qadi, I.L., 2015. Prediction of Fatigue Failure at Asphalt Concrete Layer Interface from Monotonic Testing. Transp. Res. Rec. J. Transp. Res. Board 2507, 50–56. https://doi.org/10.3141/2507-06

Tozzo, C., D'Andrea, A., Cozzani, D., Meo, A., 2014a. Fatigue investigation of the interface shear performance in asphalt pavement. Mod. Appl. Sci. 8, 1–11. https://doi.org/10.5539/mas.v8n2p1

Tozzo, C., Fiore, N., D'Andrea, A., 2014b. Dynamic shear tests for the evaluation of the effect of the normal load on the interface fatigue resistance. Constr. Build. Mater. 61, 200–205. https://doi.org/10.1016/j.conbuildmat.2014.03.010

Tran, N., Willis, R., Julian, G., 2012. NCAT Report No . 12-04 Refinement of the bond strength procedure and investigation.

UNI/TS 11214, 2007. Caratterizzazione prestazionale a taglio delle interfacce: Metodo di prova ASTRA.

Uzan, J., Livneh, M., Eshed, Y., 1978. Investigation of Adhesion Properties Between Asphaltic-Concrete Layers. Asph. Paving Technol 47, 495–521.

Venudharan, V., Biligiri, K.P., 2015. Estimation of phase angles of asphalt mixtures using resilient modulus test. Constr. Build. Mater. 82, 274–286. https://doi.org/10.1016/j.conbuildmat.2015.02.061

Walubita, L.F., Mahmoud, E., Lee, S.I., Carrasco, G., Komba, J.J., Fuentes, L., Nyamuhokya, T.P., 2019. Use of grid reinforcement in HMA overlays – A Texas field case study of highway US 59 in Atlanta District. Constr. Build. Mater. 213, 325–336. https://doi.org/10.1016/j.conbuildmat.2019.04.072

Walubita, L.F., Nyamuhokya, T.P., Komba, J.J., Ahmed Tanvir, H., Souliman, M.I., Naik, B., 2018. Comparative assessment of the interlayer shear-bond strength of geogrid reinforcements in hot-mix asphalt. Constr. Build. Mater. 191, 726–735. https://doi.org/10.1016/j.conbuildmat.2018.10.035

Wang, H., Zhao, J., Hu, X., Zhang, X., 2020. Flexible Pavement Response Analysis under Dynamic Loading at Different Vehicle Speeds and Pavement Surface Roughness Conditions. J. Transp. Eng. Part B Pavements 146, 04020040. https://doi.org/10.1061/jpeodx.0000198

Wang, X., Su, Z., Xu, A., Zhou, A., Zhang, H., 2017. Shear fatigue between asphalt pavement

layers and its application in design. Constr. Build. Mater. 135, 297–305. https://doi.org/10.1016/j.conbuildmat.2016.12.151

Wargo, A., Safavizadeh, S.A., Kim, Y.R., 2017. Comparing the Performance of Fiberglass Grid with Composite Interlayer Systems in Asphalt Concrete. Transp. Res. Rec. J. Transp. Res. Board 2631, 123–132. https://doi.org/10.3141/2631-14

West, R.C., Zhang, J., Moore, J., 2005. Evaluation of Bond Strength Between Pavement Layers, NCAT Report 05-08.

Wheat, M., 2007. Evalutation of bond strength at asphalt interfaces. Kansas State University.

White, G., 2017. State of the art: interface shear resistance of asphalt surface layers. Int. J. Pavement Eng. 18, 887–901. https://doi.org/10.1080/10298436.2015.1126270

Yang, K., Li, R., 2021. Characterization of bonding property in asphalt pavement interlayer: A review. J. Traffic Transp. Eng. (English Ed. 8, 374–387. https://doi.org/10.1016/j.jtte.2020.10.005

Yang, K., Li, R., Yu, Y., Pei, J., 2021. Unified laboratorial evaluation of interlayer bond property in asphalt pavements based on strength parameters. Constr. Build. Mater. 273, 121738. https://doi.org/10.1016/j.conbuildmat.2020.121738

Yang, K., Li, R., Yu, Y., Pei, J., Liu, T., 2020. Evaluation of interlayer stability in asphalt pavements based on shear fatigue property. Constr. Build. Mater. https://doi.org/10.1016/j.conbuildmat.2020.119628

Ye, Q., Wu, S., Li, N., 2009. Investigation of the dynamic and fatigue properties of fiber-modified asphalt mixtures. Int. J. Fatigue 31, 1598–1602. https://doi.org/10.1016/j.ijfatigue.2009.04.008

Zhang, W., 2017. Effect of tack coat application on interlayer shear strength of asphalt pavement: A state-of-the-art review based on application in the United States. Int. J. Pavement Res. Technol. 10, 434–445. https://doi.org/10.1016/j.ijprt.2017.07.003

Zofka, A., Maliszewski, M., Bernier, A., Josen, R., Vaitkus, A., Kleizienė, R., 2015. Advanced shear tester for evaluation of asphalt concrete under constant normal stiffness conditions. Road Mater. Pavement Des. 16, 187–210. https://doi.org/10.1080/14680629.2015.1029690